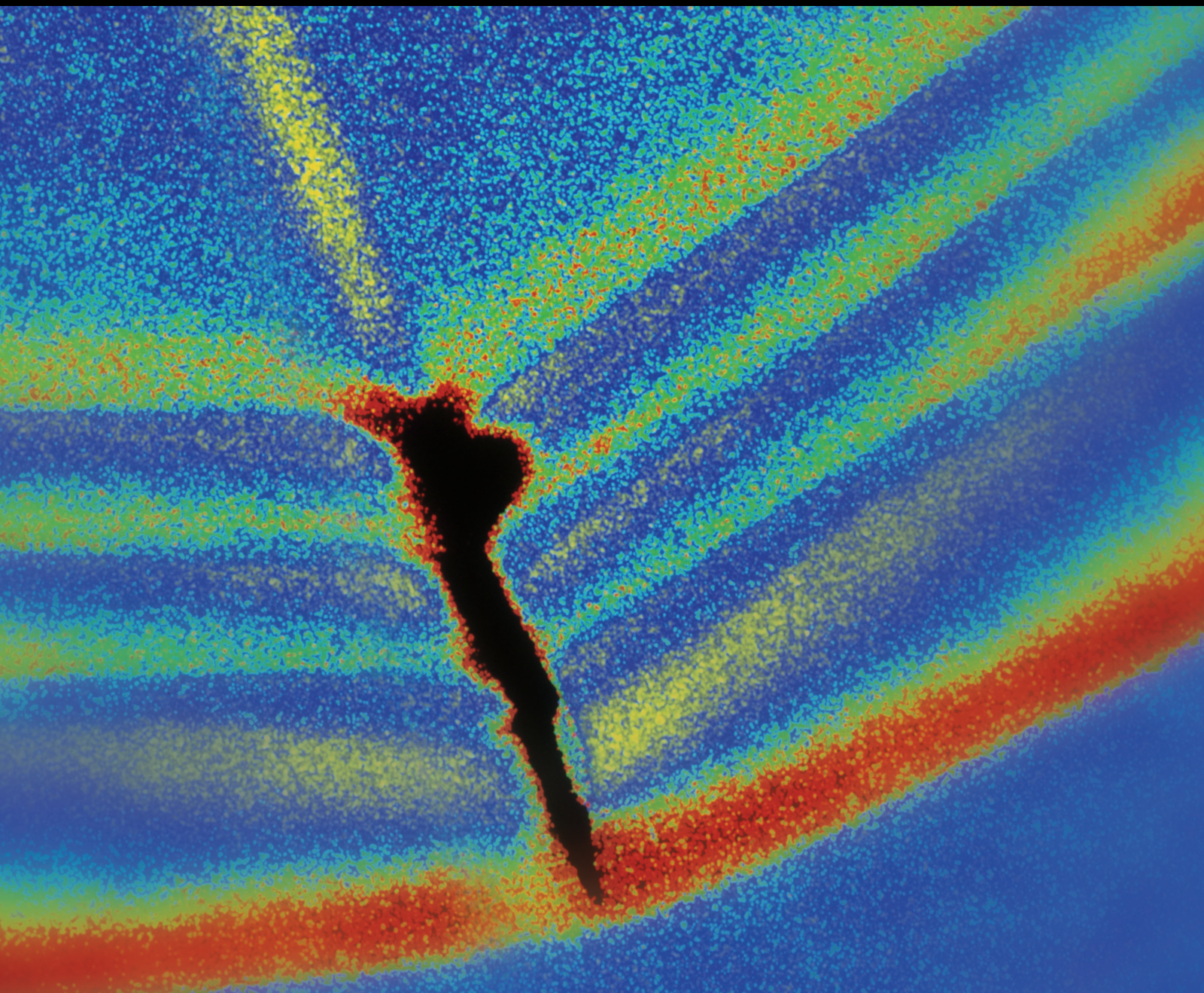


Shock and Vibration

# Dynamics, Control, and Modeling of Fractional-Order Systems

Lead Guest Editor: José M. Balthazar

Guest Editors: Paulo B. Gonçalves, Grzegorz Litak, Ângelo M. Tusset,  
and Livija Cveticanin





---

# **Dynamics, Control, and Modeling of Fractional-Order Systems**

Shock and Vibration

---

## **Dynamics, Control, and Modeling of Fractional-Order Systems**

Lead Guest Editor: José M. Balthazar

Guest Editors: Paulo B. Gonçalves, Grzegorz Litak,  
Ângelo M. Tusset, and Livija Cveticanin



---

Copyright © 2018 Hindawi. All rights reserved.

This is a special issue published in "Shock and Vibration." All articles are open access articles distributed under the Creative Commons Attribution License, which permits unrestricted use, distribution, and reproduction in any medium, provided the original work is properly cited.

## Editorial Board

- Brij N. Agrawal, USA  
Felix Albu, Romania  
Marco Alfano, Italy  
Sumeet S. Aphale, UK  
Hassan Askari, Canada  
Lutz Auersch, Germany  
Matteo Aureli, USA  
Mahmoud Bayat, Iran  
Marco Belloli, Italy  
Giosuè Boscato, Italy  
Francesco Braghin, Italy  
Rafał Burdzik, Poland  
Salvatore Caddemi, Italy  
Ivo Caliò, Italy  
Antonio Carcaterra, Italy  
Dumitru I. Caruntu, USA  
Cristina Castejón, Spain  
Nicola Caterino, Italy  
Gabriele Cazzulani, Italy  
Noel Challamel, France  
Athanasios Chasalevris, UK  
Xavier Chimentin, France  
Nawawi Chouw, New Zealand  
Simone Cinquemani, Italy  
Pedro A. Costa, Portugal  
Alvaro Cunha, Portugal  
Giorgio Dalpiaz, Italy  
Farhang Daneshmand, Canada  
Sergio De Rosa, Italy  
Silvio L.T. de Souza, Brazil  
Dario Di Maio, UK  
Luigi Di Sarno, Italy  
Longjun Dong, China  
Lorenzo Dozio, Italy  
Mohamed El Badaoui, France  
Mohammad Elahinia, USA  
Fiorenzo A. Fazzolari, UK  
Matteo Filippi, Italy  
Piotr Folega, Poland  
Paola Forte, Italy  
Francesco Franco, Italy  
Juan C. G. Prada, Spain  
Pedro Galvín, Spain  
Gianluca Gatti, Italy  
Marco Gherlone, Italy
- Anindya Ghoshal, USA  
Gilbert R. Gillich, Romania  
Nere Gil-Negrete, Spain  
Adam Glowacz, Poland  
Itzhak Green, USA  
Hassan Haddadpour, Iran  
M.I. Herreros, Spain  
Hamid Hosano, Japan  
Reza Jazar, Australia  
Sakdirat Kaewunruen, UK  
Yuri S. Karinski, Israel  
Jeong-Hoi Koo, USA  
Georges Kouroussis, Belgium  
Mickaël Lallart, France  
Luca Landi, Italy  
Marco Lepidi, Italy  
Zhixiong Li, China  
Manuel Lopez Aenlle, Spain  
Nuno M. Maia, Portugal  
Stefano Manzoni, Italy  
Giuseppe Carlo Marano, Italy  
Stefano Marchesiello, Italy  
Francesco S. Marulo, Italy  
Jean-Mathieu Mencik, France  
Laurent Mevel, France  
Fabio Minghini, Italy  
Mahdi Mohammadpour, UK  
Rui Moreira, Portugal  
Emiliano Mucchi, Italy  
Peter Múčka, Slovakia  
Sara Muggiasca, Italy  
Tony Murmu, UK  
Pedro Museros, Spain  
Roberto Nascimbene, Italy  
Sundararajan Natarajan, India  
Toshiaki Natsuki, Japan  
Miguel Neves, Portugal  
Nicola Nisticò, Italy  
Roberto Palma, Spain  
A. Papageorgiou, Greece  
Francesco Pellicano, Italy  
Paolo Pennacchi, Italy  
Evgeny Petrov, UK  
Giuseppe Piccardo, Italy  
Antonina Pirrotta, Italy
- Franck Poisson, France  
Luca Pugi, Italy  
Mohammad Rafiee, Canada  
Carlo Rainieri, Italy  
José J. Rangel-Magdaleno, Mexico  
Didier Rémond, France  
Francesco Ripamonti, Italy  
Riccardo Rubini, Italy  
Salvatore Russo, Italy  
Giuseppe Ruta, Italy  
Edoardo Sabbioni, Italy  
Filippo Santucci de Magistris, Italy  
Onome E. Scott-Emuakpor, USA  
Roger Serra, France  
Chengzhi Shi, USA  
Vadim V. Silberschmidt, UK  
Kumar V. Singh, USA  
Jean-Jacques Sinou, France  
Isabelle Sochet, France  
Alba Sofi, Italy  
Jussi Sopanen, Finland  
Stefano Sorace, Italy  
Andrea Spaggiari, Italy  
Shuaishuai Sun, Australia  
Chao Tao, China  
Marco Tarabini, Italy  
Gloria Terenzi, Italy  
Mario Terzo, Italy  
Tai Thai, Australia  
Marc Thomas, Canada  
Hamid Toopchi-Nezhad, Iran  
Carlo Trigona, Italy  
Federica Tubino, Italy  
Nerio Tullini, Italy  
Angelo Marcelo Tusset, Brazil  
Jens Twiefel, Germany  
Filippo Ubertini, Italy  
Marcello Vanali, Italy  
F. Viadero, Spain  
M. Ahmer Wadee, UK  
Jörg Wallaschek, Germany  
Matthew J. Whelan, USA  
Agnieszka Wylomanska, Poland  
Enrico Zappino, Italy  
Radoslaw Zimroz, Poland

# Contents

## **Dynamics, Control, and Modeling of Fractional-Order Systems**

José M. Balthazar , Paulo B. Gonçalves , Grzegorz Litak , Angelo M. Tusset ,  
and Livija Cveticanin 

Editorial (2 pages), Article ID 6971490, Volume 2018 (2018)

## **Dynamical Analysis and Control of a Chaotic Microelectromechanical Resonator Model**

Dailhane G. Bassinello , Angelo M. Tusset , Rodrigo T. Rocha , and Jose M. Balthazar 

Research Article (10 pages), Article ID 4641629, Volume 2018 (2018)

## **Dynamic Characteristics of Blade with Viscoelastic Damping Block Based on Complex Eigenvalue Method**

Jiao Wang , Yue-hao Zhang, Tao Yu, and Qing-kai Han 

Research Article (16 pages), Article ID 5068901, Volume 2018 (2018)

## **Experimental Validation of Numerical Model for Bi-Tilt-Isolator**

Ming-Hsiang Shih , Wen-Pei Sung , and Chia-Yu Ho

Research Article (12 pages), Article ID 7163516, Volume 2018 (2018)

## **Experimental Study on Mechanical and Acoustic Emission Characteristics of Rock Samples under Different Stress Paths**

Tao Qin , Hongru Sun, Heng Liu, Junwen Zhang , Tao Li, Gang Liu, and Zhenwen Liu

Research Article (9 pages), Article ID 4813724, Volume 2018 (2018)

## **Multistability in Horizontal Platform System with and without Time Delays**

Karthikeyan Rajagopal , Prakash Duraisamy, Riessom Weldegiorgis, and Anitha Karthikeyan

Research Article (8 pages), Article ID 1092812, Volume 2018 (2018)

## Editorial

# Dynamics, Control, and Modeling of Fractional-Order Systems

**José M. Balthazar** <sup>1</sup>, **Paulo B. Gonçalves** <sup>2</sup>, **Grzegorz Litak** <sup>3</sup>,  
**Angelo M. Tusset** <sup>4</sup>, and **Livija Cveticanin** <sup>5</sup>

<sup>1</sup>*Aeronautics Technological Institute (ITA), São José dos Campos, SP, Brazil*

<sup>2</sup>*Pontifical Catholic University of Rio de Janeiro (PUC-Rio), Rio de Janeiro, Brazil*

<sup>3</sup>*Lublin University of Technology, Lublin, Poland*

<sup>4</sup>*Federal University of Technology-Paraná (UTFPR), Ponta Grossa, PR, Brazil*

<sup>5</sup>*University of Novi Sad, Novi Sad, Serbia*

Correspondence should be addressed to José M. Balthazar; [jmbaltha@gmail.com](mailto:jmbaltha@gmail.com)

Received 14 May 2018; Accepted 15 May 2018; Published 31 July 2018

Copyright © 2018 José M. Balthazar et al. This is an open access article distributed under the Creative Commons Attribution License, which permits unrestricted use, distribution, and reproduction in any medium, provided the original work is properly cited.

This special issue addresses nonlinear system models considering the dynamical analysis, control approaches, and applications in the fractional-order case and their applications to engineering. It involves modeling, applications, and control for nonlinear systems, such as mechanical and electromechanical ones. Five relevant contributions from researchers in different topics of nonlinear systems, describing original theoretical research as well as new experimental results, were published in the presented special issue (SI). The five contributions are summarized, next.

K. Rajagopal et al. analyzed the chaotic behavior using bifurcation diagrams of horizontal platform systems (HPS) identifying the multistable parameter and investigated the coexisting attractors of the HPS. The authors in the work titled “Multistability in Horizontal Platform System with and without Time Delays” investigated the multistability existence in time-delayed HPS, plotting the bifurcation of the autonomous HPS, and showed the multistability and coexisting attractors. D. G. Bassinello et al. studied a nonlinear MEMS resonator, bringing the behavior of such system from a chaotic state to a periodic orbit, considering the time-delayed feedback control, and the sliding mode control, in the paper entitled “Dynamical Analysis and Control of a Chaotic Microelectromechanical Resonator Model”. J. Wang et al. discussed in detail the dynamical characteristics of a blade with viscoelastic damping in the paper entitled “Dynamic Characteristics of Blade with Viscoelastic Damping Block

Based on Complex Eigenvalue Method”. The effects of various parameters including thickness, storage modulus, loss factor of viscoelastic damping block, and rotating speed on natural frequency and modal damping ratio of VE-blade were considered. M.-H. Shih et al. considered the Bi-Tilt Isolator (BTI) composed of bi-tilt beveled substrate and slider in the paper “Experimental Validation of Numerical Model for Bi-Tilt-Isolator”. The proposed mathematical model and BTI element of GENDYN program were analyzed, using cubic polynomial function of friction. The authors carried out fine simulation capability to assess the nonlinear isolation effect of the structure installed with BTI. T. Qin et al. have performed a series of tests on characteristics of acoustic emission sandstone under uniaxial, conventional, triaxial conditions and the unloading confining pressure path. They observed in the paper with title “Experimental Study on Mechanical and Acoustic Emission Characteristics of Rock Samples under Different Stress Paths” that the failure mode of rock specimen was dominated by shear failure under the conventional triaxial stress path and the tension failure was the main form at a lower initial value of unloading confining pressure. In addition, they showed that the shear failure is more prominent at a higher initial value of unloading confining pressure.

We hope that this special issue would be useful in recent advances and developments in the areas of Dynamics, Control, and Modeling of Fractional-Order Systems and

attract attention of the scientific community to pursue further research and further studies.

### **Acknowledgments**

We would like to acknowledge all the authors for their informative contributions and the reviewers for their support and constructive critiques in making this special issue possible.

*José M. Balthazar*  
*Paulo B. Gonçalves*  
*Grzegorz Litak*  
*Angelo M. Tuset*  
*Livija Cveticanin*

## Research Article

# Dynamical Analysis and Control of a Chaotic Microelectromechanical Resonator Model

**Dailhane G. Bassinello** <sup>1</sup>, **Angelo M. Tuset** <sup>2</sup>,  
**Rodrigo T. Rocha** <sup>2</sup> and **Jose M. Balthazar** <sup>1,2</sup>

<sup>1</sup>Department of Electrical Engineering, São Paulo State University, 17033-360 Bauru, SP, Brazil

<sup>2</sup>Federal University of Technology-Paraná, 84016-210 Ponta Grossa, PR, Brazil

Correspondence should be addressed to Rodrigo T. Rocha; [digao.rocha@gmail.com](mailto:digao.rocha@gmail.com)

Received 26 January 2018; Accepted 10 April 2018; Published 15 May 2018

Academic Editor: Onome E. Scott-Emuakpor

Copyright © 2018 Dailhane G. Bassinello et al. This is an open access article distributed under the Creative Commons Attribution License, which permits unrestricted use, distribution, and reproduction in any medium, provided the original work is properly cited.

The dynamic analysis and control of a nonlinear MEM resonator system are considered. Phase diagram, bifurcation diagram, and the 0-1 test are applied to the analysis of the influence of the parameters on the dynamics of the system, whose parameters are damping coefficient, polarization of the voltage, and nonlinear stiffness term. The bifurcation diagram is used to demonstrate the existence of the pull-in effect. Numerical results showed that the parameters, which were taken into account, were significant, indicating that the response can be either chaotic or periodic behavior. In order to bring the system from a chaotic state to a periodic orbit, two controls are considered: the time-delayed feedback control and the sliding mode control.

## 1. Introduction

Microelectromechanical resonators were proposed in the middle of 1990s as a viable alternative for comb-drive actuators and other large conventional filters. Due to the possibility of microelectromechanical system (MEMS) applications, many researchers have dedicated their researches directed to MEMS. In [1] the nonlinear dynamics of micromechanical oscillators are explored experimentally, and a model was built to explain why high-order entrainment is seen only in doubly supported beams, and by its analysis it suggests that the strong amplitude-frequency relationship in doubly supported beams enables hysteresis, wide regions of primary entrainment, and high orders of sub- and superharmonic entrainment. In [2] a model for oscillations from the continuum description of the temperature and displacement field is considered. A bifurcation analysis of the model was performed, allowing estimating the threshold power for self-oscillation as a function of geometric and optical constants of the beam. In [3] the Mathieu–van der Pol Duffing equation is considered for presenting a MEMS model, and the authors investigated the dynamics of the system considering

it forced by parametric and nonparametric excitations. In [4] a thermomechanical model of the system was developed, and its predictions were explored to explain and predict the entrainment phenomenon. The model is validated with experimental results and could also be used to analyze MEMS limit-cycle oscillators designed to achieve specific performance objectives.

In microelectromechanical systems (MEMS), nonlinearities may arise from a variety of sources, such as spring and damping mechanisms and resistive, inductive, and capacitive circuit elements. An interesting example of nonlinearity in MEMS was demonstrated in [5–8] where it is possible to observe that the nonlinear electrostatic force depends on the gap size between the two electrodes.

Due to the nonlinearities presented in the MEMS, chaotic motion may appear. Therefore, some methods may be applied to identify such irregular motion. One of the most effective methods is the 0-1 test that can be used for any system to identify chaotic dynamics. This test uses the temporal series data to characterize the dynamics of the system, analyzing its spectral and statistical properties based on the asymptotic properties of a Brownian motion [9–14].

The ability of the time-delayed feedback control in bringing a system with chaotic behavior to a periodic attractor system has attracted the attention of several researchers, both for numerical and experimental applications.

In [15], experimental results of the application of the time-delayed feedback control in a nonlinear oscillator are presented. The experimental system was an externally driven nonlinear oscillator, including a tunnel diode, as a negative resistance device. To electronically realize the control a special analogue circuit was designed, and the signal of the control is applied in the tunnel diode. The experimental results demonstrated the efficiency of the control.

In [16], the time-delayed feedback control is used in an Atomic Force Microscope microcantilever with chaotic behavior. The control of the chaotic behavior of the system was implemented by using the time-delayed feedback control. Furthermore, in [17], the time-delayed feedback control was used in the control of the chaotic behavior of an Atomic Force Microscope microcantilever. In both cases, the authors used a nonlinear mathematical model for the representation of the AFM, and the control was performed by means of numerical simulations. Those results showed the feasibility of the time-delayed feedback control for chaos control in the considered AFM system.

In addition, the time-delayed feedback control has been used in chaos control of smart systems composed of a pendulum coupled with shape memory alloy (SMA) elements, as considered in [18]. The authors considered applying the extended time-delayed feedback control on a SMA-pendulum system by exploring the SMA temperature-dependent behavior. The numerical results indicated that the controller was able to perform the system stabilization and that, after stabilization, control force tends to vanish.

In [19], Janzen et al. used the SMA in vibration control of a flexible link with slewing motion. The sliding mode control is considered for positioning control and vibration control of the flexible link. According to the authors, the use of the sliding mode control (SMC) is justified because the control technique has been commonly applied to nonlinear systems because of its robustness for uncertainties and external disturbances. Numerical simulations results are presented to demonstrate the effectiveness of the sliding mode strategy for the positioning control of the DC motor and for the vibration suppression of the flexible link by using SMA actuators.

In [20], the chaotic behavior of a micromechanical resonator is analyzed, and the control of chaos is projected. The analyses of the chaotic behavior considered phase portraits, maximum Lyapunov exponent, and bifurcation diagrams. Moreover, a robust fuzzy sliding mode controller (FSMC) was designed to turn the chaotic motion into a periodic motion even when the MEMS have parametrical uncertainties. Numerical simulations showed the robustness of the proposed control.

In the work, the 0-1 test and bifurcation diagrams are applied to investigate the nonlinear dynamics of the MEMS, considering the influence of the damping, variation of the polarization voltage, influence of the nonlinear stiffness term, and pull-in effect. Bifurcation diagrams were considered in this work for the identification of regular and chaotic

behavior, as it is known to be useful and often used for systems with chaotic behavior, such as [20, 21]. The 0-1 test is a tool that makes it possible to analyze the results of the bifurcation diagram in a quantitative way and is successfully used in systems with chaotic behavior, such as [9–14]. In addition, in order to suppress the chaotic motion, the time-delayed feedback control technique and sliding mode control are introduced.

This paper is organized as follows. Section 2 presents the mathematical model for microelectromechanical systems. In Section 3, nonlinearities are observed in the system through the 0-1 test, considering the effects caused by the parameters, which are damping, polarization voltage, the nonlinear stiffness term, and  $V_i$  for pull-in case. In Section 4, the time-delayed feedback control is proposed and applied. In Section 5, the sliding mode control is proposed and applied. Finally, the paper is concluded in Section 6.

## 2. Microelectromechanical System (MEMS)

The behavior of the microelectromechanical system represented by an electrostatic generator of energy, shown in Figure 1, was studied previously in [22]. The physical system represented by Figure 1(a) may be considered as a set of microbeams [5]. The dynamical system under consideration is shown in Figure 1, and this device has two fixed plates and a movable plate between them (see Figure 1(b)), in which a voltage  $V(t)$  composed of a polarization voltage (DC)  $V_p$  and an alternating voltage (AC)  $V_i \sin(\omega t)$  are applied. The DC voltage applies an electrostatic force on the beam and usually changes the equilibrium position. The plates have the function of providing electrodes to form a capacitor or storing electrical energy and provide elasticity or mechanical strength.

The equation of motion of the plates is given by

$$m\ddot{x} = -F_k - F_c - F_e, \quad (1)$$

where  $F_k$  is the conservative force of the spring,  $F_c$  is the damping force of the elastic term, and  $F_e$  is the electric force.

Note that, in Figure 1(b), the distance  $d$  between the fixed and movable plates depends on the position of  $x$  and  $d_0$  (initial distance between the plates). Whereas the fixed plates have the same characteristics, the amount of total electric energy stored in the system can be obtained from

$$\begin{aligned} W^* &= \frac{\epsilon_0 V^2}{2} A \left( \frac{1}{d_0 - x} \right) + \frac{\epsilon_0 V^2}{2} A \left( \frac{1}{d_0 - x} \right) \\ &= \epsilon_0 A V^2 \left( \frac{d_0}{d_0^2 - x^2} \right). \end{aligned} \quad (2)$$

Thus, the electric force  $F_e$  is a nonlinear function of displacement in  $x$  and a quadratic function of voltage:

$$F_e = \frac{\partial W^*}{\partial x} = 2\epsilon_0 d_0 A V^2 \frac{x}{(d_0^2 - x^2)^2}. \quad (3)$$

The spring stiffness is also a parameter that can be affected by elastic term phenomena and nonlinearities, considering

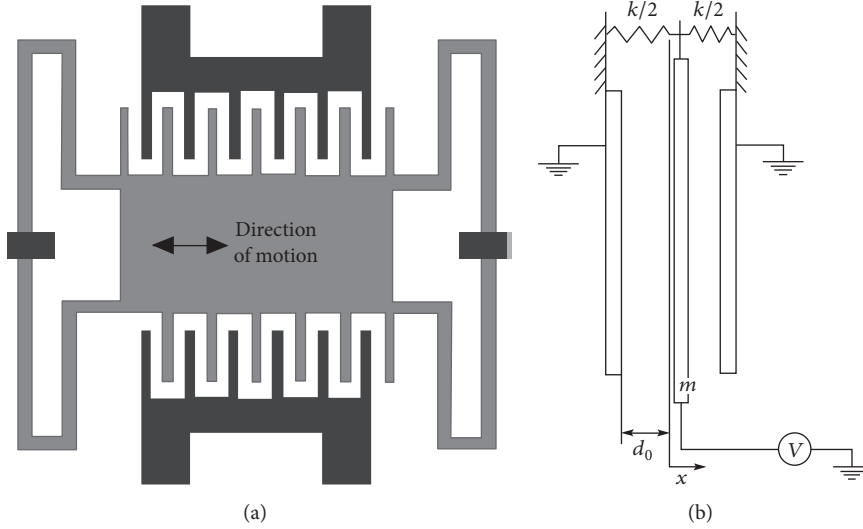


FIGURE 1: (a) In-plane gap closing. (b) Microelectromechanical system [5].

these variations. Then force  $F_k$  of the conservative spring can be represented by

$$F_k = k_1 x + k_3 x^3. \quad (4)$$

The dissipation force  $F_c$  can be obtained from

$$F_c = c \dot{x}. \quad (5)$$

Substituting (3), (4), and (5) into (1), the equation of motion of the MEMS is obtained, given by

$$m \ddot{x} + k_1 x + k_3 x^3 + c \dot{x} = 2 \varepsilon_0 d_0 A V^2 \frac{x}{(d_0^2 - x^2)^2}. \quad (6)$$

Considering the initial conditions as  $x(0) = x_0$ ,  $\dot{x}(0) = \dot{x}_0$  and defining the new variables,  $T = \omega_0 t$ ,  $u = x/x_0$ , (6) can be represented in dimensionless form by

$$\ddot{u} + \alpha_1 \dot{u} + \alpha_3 u^3 + b \dot{u} = \beta V^2 \frac{u}{(d^2 - u^2)^2}, \quad (7)$$

where  $b = (c/m\omega_0)$ ,  $\alpha_1 = (k_1/m\omega_0^2)$ ,  $\alpha_3 = (k_3 x_0^2/m\omega_0^2)$ ,  $\beta = (2\varepsilon_0 d_0 A/m\omega_0^2 x_0^4)$ ,  $w = \omega/\omega_0$ , and  $d = d_0/x_0$ .

Rewriting (7) in state-space notation, it has

$$\begin{aligned} \dot{x}_1 &= x_2 \\ \dot{x}_2 &= -\alpha_1 x_1 - \alpha_3 x_1^3 - b x_2 + \beta V^2 \frac{x_1}{(d^2 - x_1^2)^2}, \end{aligned} \quad (8)$$

where  $x_1 = u$  and  $x_2 = \dot{u}$ .

The equations of motion of the system are defined, and the next step is the dynamical analysis of the system, which is carried out in the next section.

### 3. Dynamical Analysis Using 0-1 Test

The 0-1 test, proposed in [9, 10], is directly applied to a time series data, based on the statistical properties of a single

coordinate; herein, the variable is  $x_1$  (see (8)). Basically, the 0-1 test consists of estimating a single parameter  $K$ . The test considers a system variable  $x_j$ , where two new coordinates  $(p, q)$  are defined as follows:

$$\begin{aligned} p(n, \bar{c}) &= \sum_{j=0}^n x(j) \cos(j\bar{c}) \\ q(n, \bar{c}) &= \sum_{j=0}^n x(j) \sin(j\bar{c}), \end{aligned} \quad (9)$$

where  $\bar{c} \in (0, \pi)$  is a constant. The mean square displacement of the new variables  $p(n, \bar{c})$  and  $q(n, \bar{c})$  is given by

$$\begin{aligned} M(n, c) &= \lim_{n \rightarrow \infty} \frac{1}{N} \sum_{j=1}^N \left[ (p(j+n, \bar{c}) - p(j, \bar{c}))^2 \right. \\ &\quad \left. + (q(j+n, \bar{c}) - q(j, \bar{c}))^2 \right], \end{aligned} \quad (10)$$

where  $n = 1, 2, \dots, N$  and, therefore, the parameter  $K_c$  is obtained in the limit of a very long time by

$$K = \frac{\text{cov}(Y, M(\bar{c}))}{\sqrt{\text{var}(Y) \text{var}(M(\bar{c}))}}, \quad (11)$$

where vectors  $M(\bar{c}) = [M(1, \bar{c}), M(2, \bar{c}), \dots, M(n_{\max}, \bar{c})]$  and  $Y = 1, 2, \dots, n_{\max}$ .

Given any two vectors  $x$  and  $y$ , the covariance  $\text{cov}(x, y)$  and variance  $\text{var}(x)$ , of  $n_{\max}$  elements, are usually defined as [11]

$$\text{cov}(x, y) = \frac{1}{n_{\max}} \sum_{n=1}^{n_{\max}} (x(n) - \bar{x})(y(n) - \bar{y}) \quad (12)$$

$$\text{var}(x) = \text{cov}(x, y),$$

where  $\bar{x}$  and  $\bar{y}$  are the average of  $x(n)$  and  $y(n)$ , respectively. As a final result, the value of the searched parameter  $K$  is

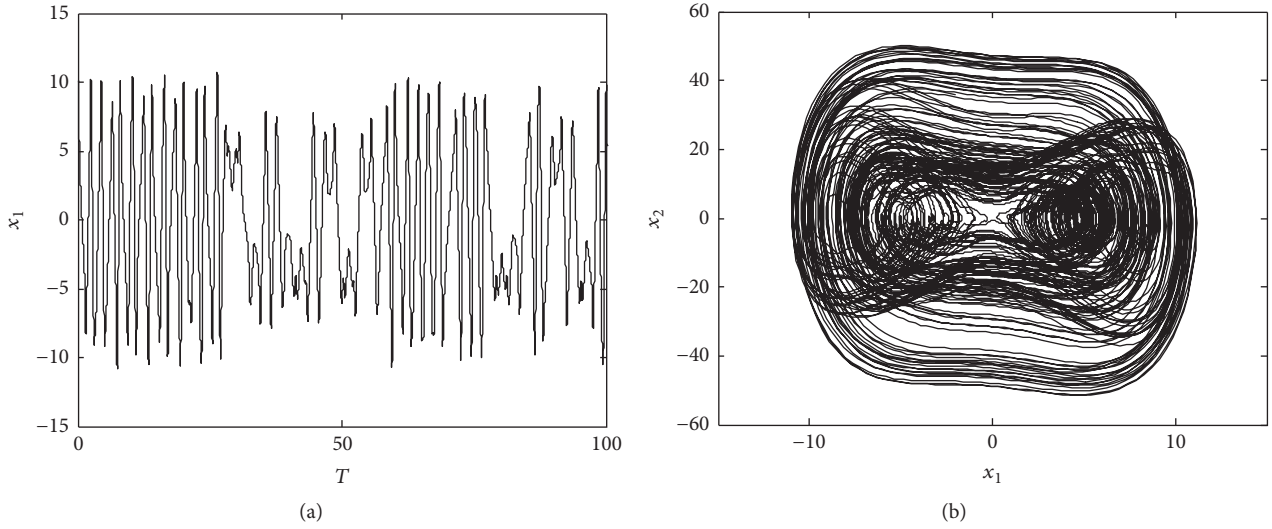
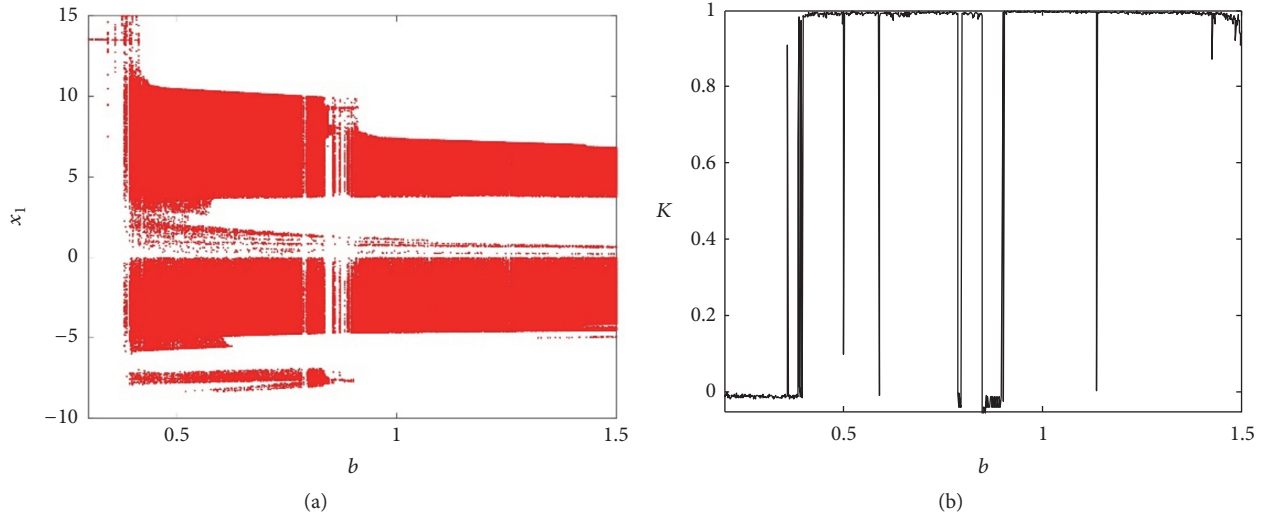


FIGURE 2: (a) Displacement. (b) Phase plane.

FIGURE 3: (a) Bifurcation diagram ( $b$  versus  $x_1$ ). (b)  $K$  versus  $b$ .

obtained taking the median of 100 different values of the parameter  $\bar{c} \in (0, \pi)$  in (11). If  $K$  value is close to 0, the system is periodic; on the other hand, if  $K$  value is close to 1, the system is chaotic. In all simulations,  $n = 1000$  and  $j = n/100, \dots, n/10$  were chosen.

The values of the parameters used in the current numerical investigations were taken from [23] and they are as follows:  $\alpha_1 = 1$ ,  $\alpha_3 = 0.4$ ,  $\beta = 69141.6$ ,  $b = 0.5$ ,  $d = 25$ ,  $\omega = 6.28$ ,  $V_p = 2$ ,  $V_i = 10$ ,  $x_{10} = 1$ , and  $x_{20} = 1.5$ . The parameters  $\alpha_1, \alpha_3, \beta$ , and  $b$  were chosen in [16] such as ( $k_1 \ll 2\varepsilon_0 d_0 A$ ).

The time history of the displacement and the phase plane can be observed in Figure 2.

Next, the effects caused by the parameters will be considered: damping parameter  $b$ , the polarization voltage  $V_p$ , the nonlinear stiffness term  $\alpha_3$ , and  $V_i$  for pull-in case.

**3.1. Damping Effect of the MEMS.** The numerical study of the MEMS shows that the damping effect can be very significant. Figure 3 shows the bifurcation diagram and the 0-1 test varying the damping parameter  $b$ , considering  $b \in [0.2, 1.5]$ . As can be seen in Figure 3, the system is periodic to the left of  $b \approx 0.4$  and most of resting values of  $b$  the system are chaotic.

A tendency of stability of chaotic behavior with the damping  $b$  variation is presented in Figure 3, indicating that a significant region of the parameter  $b$  led the system to chaotic behavior. Periodic behaviors are observed in small regions of parameter  $b$ , which are the intervals  $0.2 \leq b < 0.35$  or  $0.849 < b < 0.896$ .

**3.2. Influence of the Polarization Voltage.** Consider now the variation of the polarization voltage  $V_p$  of the nonlinear MEMS. Figure 4 shows the bifurcation diagram and the 0-1

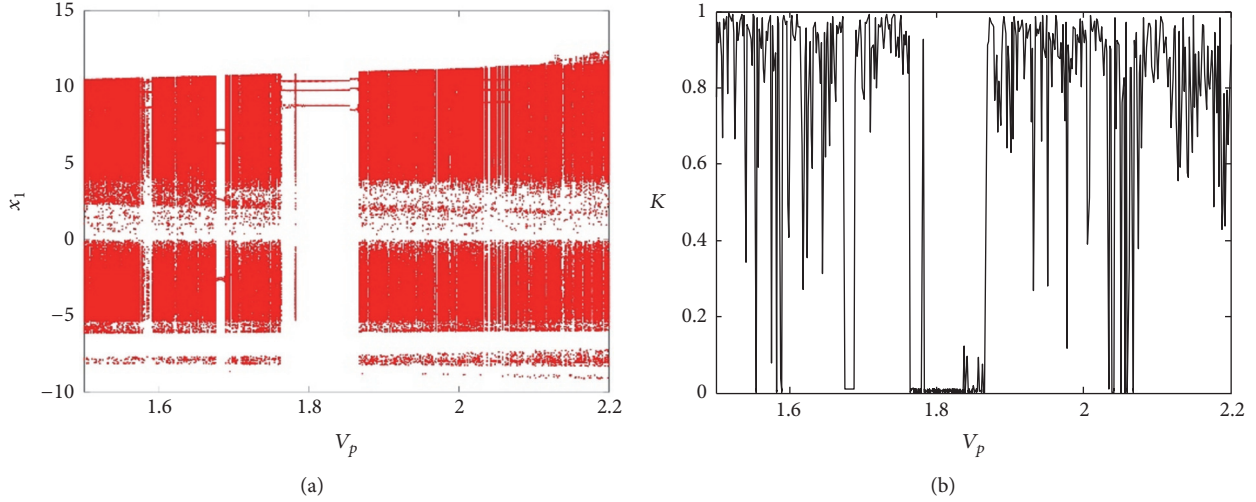


FIGURE 4: (a) Bifurcation diagram ( $V_p$  versus  $x_1$ ). (b)  $K$  versus  $V_p$ .

test. As can be seen in Figure 4 for the considered range  $V_p \in [1.5, 2.5]$ , a large variety of periodic and chaotic responses are observed.

Different from the observed behavior for the parameter  $b$ , it is possible to see in Figure 4 a tendency to instability of chaotic behavior to variations of  $V_p$ , indicating many areas of short intervals where the system maintains the chaotic behavior. Then periodic behaviors are encountered in the intervals of parameter  $V_p$  that are  $1.676 < V_p < 1.686$ ,  $1.765 < V_p < 1.78$ , or  $1.784 < b < 1.865$ .

**3.3. Influence of the Nonlinear Stiffness Term.** Now, the variation of the nonlinear stiffness term  $\alpha_3$  is considered, considering  $\alpha_3 \in [0.35, 1.5]$ . The same bifurcation diagram and 0-1 test analyses were carried out and presented in Figure 5.

Analyzing the bifurcation diagram (Figure 5(a)) and 0-1 test (Figure 5(b)), it is possible to observe that there are two regions where the variation of  $\alpha_3$  leads to periodic behavior. Such intervals are  $0.79 < \alpha_3 < 1.12$  and  $1.34 < \alpha_3 < 1.5$ . In the other areas, the system presented stability of chaotic behavior. Considering those results, it can be seen that the parameter ( $\alpha_3$ ) is the parameter with larger interval when  $K = 0$ , demonstrating that the appearance of chaotic behavior in this system is more sensitive to variation of this parameter.

**3.4. Pull-In.** The electric charge acting on a capacitor plate is composed of a continuous bias voltage and an alternating voltage. The DC component applies an electric force to a plate, thereby diverting it to a new equilibrium position, while an AC component vibrates the plate around the equilibrium position. The combined electric charge thus leads to a continuous increase in the deflection of the microstructure and, accordingly, an increase in the electrical forces in a positive feedback loop. This behavior continues until a physical contact is made with the stationary electrode. This phenomenon of structural instability is known as pull-in.

Now, the variation of the alternating voltage ( $V_i$ ) is considered, considering  $V_i \in [0, 10]$ .

Figure 6 shows a bifurcation diagram varying  $V_i$ .

Figure 6 shows the region in which the pull-in effect occurs, which is when  $V_i \approx 10$ .

#### 4. Time-Delayed Feedback Control

As originally suggested by the author of [24], continuous control input  $U$  stabilizing a chaotic oscillation is given by the difference between the current output and the past one as follows [17–19].

$$U = \kappa \{g[x_1(T - \tau), x_2(T - \tau)] - g[x_1(T), x_2(T)]\}, \quad (13)$$

where  $\tau$  is the time delay and  $k$  the feedback gain.

The terms  $g[x_1(T - \tau), x_2(T - \tau)]$  and  $g[x_1(T), x_2(T)]$  represent scalar output signals measured at the current time  $T$  and at the previous time  $(T - \tau)$ , respectively [16, 17, 24–26]. Since the control input (13) only depends on the output signal, the time delay  $\tau$  is adjusted to the period of a target unstable periodic orbit that is intended to be stabilized in a chaotic attractor, and the control input therefore converges to null after the controlled system is stabilized to the target orbit.

Assuming that the velocity of oscillation is measured as an output of nonlinear system (7), the control signal  $U$  is given as follows:

$$U = \kappa [x_2(T - \tau) - x_2(T)]. \quad (14)$$

The MEMS with control signal (14) is expressed in the following way:

$$\begin{aligned} \dot{x}_1 &= x_2 \\ \dot{x}_2 &= -\alpha_1 x_1 - \alpha_3 x_1^3 - b x_2 + \beta V^2 \frac{x_1}{(d^2 - x_1^2)^2} \\ &\quad + \kappa [x_2(T - \tau) - x_2(T)]. \end{aligned} \quad (15)$$

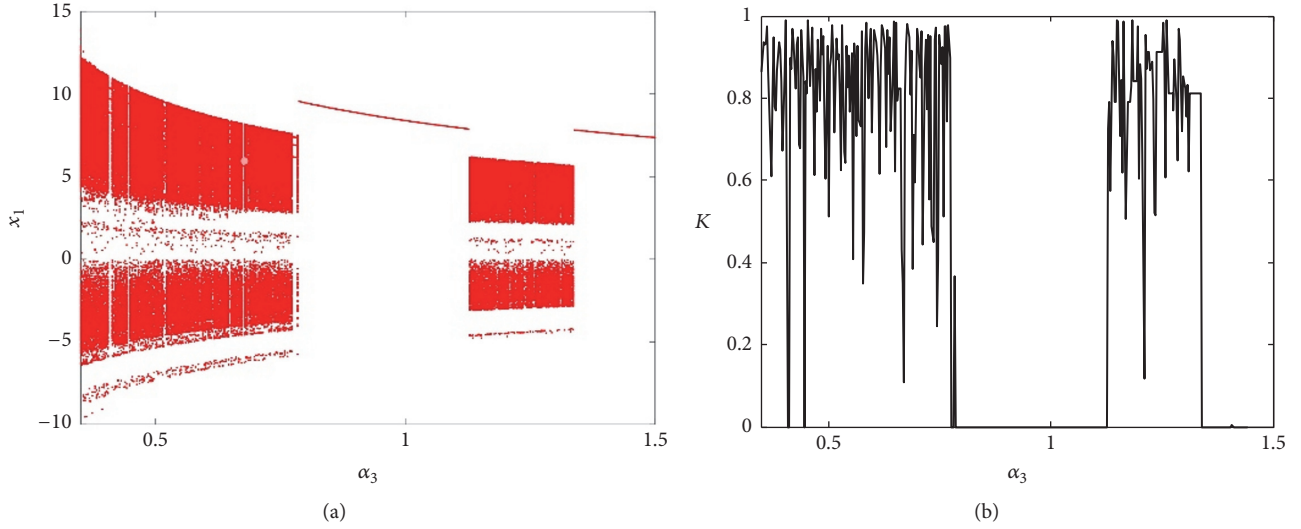


FIGURE 5: (a) Bifurcation diagram ( $\alpha_3$  versus  $x_1$ ). (b)  $\alpha_3$  versus  $K$ .

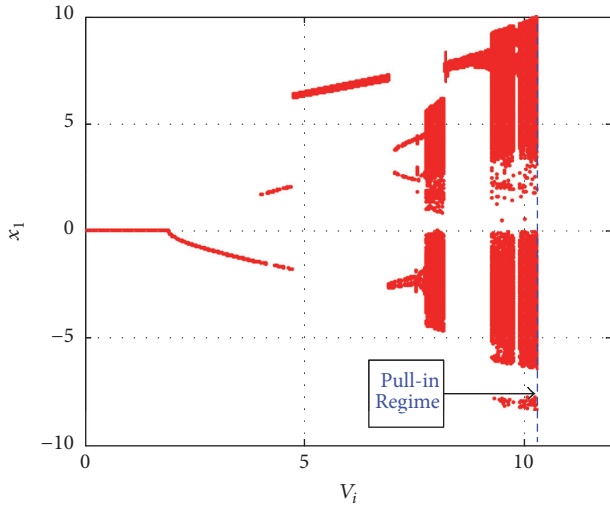


FIGURE 6: Bifurcation diagram with pull-in.

The time delay  $\tau$  and feedback gain  $\kappa$  are important control parameters that substantially affect the control performance. The time delay  $\tau$  is adjusted to  $\tau = 2\pi/\omega \approx 1$  to stabilize an orbit with the same frequency as the external force oscillating the system. Then, firstly, a variation of the control gain was carried out in Figure 7 in order to observe the behavior of the system. The system is chaotic from 0 to 0.3 approximately. After that, the behavior of the system becomes periodic.

Choose  $\kappa = 0.35$ , that is, a periodic behavior, Figure 8 shows the application of control (14).

It can be observed in Figure 8(c) that the time-delayed control was efficient in leading the system to a periodic orbit. However, for the cases where it is desired to take the system to a previously defined orbit, the control may not be the most suitable. For these mentioned cases, in the next section the sliding mode control will be considered.

## 5. Proposed Sliding Mode Control (SMC)

As can be seen in the previous section, the time delay control took the system from a chaotic behavior to a periodic attractor of the system. In this section, the case of imposing the desired orbit where the time delay control cannot be applied will be considered. For this case the sliding mode control is considered.

Consider now (8) in the form

$$\begin{aligned}\dot{x}_1 &= x_2 \\ \dot{x}_2 &= -\alpha_1 x_1 - \alpha_3 x_1^3 - b x_2 + \beta V^2 \frac{x_1}{(d^2 - x_1^2)^2} + U,\end{aligned}\quad (16)$$

where  $U$  is sliding mode control signal.

Define the desired trajectory errors as

$$e = \begin{bmatrix} x_1 - x_1^* \\ x_2 - x_2^* \end{bmatrix}, \quad (17)$$

where  $x_1^*$  is a desired trajectory; the dynamic equations of these errors (17) can be obtained as

$$\begin{aligned}\dot{e}_1 &= e_2 \\ \dot{e}_2 &= -\alpha_1 (e_1 - x_1^*) - \alpha_3 (e_1 - x_1^*)^3 - b (e_1 - x_2^*) \\ &\quad + \beta V^2 \frac{(e_1 - x_1^*)}{(d^2 - (e_1 - x_1^*))^2} + U.\end{aligned}\quad (18)$$

For the sliding mode control field, the sliding surface is generally taken to be [19, 20, 27]

$$s = e_1 - \lambda e_2. \quad (19)$$

The existence of the sliding mode requires the following conditions to be satisfied:

$$s = e_1 - \lambda e_2 \quad (20)$$

$$\dot{s} = \dot{e}_1 - \lambda \dot{e}_2,$$

where  $\lambda$  represents a real number.

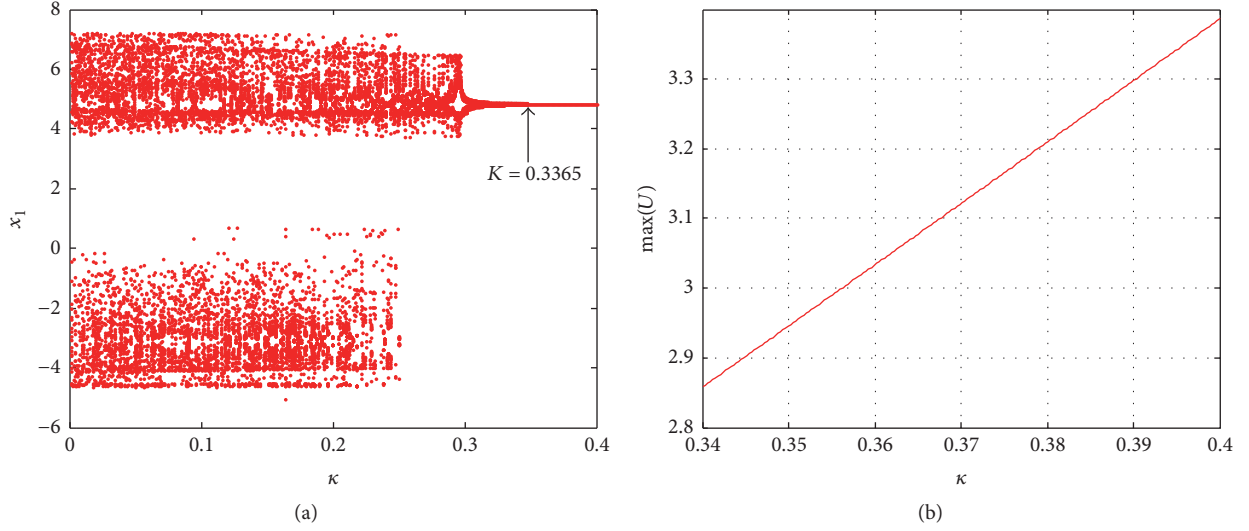


FIGURE 7: (a) Bifurcation diagram for control gain ( $\kappa$ ). (b) Variation of the control signal  $U$  for the gain variation ( $\kappa$ ).

Equation (19) defines the output of the sliding mode control controller, while the reaching law is given by [27]

$$U = \begin{cases} U_{\max} & \text{if } \frac{s}{\phi} < -1 \\ -U_{\max} & \text{if } \frac{s}{\phi} > 1 \\ K_c s & \text{if } -1 < \frac{s}{\phi} < 1, \end{cases} \quad (21)$$

where  $\phi$  is layer thickness of the control,  $K$  is a proportional gain, and  $U_{\max}$  is control of the saturation value.

For  $K_c$  determination, the Lyapunov function of the system is considered, defined as

$$V = \frac{1}{2} s^2. \quad (22)$$

The first derivative of this system with respect to time can be expressed as

$$\begin{aligned} \dot{V} &= \dot{s}s = s [\dot{e}_2 + \lambda \dot{e}_1] = s \left[ -\alpha_1 (e_1 - x_1^*) \right. \\ &\quad - \alpha_3 (e_1 - x_1^*)^3 - b(e_1 - x_2^*) \\ &\quad \left. + \beta V^2 \frac{(e_1 - x_1^*)}{(d^2 - (e_1 - x_1^*))^2} + KU + \lambda e_2 \right] = s [K_c U] \\ &\leq -K_c |s| \end{aligned} \quad (23)$$

If  $K_c > 0$  is selected, then the reaching condition ( $s\dot{s} < 0$ ) is always satisfied. Therefore, system (8) can be stabilized to a desired trajectory  $x_1^*(T)$ .

Defining the desired orbits to periodic orbits obtained with the time delay control of Figure 8(c), they are obtained through the use of Fourier series calculated numerically as

$$\begin{aligned} x_1^* &= 4.099049 - 0.80068 \cos(2\pi T) \\ &\quad + 0.123057 \sin(2\pi T) - 0.22686 \cos(4\pi T) \\ &\quad - 0.06764 \sin(4\pi T) + 0.016746 \cos(6\pi T) \\ &\quad + 0.002594 \sin(6\pi T) + 0.001333 \cos(8\pi T) \\ &\quad + 0.001167 \sin(8\pi T) \\ x_2^* &= 0.060495 + 0.773184 \cos(2\pi T) \\ &\quad + 5.030938 \sin(2\pi T) - 0.85001 \cos(4\pi T) \\ &\quad + 2.850889 \sin(4\pi T) + 0.048871 \cos(6\pi T) \\ &\quad - 0.31566 \sin(6\pi T) + 0.029304 \cos(8\pi T) \\ &\quad - 0.0335 \sin(8\pi T) \end{aligned} \quad (24)$$

and the parameters  $\lambda = 4$ ,  $K_c = 1000$ ,  $\phi = 10^{-3}$ , and  $U_{\max} = 500$  are considered. Figure 9 shows the application of the sliding mode control in the MEMS problem.

As can be seen in Figure 9(b), the proposed control (21) was efficient and it led system (16) from the initial state  $x_{1_0}$  to desired state  $x_1^*$ .

Figure 9(a) shows the difference between the state obtained with the control  $U$  and the desired state  $x_1^*$ , as it is seen that the control took approximately 1.65 T to stabilize the system in the desired orbit. In addition, Figure 9(c) presented the phase portrait for controlled systems (16), demonstrating that the system is periodic.

## 6. Conclusions

In this work, the dynamical analysis and control of the MEMS problem were investigated and discussed, contributing to

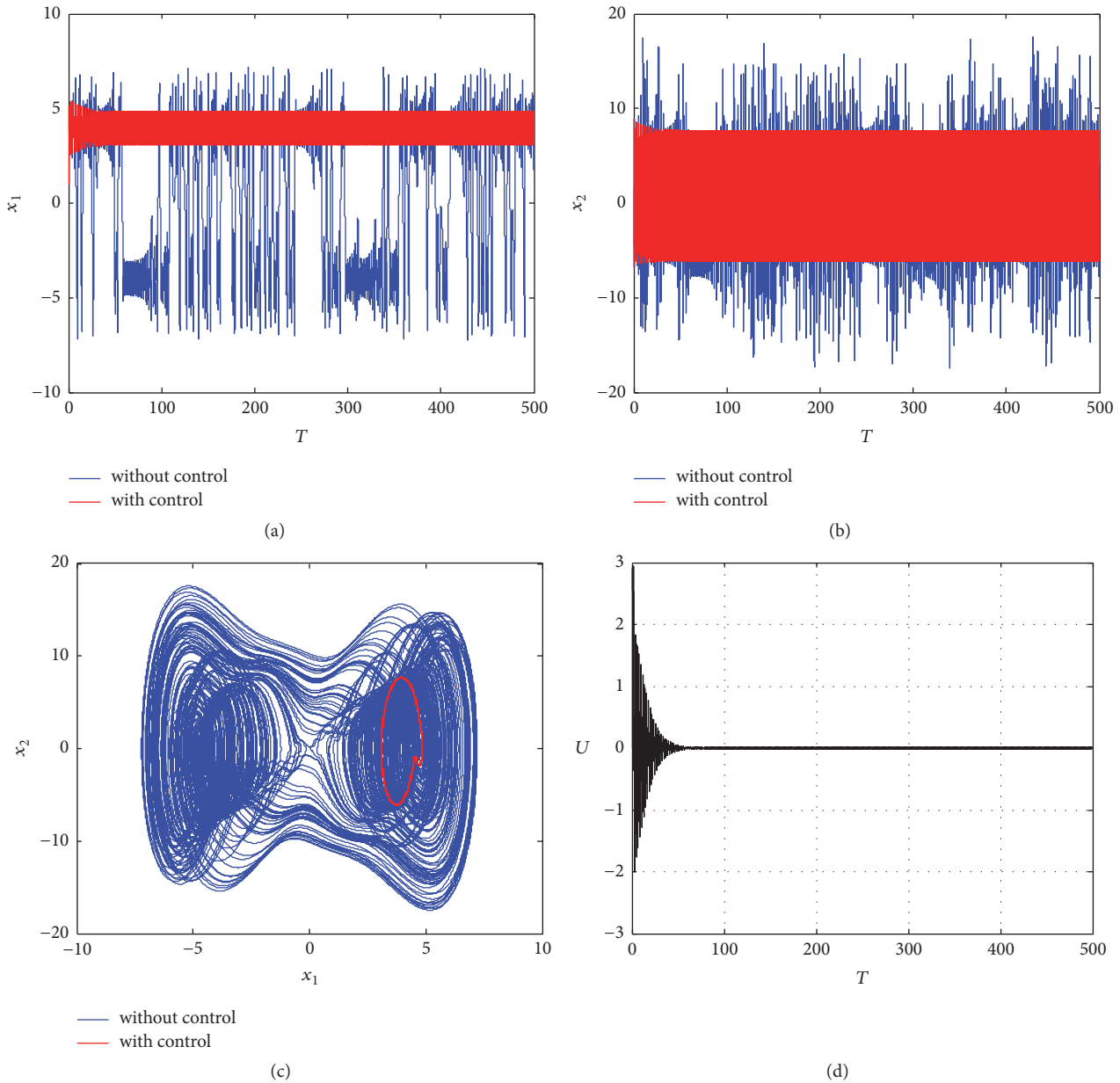


FIGURE 8: (a) Displacement. (b) Velocity. (c) Phase portrait. (d) Control signal.

the analysis of the influence of the parameters (damping coefficient, polarization of the voltage, and nonlinear stiffness term) and the design of two control techniques to control the chaotic behavior of the MEMS. With the presented numerical results, it is expected that such results contribute to new information that supports the physical assembly of a MEMS with behaviors close to those desired or for the cases of control application that can contribute to the control project.

Numerical simulations showed the existence of chaotic behavior for some regions in the parameter space of the damping, the polarization voltage, and the nonlinear stiffness term. Chaos was characterized by applying 0-1 test. The bifurcation diagrams were constructed to explore the qualitative behavior of the system.

In order to suppress the chaotic motion, the time-delayed feedback control and sliding mode control techniques were projected. The efficiency of the technique was demonstrated through numerical simulations in order to eliminate the chaotic behavior of the system. As could be seen in Figure 8(c), the time-delayed control led the system to one of the periodic attractors of the system, and we only used the control signal until the system stabilizes in the periodic orbit (see Figure 8(d)).

As the time-delayed control is not designed to take the system to any previously defined orbit, an alternative is the sliding mode control application. As could be seen in Figure 9(c), the sliding mode control was efficient in taking the system to the same periodic orbit obtained by the

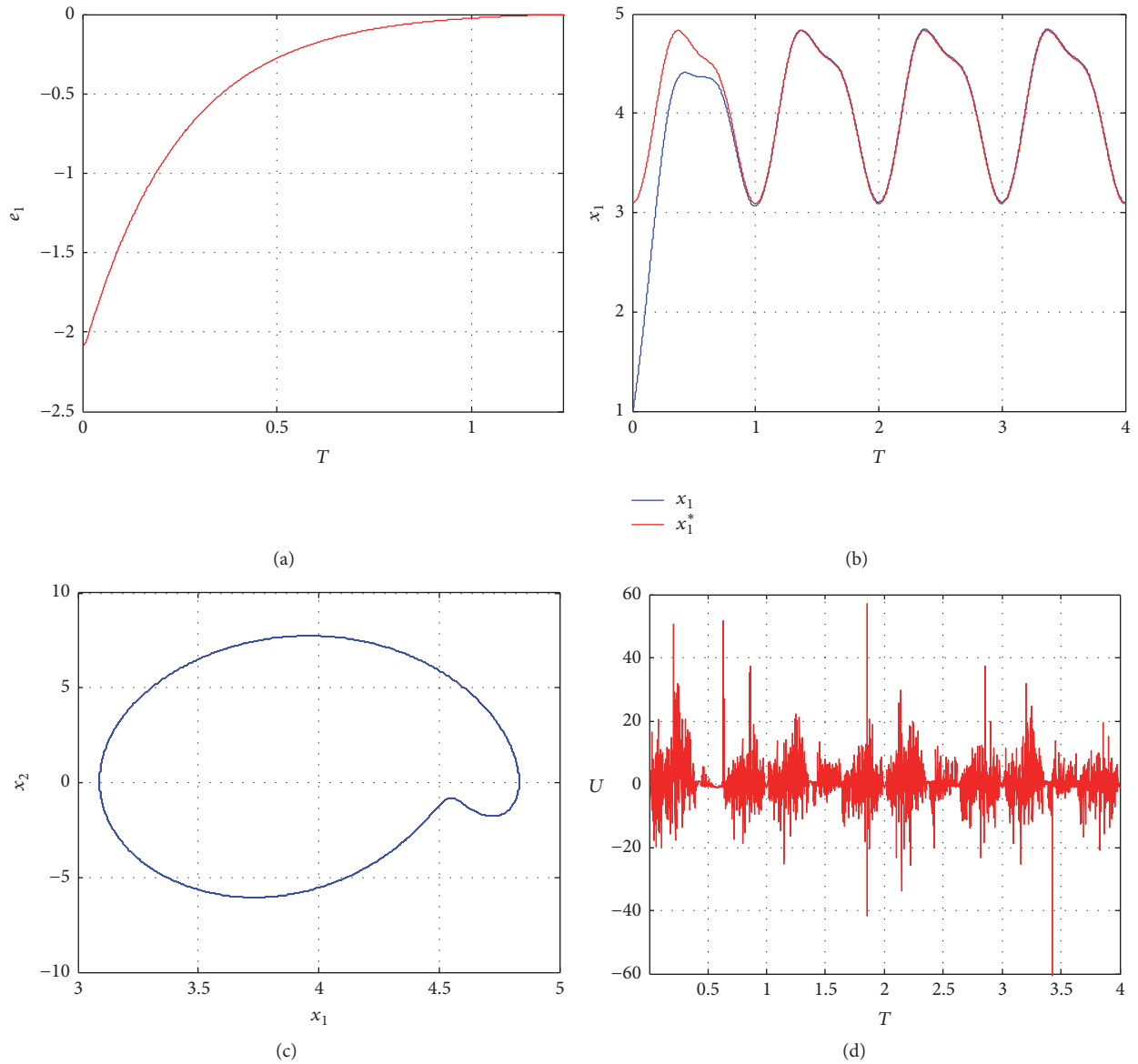


FIGURE 9: (a) Desired trajectory error ( $e_1$ ). (b) Displacement ( $x_1^*$  is the desired trajectory and  $x_1$  is displacement with proposed control (20)). (c) Phase portrait for controlled systems. (d) Control signal.

time-delayed control. However, when the control signals of Figures 8(d) and 9(d) are compared with each other, it can be observed that the sliding mode control has to maintain a control signal to keep the system in the periodic orbit, generating a control cost superior to the control cost of the time-delayed control.

Thus, it is possible to conclude that the time delay is an excellent option when the objective is to take the system to a periodic orbit with the lowest cost of control. Furthermore, the sliding mode control is an option to be considered in order to impose the desired orbit.

In future works, the efficiency of control techniques will be compared to dynamical analyses of the system with fractional-order derivatives. In addition, the analysis of the

applicability of the control in an analogous experimental model is carried out, considering the control by the electrical voltage similar to that used in [15] or the control through the use of intelligent materials (SMA) as used in [18, 19].

### Data Availability

The data used to support the findings of this study are available from the corresponding author upon request.

### Conflicts of Interest

The authors declare that there are no conflicts of interest regarding the publication of this paper.

## Acknowledgments

The authors acknowledge support by CNPq (Grant 447539/2014-0), CAPES, and all Brazilian research funding agencies.

## References

- [1] D. B. Blocher, A. T. Zehnder, and R. H. Rand, "Entrainment of micromechanical limit cycle oscillators in the presence of frequency instability," *Journal of Microelectromechanical Systems*, vol. 22, no. 4, Article ID 6478863, pp. 835–845, 2013.
- [2] D. Blocher, R. H. Rand, and A. T. Zehnder, "Analysis of laser power threshold for self oscillation in thermo-optically excited doubly supported MEMS beams," *International Journal of Non-Linear Mechanics*, vol. 57, pp. 10–15, 2013.
- [3] M. Pandey, R. H. Rand, and A. T. Zehnder, "Frequency locking in a forced Mathieu-van der Pol-Duffing system," *Nonlinear Dynamics*, vol. 54, no. 1-2, pp. 3–12, 2008.
- [4] K. Aubin, M. Zhalutdinov, T. Alan et al., "Limit cycle oscillations in CW laser-driven NEMS," *Journal of Microelectromechanical Systems*, vol. 13, no. 6, pp. 1018–1026, 2004.
- [5] A. M. Tusset, J. M. Balthazar, D. G. Bassinello, J. Pontes, and J. L. Felix, "Statements on chaos control designs, including a fractional order dynamical system, applied to a MEMS comb-drive actuator," *Nonlinear Dynamics*, vol. 69, no. 4, pp. 1837–1857, 2012.
- [6] A. M. Tusset, Á. M. Bueno, C. B. Nascimento, M. Dos Santos Kaster, and J. M. Balthazar, "Nonlinear state estimation and control for chaos suppression in MEMS resonator," *Shock and Vibration*, vol. 20, no. 4, pp. 749–761, 2013.
- [7] S. Sabarathinam and K. Thamilaran, "Implementation of analog circuit and study of chaotic dynamics in a generalized Duffing-type MEMS resonator," *Nonlinear Dynamics*, vol. 87, no. 4, pp. 2345–2356, 2017.
- [8] H. S. Haghighi and A. H. D. Markazi, "Chaos prediction and control in MEMS resonators," *Communications in Nonlinear Science and Numerical Simulation*, vol. 15, no. 10, pp. 3091–3099, 2010.
- [9] G. A. Gottwald and I. Melbourne, "A new test for chaos in deterministic systems," *Proceedings of the Royal Society A Mathematical, Physical and Engineering Sciences*, vol. 460, no. 2042, pp. 603–611, 2004.
- [10] G. A. Gottwald and I. Melbourne, "Testing for chaos in deterministic systems with noise," *Physica D: Nonlinear Phenomena*, vol. 212, no. 1-2, pp. 100–110, 2005.
- [11] D. Bernardini and G. Litak, "An overview of 0-1 test for chaos," *Journal of the Brazilian Society of Mechanical Sciences and Engineering*, vol. 38, no. 5, pp. 1–8, 2015.
- [12] D. Bernardini, G. Rega, G. Litak, and A. Syta, "Identification of regular and chaotic isothermal trajectories of a shape memory oscillator using the 0-1 test," *Proceedings of the Institution of Mechanical Engineers, Part K: Journal of Multi-body Dynamics*, vol. 227, no. 1, pp. 17–22, 2013.
- [13] G. Litak, A. Syta, and M. Wiercigroch, "Identification of chaos in a cutting process by the 0-1 test," *Chaos, Solitons & Fractals*, vol. 40, no. 5, pp. 2095–2101, 2009.
- [14] G. Litak, D. Bernardini, A. Syta, G. Rega, and A. Rysak, "Analysis of chaotic non-isothermal solutions of thermomechanical shape memory oscillators," *The European Physical Journal Special Topics*, vol. 222, no. 7, pp. 1637–1647, 2013.
- [15] K. Pyragas and A. Tamaševičius, "Experimental control of chaos by delayed self-controlling feedback," *Physics Letters A*, vol. 180, no. 1-2, pp. 99–102, 1993.
- [16] J. M. Balthazar, A. M. Tusset, S. L. T. De Souza, and A. M. Bueno, "Microcantilever chaotic motion suppression in tapping mode atomic force microscope," *Proceedings of the Institution of Mechanical Engineers, Part C: Journal of Mechanical Engineering Science*, vol. 227, no. 8, pp. 1730–1741, 2013.
- [17] K. D. S. Rodrigues, J. M. Balthazar, A. M. Tusset, B. R. de Pontes, and Á. M. Bueno, "Preventing Chaotic Motion in Tapping-Mode Atomic Force Microscope," *Journal of Control, Automation and Electrical Systems*, vol. 25, no. 6, pp. 732–740, 2014.
- [18] D. D. Costa and M. A. Savi, "Chaos control of an SMA-pendulum system using thermal actuation with extended time-delayed feedback approach," *Nonlinear Dynamics*, pp. 1–13, 2018.
- [19] F. C. Janzen, J. M. Balthazar, A. M. Tusset, R. T. Rocha, and J. J. De Lima, "Angular positioning and vibration control of a slewing flexible control by applying smart materials and sliding modes control," in *Proceedings of the ASME 2017 International Design Engineering Technical Conferences and Computers and Information in Engineering Conference, IDETC/CIE 2017*, vol. 8, Cleveland, Oh, USA, August 2017.
- [20] H.-T. Yau, C.-C. Wang, C.-T. Hsieh, and C.-C. Cho, "Nonlinear analysis and control of the uncertain micro-electro-mechanical system by using a fuzzy sliding mode control," *Computers & Mathematics with Applications. An International Journal*, vol. 61, no. 8, pp. 1912–1916, 2011.
- [21] C.-C. Wang, "Non-periodic and chaotic response of three-multilobe air bearing system," *Applied Mathematical Modelling: Simulation and Computation for Engineering and Environmental Systems*, vol. 47, pp. 859–871, 2017.
- [22] F. C. Moon, *Applied Dynamics-With Applications to Multibody and Mechatronic Systems*, Wiley-Interscience, New York, NY, USA, 1998.
- [23] D. G. Bassinello, J. M. Balthazar, A. M. Tusset, and V. Piccirillo, "Dynamic Analysis of a Fractional-Order MEMS System Using 0-1 Test," in *Proceedings of the ASME 2016 International Design Engineering Technical Conferences and Computers and Information in Engineering Conference*, pp. V008T10A014–V008T10A014, 2016.
- [24] K. Pyragas, "Continuous control of chaos by self-controlling feedback," *Physics Letters A*, vol. 170, no. 6, pp. 421–428, 1992.
- [25] K. Yamasue and T. Hikihara, "Control of microcantilevers in dynamic force microscopy using time delayed feedback," *Review of Scientific Instruments*, vol. 77, no. 5, Article ID 053703, pp. 1–6, 2006.
- [26] H. Salarieh and A. Alasty, "Control of chaos in atomic force microscopes using delayed feedback based on entropy minimization," *Communications in Nonlinear Science and Numerical Simulation*, vol. 14, no. 3, pp. 637–644, 2009.
- [27] V. I. Utkin, *Sliding Modes in Control Optimization*, Springer-Verlag, Berlin, Germany, 1992.

## Research Article

# Dynamic Characteristics of Blade with Viscoelastic Damping Block Based on Complex Eigenvalue Method

Jiao Wang <sup>1,2</sup>, Yue-hao Zhang,<sup>3</sup> Tao Yu,<sup>1,2</sup> and Qing-kai Han <sup>4</sup>

<sup>1</sup>School of Mechatronics and Automobile Engineering, Yantai University, Yantai 264005, China

<sup>2</sup>Key Laboratory of Advanced Manufacturing and Control Technology in Universities of Shandong, Yantai 264005, China

<sup>3</sup>Engineering Training Center, Yantai University, Yantai 264005, China

<sup>4</sup>Dalian Universities of Technology, Dalian 116024, China

Correspondence should be addressed to Jiao Wang; [zoe\\_wjiao@163.com](mailto:zoe_wjiao@163.com)

Received 16 September 2017; Revised 2 February 2018; Accepted 25 February 2018; Published 5 April 2018

Academic Editor: Paulo B. Gonçalves

Copyright © 2018 Jiao Wang et al. This is an open access article distributed under the Creative Commons Attribution License, which permits unrestricted use, distribution, and reproduction in any medium, provided the original work is properly cited.

A novel method for vibration suppression is proposed, adding a viscoelastic damping block to the root of the blade. The dynamical equation for a rotational viscoelastic damping block-blade (VE-blade) in a centrifugal force field and aerodynamic force field is established to calculate the dynamical natural frequency and responses of the VE-blade. Complex modulus model is applied to represent the constitutive law of viscoelastic material and shear force acting on the VE-blade formulates the effect of viscoelastic damping at the root interfaces. The dynamical equation of the system is established and the Galerkin method is used to discretize the partial differential equations to a 3-DOF system so as to compute the dynamic natural frequencies and responses of the VE-blade. Then the differential equations of motion with 3-DOF are numerically solved by using complex eigenvalue method. A cantilever VE-blade is simplified according to testing the first three natural frequencies of the real blade to obtain geometric parameters of cantilever beam. The effects of various parameters including thickness, storage modulus, loss factor of viscoelastic damping block, and rotating speed on natural frequency and modal damping ratio of VE-blade are discussed in detail.

## 1. Introduction

Blade is an important component of turbomachinery such as aeroengine, gas turbine, and high-end axial flow compressor. Under the condition of multifield coupling, the blade is subjected to relatively severe fluid and heat coupling excitation, and the resonance is inevitably generated due to its own dense natural frequency and complex vibration mode. In engineering practice, even to meet the requirements of the static strength and resistance to low cycle fatigue design, but due to the high stress level and the possible high frequency resonance, blade is still prone to high cycle fatigue failure. Therefore, the blade in the existing structure cannot be further optimized, and it is imperative to adopt an additional damping method to achieve vibration damping of the blade and improve its antivibration fatigue capability.

The vibration and noise can be inhibition in quite a wide frequency band with the high damping characteristics

of viscoelastic materials [1, 2]. The damping mechanism of viscoelastic damping material mainly depends on the internal friction polymer to dissipate vibration energy. The greater the internal friction of the polymer, the better the damping performance. But internal friction cannot be indefinitely increased, the main effect of polymer friction is the temperature and frequency, and each kind of viscoelastic damping material has its best working temperature and frequency range [3]. In recent years, the use of viscoelastic materials to improve the damping performance and the dynamic characteristics of components getting the people's attention, especially the thin-walled components, has been applied to aircraft engine, such as compressor blade, disc, and drum [4–7]. Now studies have shown that viscoelastic material with a high damping performance can effectively achieve damping vibration of structure and thus improve the component antivibration fatigue. With it stick on the blade dovetail structure as a damping layer (Figure 1), it will produce cyclical

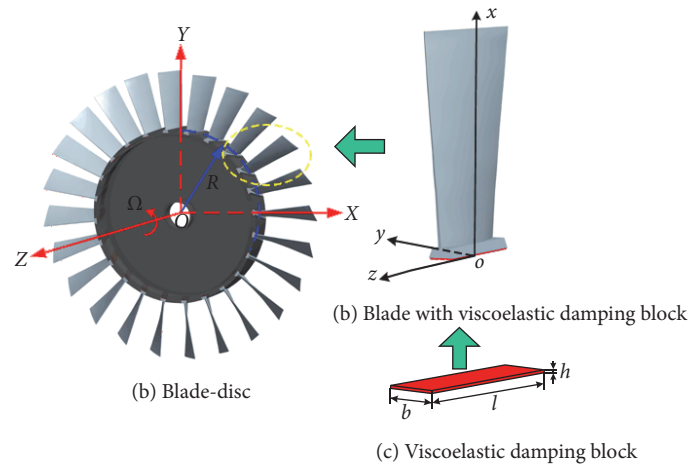


FIGURE 1: Schematic diagram of the blade-disc with viscoelastic damping block.

tensile deformation under the vibration of the component, so the phase difference between its stress and strain can dissipate energy dissipation and suppress the vibration of the blade, which has important engineering value.

The viscoelastic damping technology has been applied to turbine blades and other key components. Deng et al. [8] used cantilever with metal rubber block at its root to simulate the blade damping vibration. Li et al. [9] studied on new ways to suppress the resonance of fan's blade with the shoulder. The results show that the root rubber damper structure suppression effect on maximum vibration stress mode of blade tenons is obvious. Balmes et al. [4] found that the viscoelastic constrained layer improves the damping of aeroengine disks and changes its natural frequency and through experimental testing and numerical analysis verify that the damping performance of viscoelastic materials is affected by temperature. Miao [10] proposed that the natural frequency of the blade can be greatly reduced by applying nylon glue to the bottom of the blade root to meet the requirement of blade vibration. But the abnormal contact caused by irregular nylon glue and nonstandard assembly process easily leads to fretting wear and blade root fracture failure. Kocatürk [11] researched on the steady state responses of beam with elastic support under base excitation. Lagrange equation is adopted to establish the dynamic equation for the first two-order natural frequency and the results compared with the results obtained from Euler beam theory. This paper considers the effect of the viscoelastic damping and stiffness parameters on the steady state response, but not considering the effect of the friction on cantilever beam under elastic support, also does not consider the effect of rotational speed and the root of the cantilever fixed. Wang and Inman [12] studied the stiffness and damping of viscoelastic materials with frequency-dependent characteristics, which will affect the natural frequencies and responses of composite structures. Rafiee et al. [13] presented a critical review about dynamics, vibration, and control of rotating composite beams and blades. The active vibration control [14, 15] and passive control method [16] of the rotating beams and blades are introduced. Hosseini et al. [17] carried out the research on the

nonlinear forced response analytic solution of piezoelectric composite viscoelastic beam under the action of nonlinear elastic support. Euler beam theory, Kelvin-Voigt viscoelastic materials model, and Hamilton principle are adopted to establish the dynamics equation, and considering the effect of nonlinear elastic stiffness, piezoelectric damping and elastic damping on structure nonlinear forced response. Min et al. [18] applied active piezoelectric vibration control method to decrease the vibration of the blade considering rotational effects. Through experiments and finite element simulation, it is verified that the piezoelectric material can effectively reduce the vibration of the blade.

Therefore, attaching viscoelastic materials at the bottom of blade root as a new vibration damping measure can effectively avoid the vibration fatigue of blade and improve the surface quality and effectively resist the impact, abrasion, and erosion caused by the external object. However, the related vibration theory of the nonlinear dynamic model and the mathematical model of the blade with viscoelastic materials is not perfect. The stiffness and damping are significantly increased after applying viscoelastic damping materials, and they are the main parameters of viscoelastic damping structure dynamic characteristics. For the dynamic analysis of composite structure, mainly using the modal strain energy method [19], the complex eigenvalue method and the direct frequency response method. Rao et al. [20] studied the beam with constrained damping layer and initial stress using residual deformation beam element and solved the loss factor with direct frequency response method and modal strain energy method. Rikards et al. [21] analyzed the vibration and damping of sandwich beam and plate using complex eigenvalue method and approximate energy method. Ravi et al. [22] used the modal superposition method to study the dynamic response of the beam to local or all of the free damping layer and the constrained damping layer. Chen and Shi [23] studied the local passive constrained damping beam using modal strain energy method, to extract the modal strain energy in each layer and solve the loss factor. Wang et al. [24] analyzed the frequency and dynamic response of the reinforced composite plate with viscoelastic damping layer using

subspace iteration method and precise integration method. Analysis of the laminated plate and the laminated beam using damping matrix method, which combined Adams strain energy method with Raleigh damping model method, considered the dependence of the vibration frequency and temperature on the material properties and the dissipation coefficient of surface viscoelastic damping material established the frequency-dependent viscoelastic material damping matrix calculation method. Zhang and Chen [25] studied the damping characteristic of composite beam with viscoelastic material based on ANSYS using modal strain energy method and studied the influence of viscoelastic layer laying angle and position on the loss factor and natural frequency of the composite beam. Cortés and Elejabarrieta [26] used an iteration method to solve the eigenvalue and eigenvector of composite structure, obtained the eigenvalue and eigenvector of a static system without damping firstly, and then obtained the natural frequency and loss factor of composite plate structure using iteration method, the stiffness, and damping of composite plate structure change with frequency. Compare the result with obtained from modal strain energy method, which proved the accuracy of the iteration method.

In this paper, a general theory method for vibration suppression is proposed. The dynamical equation for a rotational cantilever VE-blade in a centrifugal force field and aerodynamic force field is established and the Galerkin method is used to discretize the partial differential equations to a 3-DOF system so as to compute the dynamic natural frequencies and responses of the VE-blade. Then the differential equations of motion with 3-DOF are numerically solved by using complex eigenvalue method. A cantilever VE-blade is simplified according to testing the first three natural frequencies of the real blade to obtain geometric parameters of cantilever beam. Compared with the experimental results, the rationality of the model is verified. The effects of viscoelastic damping material parameters such as thickness, storage modulus, loss factor, and rotational angular speed on the dynamic characteristics of VE-blade are further considered. The results show that increasing the thickness of the viscoelastic damping block, choosing the material with large storage modulus and loss factor can improve the modal damping ratio of the system and obtain better damping effect. With the increase of the rotational speed, the natural frequency of VE-blade increases gradually and the modal damping ratio decreases; indicating that with the increase of the rotational speed, the damping effect of the viscoelastic damping block decreases.

## 2. Theoretical Analysis

**2.1. Simplified Mechanical Model of VE-Blade.** Simplified VE-blade can be regarded as a cantilever beam structure. The structure of blade-disc as shown in Figure 1 consists of blades, disc, and viscoelastic damping block, placed at the bottom of the blade. OXYZ is the global coordinate system, point O is located in the center of the disc, and that rotates around the z-axis in angular velocity  $\Omega$ .

Take one blade from the blade-disc structure, set up local coordinate system  $oxyz$ , origin  $o$  at the bottom of the viscoelastic block, and  $R$  is the distance between  $O$  and  $o$ . Make

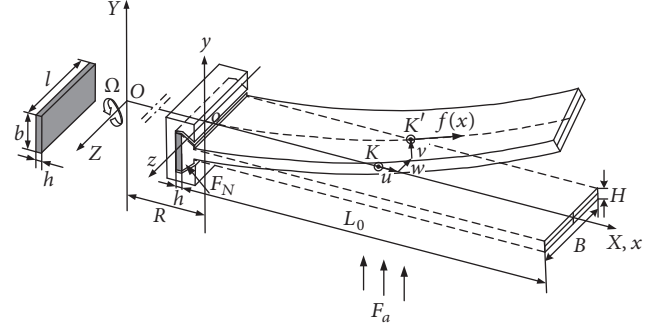


FIGURE 2: Schematic diagram of cantilever beam with viscoelastic damping block.

the first three-order natural frequency of the blade as the equivalent target; it can be simplified as a cantilever beam, as shown in Figure 2. The geometrical and material parameters of the blade are density  $\rho$ , elastic modulus  $E$ , Poisson's ratio  $\mu$ , length  $L_0$ , width  $B$ , thickness  $H$ , and cross-sectional area  $A$ . Geometrical and material parameters of viscoelastic damping block are length  $l$ , width  $b$ , thickness  $h$ , density  $\rho_1$ , energy storage modulus  $E_1$ , loss factor  $\eta$ , and Poisson's ratio  $\mu_1$ .

In general, viscoelastic materials have strong temperature and frequency dependence. The temperature is regarded as a constant in this paper. The complex Young's modulus of viscoelastic material is

$$E_v(\omega) = E_1(\omega) + E_2(\omega)i = E_1(\omega)(1 + i\eta(\omega)),$$

$$G_v(\omega) = \frac{E_v(\omega)}{2(1 + \mu_1)}, \quad (1)$$

where  $E_1(\omega)$  is the real part of  $E_v(\omega)$ , called the storage modulus,  $E_2(\omega)$  is the imaginary part of  $E_v(\omega)$ , called energy modulus,  $\eta(\omega) = E_2(\omega)/E_1(\omega)$  is loss factor;  $G_v(\omega)$  is complex shear modulus;  $\mu_1$  is poisson's ratio.

The viscoelastic damping block applied at the root of the blade is always in contact with the bottom of the blade and the bottom of the disc-slot. The movement of the blade produces tension, pressure, and shear force on the viscoelastic damping block [27]; it can free deformation in the length ( $z$ -axis) direction. Therefore, the stiffness and damping of the viscoelastic damping block are different in the thickness ( $x$ -axis) direction and width ( $y$ -axis) direction, where stiffness in  $x$ -axis direction is determined by the elasticity modulus, stiffness [28] in  $y$ -axis direction is determined by the shear modulus, respectively, as follows:

$$k_{vx} = \frac{Sk_T}{h} E_v(\omega),$$

$$k_{vy} = \frac{Sk_s}{h} G_v(\omega), \quad (2)$$

where  $k_T$ ,  $k_s$  are shape factor of  $k_{vx}$ ,  $k_{vy}$ , respectively.

In this paper, it is difficult to determine some parameters that affect  $k_T$  and  $k_s$  value, so  $k_T = k_s \cong 1$ .

Although there will be some error, it has little effect on the calculation results. Therefore, the acting point of force in the place where viscoelastic damping block and blade contact, the

applied force on blade in tension and compression ( $x$ -axis), and shear ( $y$ -axis) direction produce by viscoelastic damping block can be written as the multiplication of equivalent stiffness and displacement component, as follows:

$$\begin{aligned} F_{vx} &= k_{vx}u_v = \frac{bl}{h}E_1(1+i\eta)u_v, \\ F_{vy} &= k_{vy}v_v = \frac{blE_1}{2h(1+\mu_1)}(1+i\eta)v_v, \end{aligned} \quad (3)$$

where  $u_v = u(h, t)$  and  $v_v = v(h, t)$  are the displacement in  $x$  and  $y$  directions of the viscoelastic damping block acting point, respectively.

**2.2. Dynamic Equations of VE-Blade.** Newton mechanics method is adopted to establish the dynamic equations of VE-blade. In order to establish an effective dynamic model of VE-blade, the following assumptions are applied [29, 30]:

- (1) VE-blade simplified as cantilever beam, its transverse vibration is microvibration.
- (2) The material is isotropic, and the constitutive relation satisfies Hooke's law. The geometry parameters of cross section of blade and all cross section involved remain unchanged within the surface.
- (3) VE-blade is simplified as cantilever beam; it perpendicular to the cross section of neutral axis before deformation and still planes after deformation. Shear and torsion and warping effect are ignored.
- (4) Regardless the influence of surrounding medium damping and material internal damping of blade on vibration.
- (5) Regardless of the Coriolis effect, ignore the longitudinal displacement  $u$  along the axis of rotation direction displacement  $w$  of the beam.

$K$  is a point on the central axis of cantilever beam microelement  $dx$ , moving to the point  $K'$  after deformation, as shown in Figure 2. The position vector of microelement  $dx$  after deformation in inertial coordinate system  $OXYZ$  is expressed in  $\mathbf{r}_O$ .

$$\mathbf{r}_O = (R+x)\mathbf{i} + v(x, t)\mathbf{j}, \quad (4)$$

where  $\mathbf{i}$ ,  $\mathbf{j}$ , respectively, represent the unit vector in  $OX$ ,  $OY$  axes.

The inertial velocity vector and acceleration vector of microelement  $dx$  can be expressed as

$$\begin{aligned} \mathbf{v}_a &= v_x\mathbf{i} + v_y\mathbf{j}, \\ \mathbf{a}_a &= a_x\mathbf{i} + a_y\mathbf{j}, \end{aligned} \quad (5)$$

where

$$\begin{aligned} v_x &= -v(x, t)\Omega, \\ v_y &= (R+x)\Omega + \frac{\partial v(x, t)}{\partial t}, \end{aligned}$$

$$\begin{aligned} a_x &= -\Omega^2(R+x) - 2\Omega\frac{\partial v(x, t)}{\partial t}, \\ a_y &= \frac{\partial v^2(x, t)}{\partial t^2} - \Omega^2v. \end{aligned} \quad (6)$$

Based on the principle of Newton, the dynamic equation of VE-blade is established. Take a microelement  $dx$  at coordinates  $x$  in the simplified cantilever; it is force analysis as shown in Figure 3 [30]. The forces acting on the microelement have shear force  $Q(x, t)$ , centrifugal load  $f(x)$ , aerodynamic load  $F_a(t)$ , and bending moment  $M(x, t)$ . The deformations are  $(\partial Q(x, t)/\partial x)dx$ ,  $df(x)$ ,  $dF_a(t)$ , and  $dM(x, t)$ , respectively.

Equation is established according to the force balance and moment balance theory. Only consider the transverse vibration according to the assumption. Therefore, consider the force balance in  $y$  direction, and then introduce the viscoelastic tangential force acting on blade root. The relational expression between transverse vibration displacement  $v(x, t)$  and transverse forces is

$$\begin{aligned} Q(x, t) - \left[ Q(x, t) + \frac{\partial Q(x, t)}{\partial x}dx \right] + F_a(t)dx \\ - F_{vy}D(x-h)dx = \rho A dx a_y, \end{aligned} \quad (7)$$

where  $Q(x, t)$  is the shear force on the cross section and  $F_a(t)$  is the aerodynamic loading acted on pressure surface of blade. It generated by the first stage stator blade wake excitation expressed as

$$F_a(t) = F_{a0} \cos(jN\Omega t), \quad j = 1, 2, 3, \dots, \quad (8)$$

where  $F_{a0}$  is amplitude of aerodynamic force,  $j$  is the order of harmonic force, and  $N$  is the number of blades in the upstream cascade row.

$D(x-h)$  is Dirac function and meets  $D(x) = \{+\infty, x = 0; 0, x \neq 0\}$  and  $\int_{-\infty}^{+\infty} D(x)dx = 1$ .  $D(x-h)$  represents the viscoelastic force acting at the root of blade.

Substituting  $a_y = \partial v^2(x, t)/\partial t^2 - \Omega^2v$  into (7), divided by  $dx$ , we have

$$\begin{aligned} \frac{\partial Q(x, t)}{\partial x} = \rho A \Omega^2 v - \rho A \frac{\partial v^2(x, t)}{\partial t^2} + F_a(t) \\ - \frac{blE_1}{2h(1+\mu)}(1+i\eta)v_v D(x-h). \end{aligned} \quad (9)$$

Point  $K'$  on neutral axis of microelement meets moment balance theory, and we have the rotation equation of microelement

$$\begin{aligned} \left( M(x, t) + \frac{\partial M(x, t)}{\partial x}dx \right) - M(x, t) - Q(x, t)dx \\ - f(x)\frac{\partial v(x, t)}{\partial t}dx - F_a(t)dx\frac{dx}{2} = 0, \end{aligned} \quad (10)$$

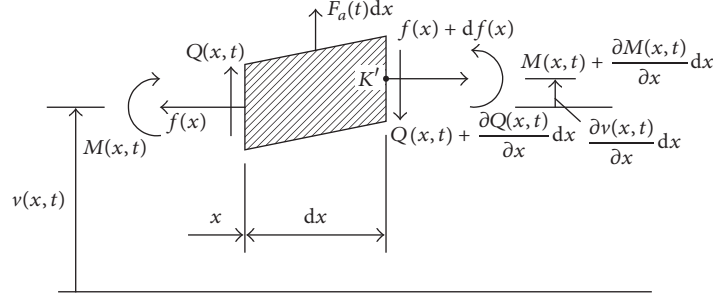


FIGURE 3: Mechanical schematics of blade microelement.

where  $f(x)$  is the axial centrifugal load expressed as

$$\begin{aligned} f(x) &= \int_x^L \rho A \Omega^2 (R+x) dx \\ &= -\frac{1}{2} \rho A \Omega^2 (x-L)(x+2R+L). \end{aligned} \quad (11)$$

Omit quadratic term contains  $dx$  and simplified equation (10) to

$$Q(x,t) = \frac{\partial M(x,t)}{\partial x} - f(x) \frac{\partial v(x,t)}{\partial x}. \quad (12)$$

According to assumption (1), under the condition of small deformation, the bending moment and deflection are the following relations:

$$M(x,t) = EI \frac{\partial^2 v(x,t)}{\partial x^2}. \quad (13)$$

Substitute (12) and (13) into (9), based on the assumption of cantilever beam, we have the transverse vibration differential equation of system

$$\begin{aligned} EI \frac{\partial^4 v(x,t)}{\partial x^4} + \rho A \frac{\partial^2 v(x,t)}{\partial t^2} \\ + \frac{1}{2} \rho A \Omega^2 (x-L)(x+2R+L) \frac{\partial^2 v(x,t)}{\partial x^2} \\ - \rho A \Omega^2 (x+R) \frac{\partial v(x,t)}{\partial x} - \rho A \Omega^2 v(x,t) \\ + \left( \frac{blE_1}{2h(1+\nu)} (1+i\eta) \right) v_v D(x-h) = F_a(t). \end{aligned} \quad (14)$$

### 3. Solution Method to Dynamic Equation of VE-Blade

**3.1. Galerkin Discretization.** The material parameters of the viscoelastic damping block can be regarded as a constant, and the dynamic equation of VE-blade can be discrete using Galerkin method and then can be solved in the frequency domain. In the given cantilever boundary condition, the solution of (14) is

$$v(x,t) = \sum_{i=1}^n \phi_i(x) q_i(t), \quad (15)$$

where  $\phi_i(x)$  ( $i = 1, 2, \dots, n$ ) is the  $i$ th order mode shape function and  $q_i(t)$  is the corresponding generalized coordinates.

By the cantilever beam assumption, the eigenfunction as follows:

$$\begin{aligned} \phi_i(x) &= \cosh \frac{\lambda_i}{L} x - \cos \frac{\lambda_i}{L} x \\ &- \frac{\cosh \lambda_i + \cos \lambda_i}{\sinh \lambda_i + \sin \lambda_i} \left( \sinh \frac{\lambda_i}{L} x - \sin \frac{\lambda_i}{L} x \right), \end{aligned} \quad (16)$$

where  $\lambda_i$  is eigenvalue and satisfies  $\cos(\lambda_i) \cosh(\lambda_i) + 1 = 0$ ;  $L$  is the length of beam and satisfies  $L = L_0 + h$ .

By the orthogonality of the vibration mode function,  $\int_0^L \phi_i(x) \phi_k(x) dx = \{0, (k \neq i); L, (k = i)\}$ ,  $\int_0^L \phi_i^{(4)}(x) \phi_k(x) dx = \{0, (k \neq i); \lambda_i^4/L^3, (k = i)\}$ . Discretize the original system equation. Substitute (15) into (14), multiplied by  $\phi_k(x)$  on both sides of the equation, integral on  $x$  in the range  $[0, L]$  gives

$$\begin{aligned} EI \sum_{i=1}^n q_i(t) d_1 + \rho A \sum_{i=1}^n \ddot{q}_i(t) d_2 + \frac{1}{2} \rho A \Omega^2 \sum_{i=1}^n q_i(t) d_3 \\ - \rho A \Omega^2 \sum_{i=1}^n q_i(t) d_4 - \rho A \Omega^2 \sum_{i=1}^n q_i(t) d_2 \\ + \left( \frac{blE_1}{2h(1+\nu)} (1+i\eta) \right) \sum_{i=1}^n q_i(t) d_5 \\ = \int_0^L F_{a0} \phi_k(x) \cos(jN\Omega t) dx, \quad (k = 1, 2, \dots, n), \end{aligned} \quad (17)$$

where  $d_1 = \int_0^L \phi_i^{(4)}(x) \phi_k(x) dx$ ,  $d_2 = \int_0^L \phi_i(x) \phi_k(x) dx$ ,  $d_3 = \int_0^L (x-L)(x+2R+L) \phi_i^{(2)}(x) \phi_k(x) dx$ ,  $d_4 = \int_0^L (x+R) \phi_i^{(1)}(x) \phi_k(x) dx$ , and  $d_5 = \int_0^L \phi_i(h) \phi_k(x) D(x-h) dx$ , where  $\phi_i^{(m)}(x) = d^m \phi_i(x)/dx$  represents  $m$ -order derivative of  $x$  in vibration model function.

Equation (17) can be written as follows in the form of a matrix:

$$\mathbf{M} \ddot{\mathbf{q}}(t) + \mathbf{K} \mathbf{q}(t) = \mathbf{F}(t), \quad (18)$$

where  $\mathbf{q}(t)$  is the vector of generalized coordinates  $q_i(t)$  ( $i = 1, 2, \dots, n$ ),  $\mathbf{M} = \rho A L \text{diag}(1, 1, \dots, 1)_{n \times n}$  is a mass matrix,

$\mathbf{K} = \mathbf{K}_e + \mathbf{K}_c + \mathbf{K}_v(\omega)$  is the stiffness matrix of VE-blade and it has complex value and asymmetry, and  $\mathbf{K}_v(\omega)$  has frequency-dependent characteristics.

In the stiffness matrix  $\mathbf{K}$ , the elastic stiffness matrix  $\mathbf{K}_e$ , centrifugal stiffness matrix  $\mathbf{K}_c$ , viscoelastic stiffness matrix  $\mathbf{K}_v(\omega)$ , and its expression are as follows:

$$\begin{aligned} \mathbf{K}_e &= \frac{EI}{L^3} \text{diag}(\lambda_1^4, \lambda_2^4, \dots, \lambda_n^4)_{n \times n}, \\ \mathbf{K}_c &= \frac{1}{2} \rho A \Omega^2 \begin{bmatrix} \int_0^L (x-L)(x+2R+L) \phi_1^{(2)}(x) \phi_1(x) dx & \cdots & \int_0^L (x-L)(x+2R+L) \phi_1^{(2)}(x) \phi_n(x) dx \\ \vdots & \ddots & \vdots \\ \int_0^L (x-L)(x+2R+L) \phi_n^{(2)}(x) \phi_1(x) dx & \cdots & \int_0^L (x-L)(x+2R+L) \phi_n^{(2)}(x) \phi_n(x) dx \end{bmatrix}_{n \times n} \\ &+ \rho A \Omega^2 \begin{bmatrix} \int_0^L (x+R) \phi_1^{(1)}(x) \phi_1(x) dx & \cdots & \int_0^L (x+R) \phi_1^{(1)}(x) \phi_n(x) dx \\ \vdots & \ddots & \vdots \\ \int_0^L (x+R) \phi_n^{(1)}(x) \phi_1(x) dx & \cdots & \int_0^L (x+R) \phi_n^{(1)}(x) \phi_n(x) dx \end{bmatrix}_{n \times n} \\ &- \rho A \Omega^2 L \text{diag}(1, 1, \dots, 1)_{n \times n}, \\ \mathbf{K}_v(\omega) &= \left( \frac{blE_1}{2h(1+i\mu)} (1+i\eta) \right) \text{diag}(\phi_1^2(h), \phi_2^2(h), \dots, \phi_n^2(h))_{n \times n}. \end{aligned} \quad (19)$$

The excitation force vector  $\mathbf{F}(t)$  is

$$\begin{aligned} \mathbf{F}(t) &= F_{a0} \cos(jN\Omega t) \\ &\cdot \left[ \int_0^L \phi_1(x) dx, \int_0^L \phi_2(x) dx, \dots, \int_0^L \phi_n(x) dx \right]^T. \end{aligned} \quad (20)$$

**3.2. Solving the Natural Characteristics.** The solution of the homogeneous equation  $\mathbf{M}\dot{\mathbf{q}}(t) + \mathbf{K}\mathbf{q}(t) = \mathbf{0}$  has exponential

$$\mathbf{q}(t) = \boldsymbol{\psi} e^{i\lambda t}. \quad (21)$$

Substituting it into the homogeneous equation, we have a characteristic equation

$$[\mathbf{K} - \lambda^2 \mathbf{M}] \boldsymbol{\psi} = \mathbf{0} \quad (22a)$$

or

$$\mathbf{K}\boldsymbol{\psi}_k = \lambda_k^2 \mathbf{M}\boldsymbol{\psi}_k, \quad (22b)$$

where  $\lambda_k$  is the  $k$ th eigenvalue and  $\boldsymbol{\psi}_k$  is the eigenvector of the corresponding eigenvalue  $\lambda_k$ ,  $k = 1, \dots, n$ .

Considering that the matrix  $\mathbf{M}$  is symmetric and  $\mathbf{K}$  is asymmetric, the adjoint problem of the eigenequation needs to be solved. The left eigenvector can be obtained through the corresponding adjoint system

$$\mathbf{K}^T \boldsymbol{\psi}_j = \lambda_j^2 \mathbf{M}^T \boldsymbol{\psi}_j, \quad (23)$$

where  $\lambda_j$  is the  $j$ th eigenvalue and  $\boldsymbol{\psi}_j$  is the eigenvector of the corresponding eigenvalue  $\lambda_j$ ,  $j = 1, \dots, n$ .

Premultiply (22b) by  $\boldsymbol{\psi}_j^T$  to get the following equation:

$$\boldsymbol{\psi}_j^T \mathbf{K} \boldsymbol{\psi}_k = \lambda_k^2 \boldsymbol{\psi}_j^T \mathbf{M} \boldsymbol{\psi}_k. \quad (24)$$

After (23) is transposed, then the right side is multiplied by  $\boldsymbol{\psi}_k$ ,

$$\boldsymbol{\psi}_j^T \mathbf{K} \boldsymbol{\psi}_k = \lambda_j^2 \boldsymbol{\psi}_j^T \mathbf{M} \boldsymbol{\psi}_k. \quad (25)$$

By  $\det(\mathbf{M}) = \det(\mathbf{M}^T)$  and  $\det(\mathbf{K}) = \det(\mathbf{K}^T)$ , (22a), (22b), and (23) have the same characteristic value which is  $\det(\mathbf{K} - \lambda_k^2 \mathbf{M}) = \det(\mathbf{K}^T - \lambda_k^2 \mathbf{M}^T)$ ; by (24) minus (25) we have

$$(\lambda_k^2 - \lambda_j^2) \boldsymbol{\psi}_j^T \mathbf{M} \boldsymbol{\psi}_k = 0. \quad (26)$$

If all the eigenvalues are different, when  $k \neq j$ ,  $\lambda_k^2 \neq \lambda_j^2$ . We have

$$\begin{aligned} \boldsymbol{\psi}_j^T \mathbf{M} \boldsymbol{\psi}_k &= 0, \\ \boldsymbol{\psi}_j^T \mathbf{K} \boldsymbol{\psi}_k &= 0 \end{aligned} \quad (27)$$

when  $k = j$ , we have

$$\begin{aligned} \boldsymbol{\psi}_j^T \mathbf{M} \boldsymbol{\psi}_j &= m_j, \\ \boldsymbol{\psi}_j^T \mathbf{K} \boldsymbol{\psi}_j &= k_j, \end{aligned} \quad (28)$$

where  $m_j$  is the modal mass,  $k_j$  is the modal stiffness, and  $j = 1, \dots, n$ .

The relationship between eigenvalues and modal mass and modal stiffness is

$$\lambda_j^2 = \frac{k_j}{m_j}. \quad (29)$$

Eigenvectors  $\psi_j$  and  $\psi_k$  have weighted orthogonality about  $\mathbf{M}$  and  $\mathbf{K}$ ,

$$\psi_j^T \mathbf{M} \psi_k = \begin{cases} 0, & j \neq k, \\ m_j, & j = k, \end{cases} \quad (30a)$$

$$\psi_j^T \mathbf{K} \psi_k = \begin{cases} 0, & j \neq k, \\ k_j, & j = k. \end{cases} \quad (30b)$$

The  $j$  order eigenvalues of complex stiffness system can be written as [31]

$$\lambda_j^2 = \omega_j^2 (1 + i\eta_j), \quad (31)$$

where  $\omega_j$  is the natural frequency and  $\eta_j$  is the modal loss factor of the system.

The natural frequency is

$$\omega_j = \sqrt{\text{Re}(\lambda_j^2)}. \quad (32)$$

The loss factor is

$$\eta_j = \frac{\text{Im}(\lambda_j^2)}{\text{Re}(\lambda_j^2)}. \quad (33)$$

**3.3. Solution of the Frequency Response.** The frequency response of VE-blade can be obtained by transforming (17) in the frequency domain. Equation (18) can be expressed as the equation of motion in the frequency domain through Fourier transform [5].

$$[-\lambda^2 \mathbf{M} + \mathbf{K}(\lambda)] \mathbf{Q}(\lambda) = \mathbf{F}(\lambda), \quad (34)$$

where  $\mathbf{F}(\lambda)$  and  $\mathbf{Q}(\lambda)$  are the Fourier transform result of  $\mathbf{F}(t)$  and  $\mathbf{q}(t)$ .

The VE-blade is subjected to excitation as follows:

$$\mathbf{F}(\lambda) = \mathbf{H}_F(\lambda) e^{i\Phi(\lambda)} = F_{a0} \left[ \int_0^L \phi_1(x) dx, \int_0^L \phi_2(x) dx, \dots, \int_0^L \phi_n(x) dx \right]^T D(\lambda - jN\Omega), \quad (35)$$

where  $\mathbf{H}_F(\lambda)$  are the amplitude of  $\mathbf{F}(\lambda)$  and  $D(\lambda - jN\Omega)$  is Dirac function and meets  $D(x) = \{\infty, x = 0; 0, x \neq 0\}$  and  $\int_{-\infty}^{+\infty} D(x) dx = 1$ .

Displacement response in frequency domain of VE-blade is

$$\mathbf{Q}(\lambda) = \mathbf{H}_q(\lambda) e^{i\Phi(\lambda)}, \quad (36)$$

where  $\mathbf{H}_q(\lambda)$  are the amplitude of  $\mathbf{Q}(\lambda)$ .

Substituting (35) and (36) into (34), we have

$$\mathbf{H}_q(\lambda) = \mathbf{H}(\lambda) \mathbf{H}_F(\lambda). \quad (37)$$

That is,

$$\mathbf{H}(\lambda) = [-\lambda^2 \mathbf{M} + \mathbf{K}(\lambda)]^{-1}, \quad (38)$$

where  $\mathbf{H}(\lambda)$  is frequency response function matrix.

If  $\psi$  is taken as a transformation matrix, we have

$$\mathbf{q}(t) = \psi \mathbf{y}(t), \quad (39)$$

where  $\mathbf{y}(t)$  is modal coordinates vector.

Equation (39) can be expressed as the equation of motion in the frequency domain through Fourier transform, we have

$$\mathbf{Q}(\lambda) = \psi(\lambda) \mathbf{Y}(\lambda). \quad (40)$$

Substitute (39) into (18), and then multiply the left side by  $\psi^T$ . According to the orthogonality of the modal vectors, the equation of forced vibration under modal coordinates is obtained.

$$\text{diag}[m_j] \ddot{\mathbf{y}}(t) + \text{diag}[k_j] \mathbf{y}(t) = \psi^T \mathbf{F}(t), \quad (41)$$

where  $\text{diag}$  is diagonal matrix.

Equation (41) can be expressed as the equation of motion in the frequency domain through Fourier transform; we have

$$\text{diag}[-\lambda^2 m_j + k_j] \mathbf{Y}(\lambda) = \psi^T(\lambda) \mathbf{F}(\lambda). \quad (42)$$

Displacement response in frequency domain of VE-blade is

$$\mathbf{Y}(\lambda) = \mathbf{H}_Y(\lambda) e^{i\Phi(\lambda)}. \quad (43)$$

Substituting (43) into (42), we have

$$\text{diag}[-\lambda^2 m_j + k_j] \mathbf{H}_Y(\lambda) = \psi^T(\lambda) \mathbf{H}_F(\lambda). \quad (44)$$

That is,

$$\mathbf{H}_Y(\lambda) = \text{diag}[-\lambda^2 m_j + k_j]^{-1} \psi^T(\lambda) \mathbf{H}_F(\lambda). \quad (45)$$

Substituting (36) and (43) into (40), the amplitude of frequency response  $\mathbf{H}_q(\lambda)$  is

$$\mathbf{H}_q(\lambda) = \psi(\lambda) \text{diag}[-\lambda^2 m_j + k_j]^{-1} \psi^T(\lambda) \mathbf{H}_F(\lambda). \quad (46)$$

The frequency domain response amplitude of the  $oxyz$  coordinate system is the superposition of the frequency response amplitude in the generalized coordinates, so we have

$$H(x_0) = \phi(x_0) \mathbf{H}_q(\lambda) = \sum_{i=1}^n \phi_i(x_0) H_{qi}(\lambda), \quad (47)$$

where  $x_0$  is the height between the place picking up response and the origin  $o$  and  $h \leq x_0 \leq L$ , at the blade root  $x_0 = h$ , at the top of blade  $x_0 = L$ . According to (14),  $\phi(x_0) = [\phi_1(x_0), \phi_2(x_0), \dots, \phi_n(x_0)]^T$  is the vector of modal shape function at  $x_0$ .

TABLE 1: Material parameters of the viscoelastic damping block.

Material	Elasticity modulus/Pa	Poisson's ratio	Density/(kg/m <sup>3</sup> )	Loss factor
Zn-33	$1 \times 10^9$	0.498	930	0.9683

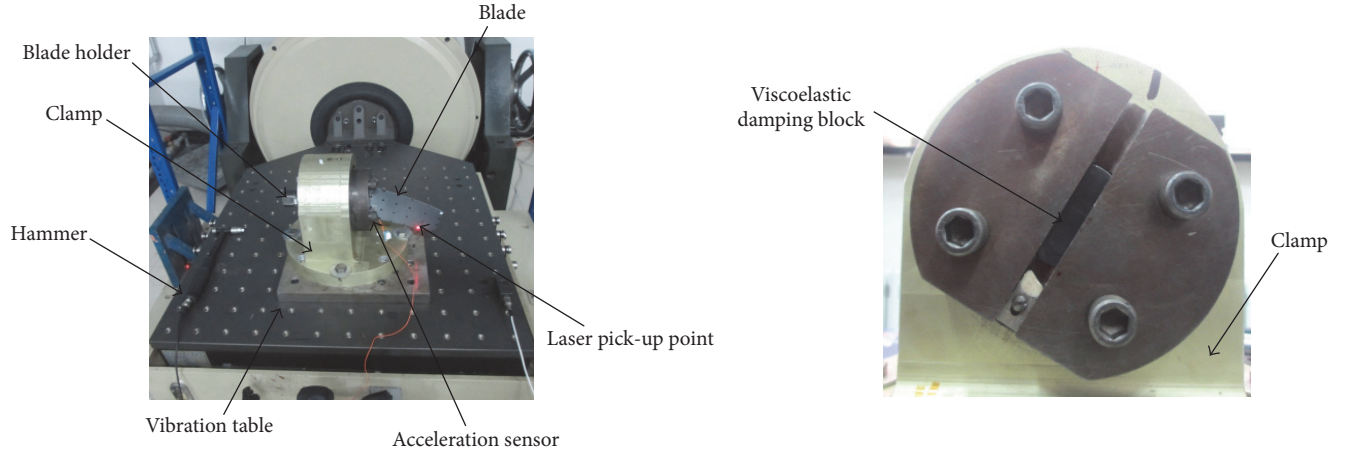


FIGURE 4: Test device of VE-blade.

TABLE 2: Geometric parameters of viscoelastic material Zn-33/mm.

Length $l$	Width $b$	Thickness $h$
45.60	11.30	1.48

#### 4. Numerical Results and Discussion

The effect of viscoelastic damping block on natural frequency and modal damping ratio of the blade is studied. The parameters of viscoelastic damping block mainly include thickness, energy storage modulus, and loss factor. Meanwhile, consider the influence of rotational angular velocity on the natural characteristics of VE-blade.

The number of preset blade stators  $N = 36$ , the resonant frequency  $j = 1$ , the radius of the disc are a multiple of the length of the blade,  $R = 1.2L$ .

In order to compare with the static state experimental data, the rotational speed is 0; when considering the effect of rotational angular velocity on the natural frequency and modal damping ratio of the VE-blade, the speed range is 0~60000 rpm.

When the blade is simplified, only the first three-order modes ( $n = 3$ ) are truncated. In (18), the dimension of the  $M$  and  $K$  matrices is 3.

**4.1. Material and Geometric Parameters of VE-Blade.** In the analysis, elastic modulus of viscoelastic damping block is constant. Material parameters and the geometry size of viscoelastic damping block are shown in Tables 1 and 2.

The material and geometric parameters of the blade are confirmed by the measured method and the material parameters of the blade are shown in Table 3.

The 30 N·m torque is applied to the blade holder; fix the rubber block made by ZN-33 on the blade clamp slot and blade root. Vibration table is used to sweep the blade and

VE-blade to get the natural frequencies, then the blade is excited by constant frequency to get the resonance response. Envelope method is used to obtain the modal damping ratio of a certain vibration frequency, using a laser vibrometer pickup blade response data. The test device is shown in Figure 4.

Theoretical analysis in this chapter mainly considers material damping effect on the natural frequency and response of the blade after adding viscoelastic damping block. Obtain the blade damping ratio by Rayleigh method using the experimental data before adding viscoelastic damping block. Material damping is used to represent the blade damping after adding viscoelastic damping block. The experimental data is shown in Table 4.

A cantilever VE-blade is simplified according to the testing the first three natural frequency of the real blade to obtain geometric parameters of cantilever beam. Calculating formula of natural frequency of cantilever beam is used.

$$\omega_i = \frac{\lambda_i^2}{L_o^2} \sqrt{\frac{EI}{\rho A}} = \frac{\lambda_i^2 H}{L_o^2} \sqrt{\frac{E}{12\rho}}, \quad (48)$$

where  $\omega_i$  is natural frequency of testing blade.

The length of the viscoelastic damping layer is used as the width of the cantilever beam; that is,  $B = l = 45.6$  mm. Then the length of cantilever beam is measured blade height; that is, 130 mm, and then the thickness  $H$  of the cantilever beam is obtained. The geometrical parameters of the first three-order cantilever beam are shown in Table 5.

**4.2. Resonance Characteristics.** The natural properties of the VE-blade are calculated and compared with the test data. Using aerodynamic load simulates excitation energy and changes the excitation energy from 0.5 g to 3 g, to calculate the resonance characteristics of the blade with one-layer

TABLE 3: Material parameters of the blade.

Material	Elasticity modulus/Pa	Poisson's ratio	Density/(kg/m <sup>3</sup> )	Loss factor
1Cr11Ni2W2MoV	$214 \times 10^9$	0.3	7800	—

TABLE 4: Natural frequencies and modal damping ratio of the blade.

Order	Mode shape	Natural frequency/Hz	Damping ratio/%
(1)	First bending	253.25	0.0954
(2)	First bending	1011.75	0.0818
(3)	First torsion	1189.50	0.0242

TABLE 5: Geometric parameters of the blade are simplified as cantilever beam/mm.

Order	Length $L_0$	Width $B$	Thickness $H$
(1)	130	45.6	5.07
(2)	130	45.6	3.22
(3)	130	45.6	1.35

viscoelastic damping block. Remove the viscoelastic force term in (14), so that the thickness of viscoelastic damping block  $h = 0$ ; we can get the resonance curve of the pure blade.

The frequency domain response of the VE-blade and the blade tip in stationary state are shown in Figure 5.

In this study, all excitation forces are assumed to be uniform with 0.5 g.

As can be seen from Figure 5, the added viscoelastic block shifts the first three-order resonance frequency of the blade from 253 Hz to 247.34 Hz, 1012.15 Hz to 989.57 Hz, and 1189.25 Hz to 1163.8 Hz, respectively. The natural frequency decreases by 2.25%, 2.23%, and 2.14%, respectively. The first three-order vibration amplitude at the tip of the VE-blade compared with the pure blade decreases from 0.3382 mm to 0.2256 mm, 0.0106 mm to 0.0103 mm, and 0.0053 mm to 0.0017 mm, respectively. The vibration amplitude decreased by 33.29%, 2.83%, and 67.92%, and the damping effect is obvious. The experimental test data are shown in Table 6, in which the first three-order amplitude decreased by 13.36%, 21.9%, and 11.8%. The experimental value and the simulation value trend were basically consistent, which verified the rationality of the numerical simulation.

**4.3. Response Characteristics.** For the pure blade with viscoelastic damping block, its thickness is one layer, two layers, three layers, respectively. Experimental results and simulation result of the first three-order resonant amplitude at the tip of VE-blade for the above three cases are shown in Figure 6. In this study, all excitation forces are assumed to be uniform with 0.5 g to consider the effect of different layers of viscoelastic damping block on the response characteristic of the blade.

As can be seen from Figure 6, for the pure blade with viscoelastic damping block, its thickness is one layer, two layers, and three layers, respectively. The simulated and experimental values of the first three-order resonant amplitude at the tip of the blade for the above three cases are shown in Figure 6.

In Figure 6(a), the deviation of simulation results and experiment results with above three cases are 28.5%, 17.6%, and 63.9%, respectively. With the resonance response of blade with one and two layers' viscoelastic damping block lower than the pure blade, we can see from the experiment result that the resonance response fell by 13.36%, and 16.87% compared with the pure blade. But the three layers of viscoelastic damping block is applied to the blade, the resonance response decreases by 3.1% in simulation result and increased in experiment result.

As can be seen from Figure 6(b), the deviation of simulation result and experiment result with above three cases are 53.25%, 52.9%, and 26.8%. The resonance response of blade with two layers viscoelastic damping block is increased by 2.3% than the pure blade in experiment result and lower in simulation result. While the resonance response of blade with one and three layers viscoelastic damping block decreased by 36.9%, 39.6% in simulation result and decreased by 21.9%, 38.5% in experiment result. The damping effect is obvious.

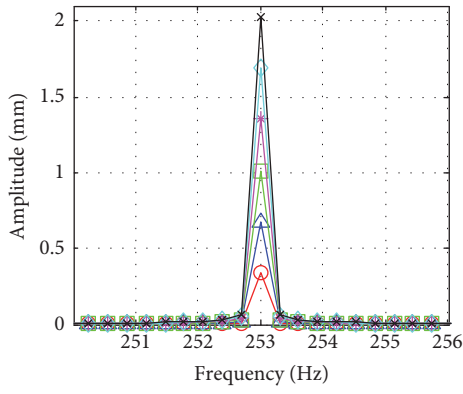
As can be seen from Figure 6(c), the deviation of simulation result and experiment result with above three cases are 96.9%, 95.5%, and 97.9%. The resonance response of blade with above three cases decreased by 83.1%, 72.3%, and 86.9% compared with the pure blade in simulation result, the damping effect is obvious. In experiment result, the resonance response of blade with one and two layers viscoelastic damping block decreased by 11.8% and 4.3%, increased by 2.0% after applied three layers viscoelastic damping block.

Therefore, the results show that the calculated results are smaller than the experimental results, but they have the same trend. Possible reasons are using gas excitation to simulate the base excitation so that the actual exciting force is insufficient. Blade model is simplified according to the natural frequency, without considering the change of loss factor, thus leading to vibration amplitude error exists.

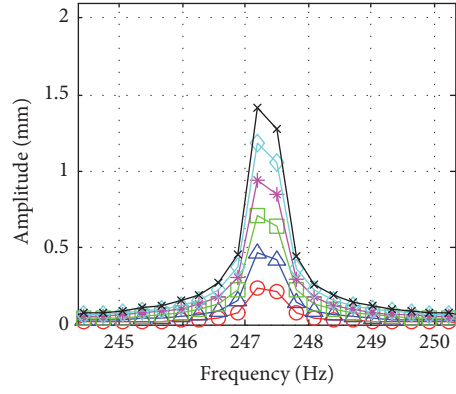
**4.4. Effect of Viscoelastic Damping Parameters on Natural Characteristics.** Consider the effect of the viscoelastic damping block's thickness, storage modulus, loss factor, and rotational angular velocity on the natural frequency and modal damping ratio of the VE-blade.

**4.4.1. Effect of Viscoelastic Damping Block's Thickness.** Change the viscoelastic damping block's thickness from 1 mm to 6 mm, the natural frequency, and modal damping ratio of the VE-blades shown in Table 7. Figure 7 shows the influence of the thickness change on the natural frequency and modal damping ratio of viscoelastic damping block-blade.

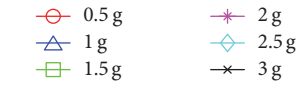
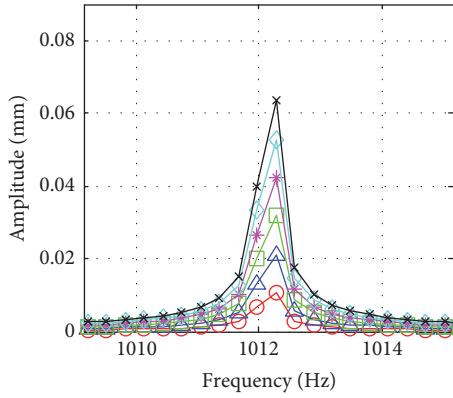
As can be seen from Table 7 and Figure 7, with the increase of the thickness of the viscoelastic damping block, the natural frequency of the VE-blade is slowly decreasing, and the modal damping ratio is gradually increasing. The thickness of viscoelastic damping block is 1 mm and 2 mm as



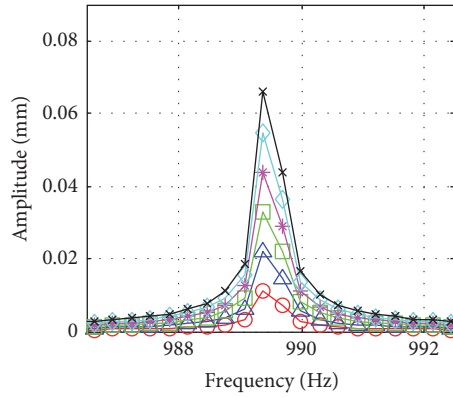
(a) The first-order amplitude of pure blade



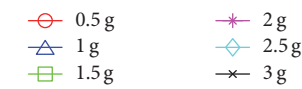
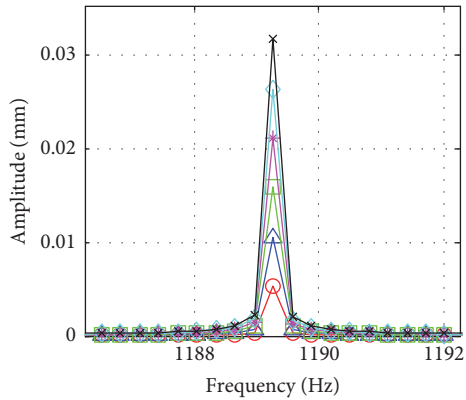
(b) The first-order amplitude of VE-blade



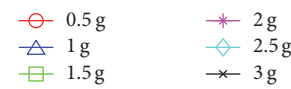
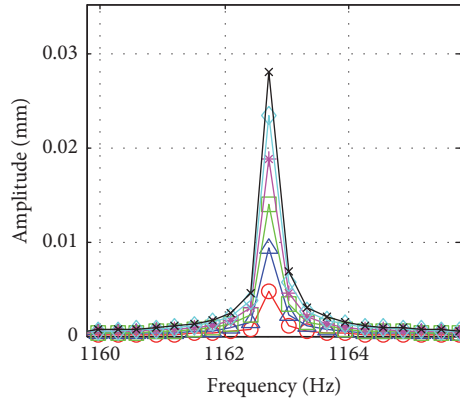
(c) The second-order amplitude of pure blade



(d) The second-order amplitude of VE-blade



(e) The third-order amplitude of pure blade



(f) The third-order amplitude of VE-blade

FIGURE 5: Comparison of numerical results of resonance characteristics of the VE-blade and pure blade.

TABLE 6: Resonant amplitude obtained by test/mm.

Order	Excitation energy	Response point	Pure blade/mm	VE-blade/mm
(1)	0.5 g	Blade tip	0.3645	0.3158
(2)	1 g	Blade tip	0.0283	0.0221
(3)	1 g	Blade tip	0.0669	0.0590

TABLE 7: Natural frequencies and modal damping ratios of the blade with different thickness of viscoelastic damping block.

Thickness/mm	First order		Second order		Third order	
	Natural frequency/Hz	Modal damping ratio/%	Natural frequency/Hz	Modal damping ratio/%	Natural frequency/Hz	Modal damping ratio/%
1	249.15	$6.05e-04$	996.78	$2.28e-03$	1171.5	$3.04e-02$
2	245.39	$4.77e-03$	981.89	$1.77e-02$	1156.2	$2.31e-01$
3	241.75	$1.59e-02$	967.58	$5.78e-02$	1144.9	$7.35e-01$
4	238.21	$3.70e-02$	952.80	$1.33e-01$	1138.6	1.63
5	234.78	$7.12e-02$	941.00	$2.50e-01$	1137.9	2.94
6	231.46	$1.21e-01$	928.82	$4.17e-01$	1143.1	4.66

TABLE 8: Natural frequencies and modal damping ratios of the blade with different storage modulus.

Storage modulus/Mpa	First order		Second order		Third order	
	Natural frequency/Hz	Modal damping ratio/%	Natural frequency/Hz	Modal damping ratio/%	Natural frequency/Hz	Modal damping ratio/%
500	247.34	$9.73e-10$	989.49	$3.65e-09$	1162.6	$4.82e-08$
700	241.86	$1.35e-09$	967.59	$5.05e-09$	1136.9	$6.68e-08$
1000	236.56	$1.90e-09$	946.40	$7.14e-09$	1112.0	$9.44e-08$
2000	231.44	$3.77e-09$	925.90	$1.41e-08$	1087.9	$1.87e-07$
3000	226.48	$5.59e-09$	906.06	$2.09e-08$	1064.6	$2.77e-07$
4000	221.68	$7.38e-09$	886.85	$2.77e-08$	1042.0	$3.66e-07$

an example. The natural frequency decreases from 249.15 Hz down to 245.39 Hz, decreased by 1.5%, modal damping ratio increased from  $6.05e-04\%$  to  $4.77e-03\%$ , increased by 87.3%. Increasing the thickness of the viscoelastic damping block to improve the damping effect of the system is obvious.

**4.4.2. Effect of Viscoelastic Damping Block's Storage Modulus.** Change the storage modulus from 500 MPa to 4000 MPa; the effect on natural frequency and modal damping ratio is shown in Table 8 and Figure 8.

As can be seen from Table 8 and Figure 8, with the increase of the storage modulus of the viscoelastic damping block, the natural frequency of the VE-blade is decreasing, and the modal damping ratio is gradually increasing. Change the viscoelastic damping block's storage modulus from 500 MPa to 700 MPa, the natural frequency decreased from 247.34 Hz down to 241.86 Hz, decreased by 2.2%, and modal damping ratio increased from  $9.73e-10\%$  to  $1.35e-9\%$  increased by 27.9%. It shows that selecting the damping material with large storage modulus is beneficial to improve the damping of the structure.

**4.4.3. Effect of Viscoelastic Damping Block's Loss Factor.** Change the loss factor from 0.5 to 1.5; the effect on natural

frequency and modal damping ratio is shown in Table 9 and Figure 9.

As can be seen from Table 9 and Figure 9, with the increase of the loss factor of the viscoelastic damping block, the natural frequency of the VE-blade is decreasing, and the modal damping ratio is significantly increasing, especially in the third order. It is showed that the damping material with large loss factor is directly beneficial to improve the damping of the structure.

Change the viscoelastic damping block's loss factor from 0.5 to 0.7, the natural frequency decreased from 247.34 Hz down to 241.87 Hz, decreased by 2.2%, and modal damping ratio increased from  $1.01e-3\%$  to  $1.39e-3\%$ , increased by 27.3%.

**4.4.4. Effect of the Rotational Speed.** Change the rotational speed from 0 rpm to 60000 rpm, the dynamic frequency and modal damping ratio of the VE-blade are shown in Table 10 and the Campbell diagram of the viscoelastic damping block-blade is shown in Figure 10.

As can be seen from the Table 10, with the increase of rotational speed, the natural frequency of the VE-blade gradually increased, and the modal damping ratio decreased gradually.

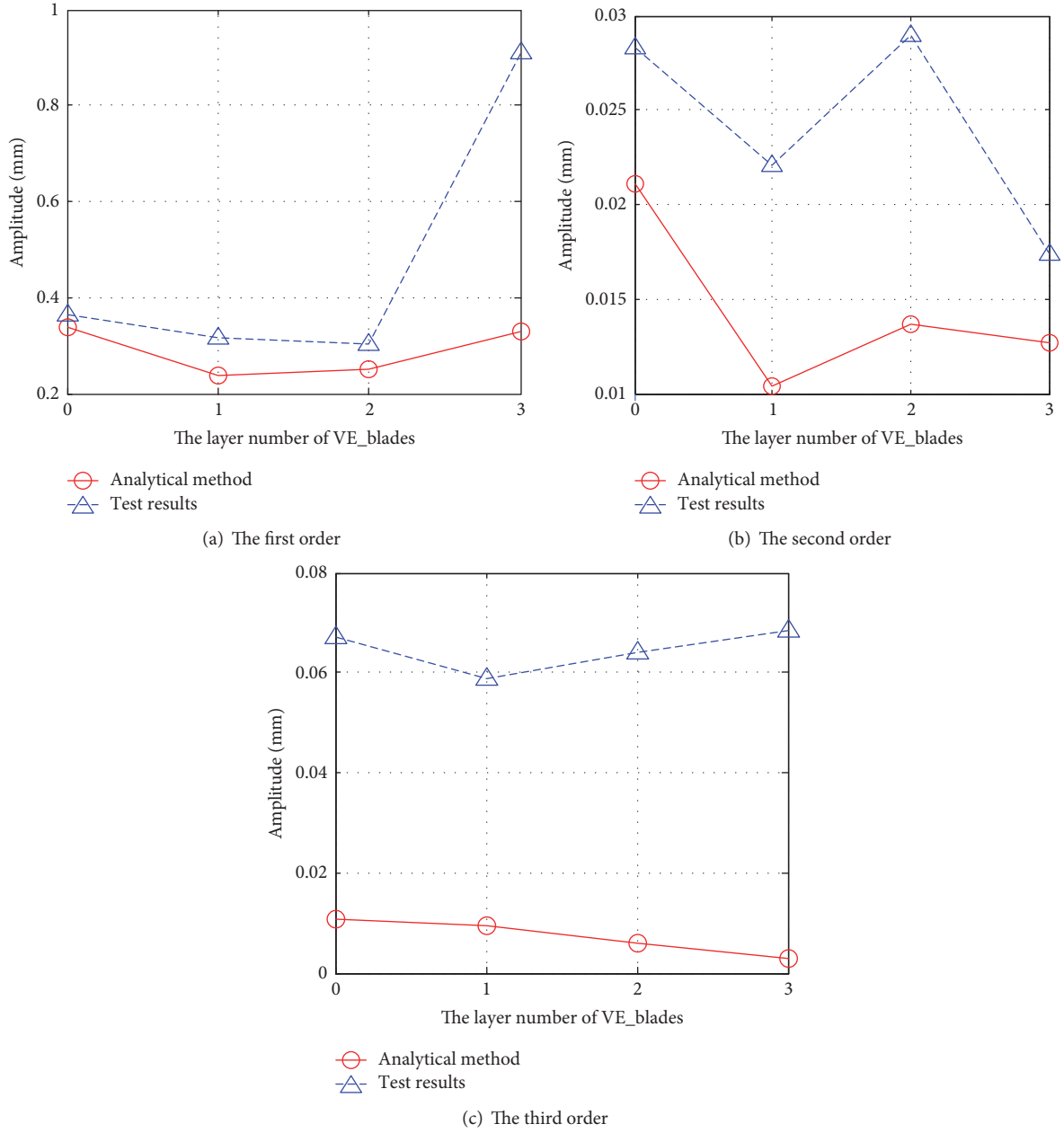


FIGURE 6: Comparison of experimental results (solid line with circle) and simulation results (dotted line with triangle) of resonant response of VE-blade.

TABLE 9: Natural frequencies and modal damping ratios of the blade with different loss factors.

Loss factor	First order		Second order		Third order	
	Natural frequency/Hz	Modal damping ratio/%	Natural frequency/Hz	Modal damping ratio/%	Natural frequency/Hz	Modal damping ratio/%
0.5	247.34	$1.01e-3$	989.57	$3.77e-3$	1163.8	$4.97e-2$
0.7	241.87	$1.39e-3$	967.66	$5.21e-3$	1138	$6.88e-2$
0.9	236.57	$1.77e-3$	946.47	$6.63e-3$	1113.1	$8.76e-2$
1.1	231.45	$2.14e-3$	925.97	$8.02e-3$	1089	$1.06e-1$
1.3	226.49	$2.50e-3$	906.13	$9.38e-3$	1065.6	$1.24e-1$
1.5	221.68	$2.86e-3$	886.92	$1.07e-2$	1043	$1.42e-1$

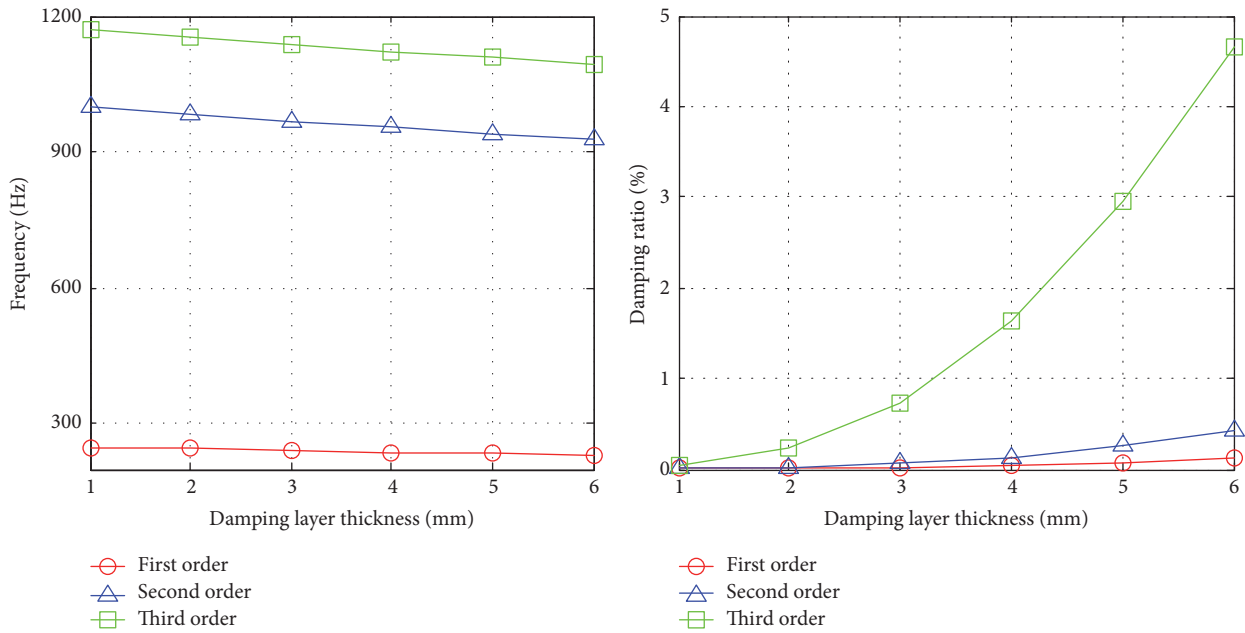


FIGURE 7: The thicknesses of viscoelastic damping block on the influence of natural frequencies and modal damping ratio of the blade.

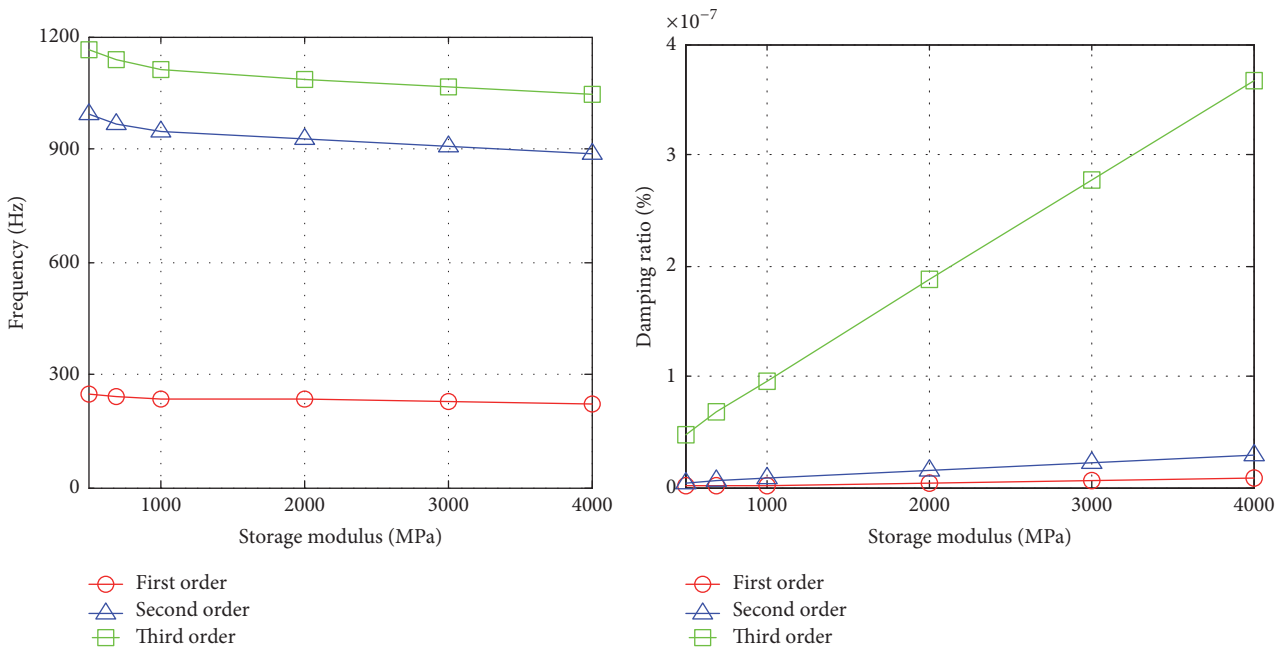


FIGURE 8: Natural frequencies and modal damping ratio of the blade under the influence of storage modulus.

Change the rotational speed from 10000 rpm to 20000 rpm, the natural frequency increased from 247.34 Hz to 377.15 Hz and increased by 34.4%; modal damping ratio decreased from  $2.56e - 2\%$  to  $1.06e - 2\%$ , and decreased by 58.6%. It shows that the damping effect of the viscoelastic damping block decreased with the increase of the rotational speed.

From Figure 10, when the VE-blade is working at about 10000 rpm, the second-order frequency curve and excitation

vibration frequency line  $k = 7$  intersect, prone to resonance; when the VE-blade working speed range in 10000~20000 rpm, the first-order frequency curve and excitation vibration frequency line  $k = 2$  intersect, prone to resonance; when the VE-blade working speed range in 40000~50000 rpm, the third-order frequency curve and excitation vibration frequency line  $k = 7$  intersect, but its not within the working speed range; therefore it will not cause resonance.

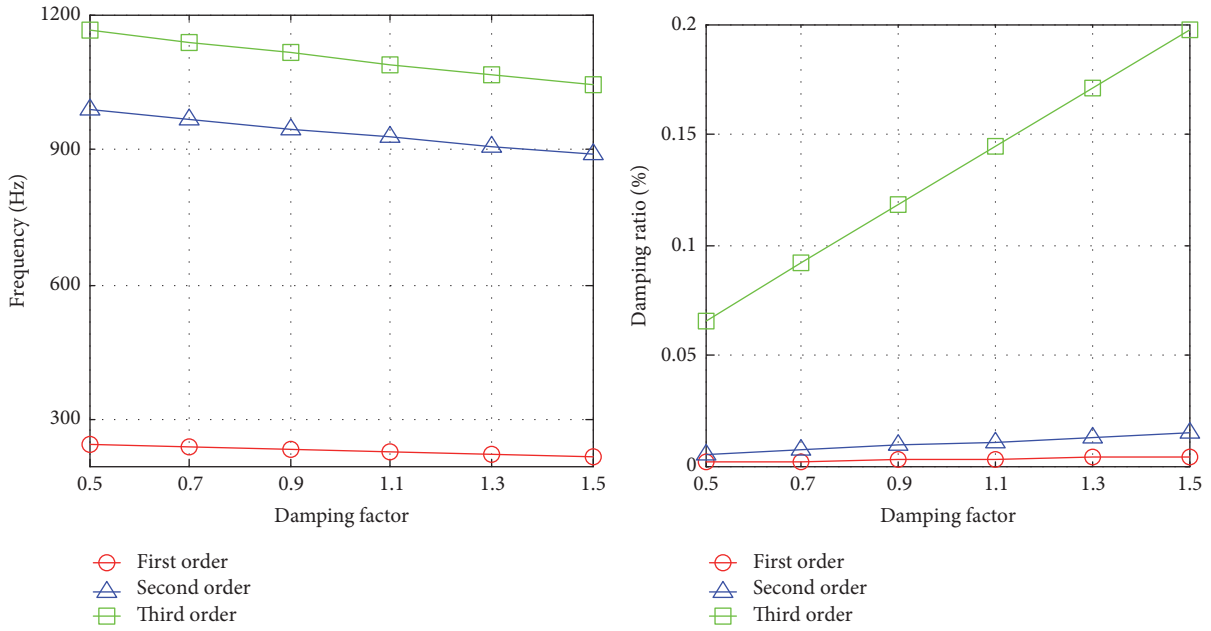


FIGURE 9: Natural frequencies and modal damping ratio of the blade under the influence of loss factor.

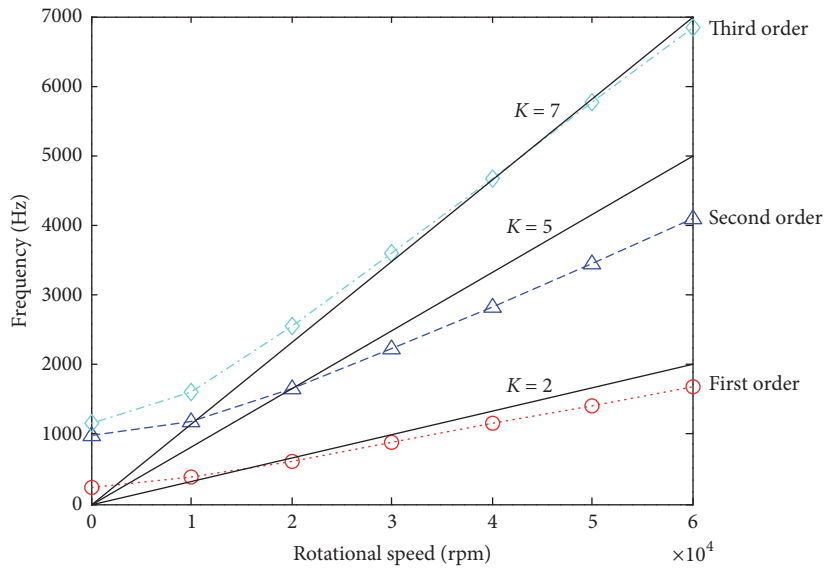


FIGURE 10: Campbell diagram of the blade with viscoelastic damping block.

TABLE 10: Dynamic frequencies and modal damping ratios of the blade with different rotating speeds.

Rotational speed/rpm	First order		Second order		Third order	
	Natural frequency/Hz	Modal damping ratio/%	Natural frequency/Hz	Modal damping ratio/%	Natural frequency /Hz	Modal damping ratio/%
0	247.34	$2.56e-2$	989.5	$9.58e-2$	1162.8	1.26
10000	377.15	$1.06e-2$	1182.5	$6.42e-2$	1614.2	$6.28e-2$
20000	619.86	$4.01e-3$	1652.1	$3.16e-2$	2542.2	$2.41e-1$
30000	882.34	$2.09e-3$	2224.8	$1.68e-2$	3587.6	$1.16e-1$
40000	1149.3	$1.30e-3$	2835.5	$9.97e-3$	4666.7	$6.57e-2$
50000	1417.3	$8.82e-4$	3462.0	$6.45e-3$	5756.4	$4.13e-2$
60000	1685.3	$6.31e-4$	4095.1	$4.44e-3$	6848.2	$2.80e-2$

## 5. Conclusions

Based on analytical analysis, numerical calculation, and test, the dynamic characteristic of the VE-blade is studied. The effects of various parameters including thickness, storage modulus, loss factor of viscoelastic damping block, and rotational speed on natural frequency and modal damping ratio of VE-blade are discussed in detail. Conclusions are as follows.

The VE-blade is simplified as a cantilever beam. Based on Euler Bernoulli beam theory, under the assumption of microvibration, moment of inertia and the nonlinearity of the strain and displacement are neglected. Compared with the experimental data, the rationality of the cantilever beam model and the mechanical simplification method is verified.

The first three-order natural frequencies of the blade decrease after applied a layer viscoelastic damping block. The first three-order natural frequencies decreased by 2.25%, 2.23%, 2.14%, respectively. Test results were reduced by 0.49%, 0.52%, and 0.15%, respectively. The experimental and simulation results show a trend consistency.

With the increase of viscoelastic damping block thickness, the influence on different orders resonant response is different. The resonant response decreased by 33.3%, 26.2%, and 3% in simulation result. In experiment result, it decreased by 13.36% and 16.87% and increased after applying three layers' viscoelastic damping block. The experiment and simulation result have the same trend after applying one and two layers viscoelastic damping block, which verified the rationality of the simulation result.

With the increase of the thickness of viscoelastic damping block, the storage modulus, loss factor, the natural frequency of VE-blade decreases and modal damping ratio increases. It is suggested that the appropriate increase of the thickness of the viscoelastic damping block, the selection of the material with larger energy storage modulus, and loss factor can improve the modal damping ratio of the system and obtain a better effect of vibration reduction.

With the increase of the rotational speed, the natural frequency of the VE-blade increases gradually, and the modal damping ratio decreases obviously, which shows that the damping effect of the viscoelastic damping block decreases with the increase of the rotational speed.

## Conflicts of Interest

The authors declare that they have no conflicts of interest.

## Acknowledgments

This work is financially supported by National Natural Science Foundation of China (no. 11502227) and Shandong Provincial Natural Science Foundation, China (no. ZR2014EEP006).

## References

- [1] X. Q. Zhou, D. Y. Yu, X. Y. Shao, S. Q. Zhang, and S. Wang, "Research and applications of viscoelastic vibration damping materials: A review," *Composite Structures*, vol. 136, pp. 460–480, 2016.

- [2] P. C. O. Martins, T. A. M. Guimarães, D. D. A. Pereira, F. D. Marques, and D. A. Rade, "Numerical and experimental investigation of aeroviscoelastic systems," *Mechanical Systems and Signal Processing*, vol. 85, pp. 680–697, 2017.
- [3] G. J. Chang, *Viscoelastic damping materials*, National Defense Industry Press, Beijing, China, 2012.
- [4] E. Balme, M. Corus, S. Baumhauer, P. Jean, and J. Lombard, "Constrained viscoelastic damping, test/analysis correlation on an aircraft engine," in *Structural Dynamics, Volume 3*, Conference Proceedings of the Society for Experimental Mechanics Series, pp. 1177–1185, Springer New York, New York, NY, 2011.
- [5] C. A. Bavastri, E. M. D. S. Ferreira, J. J. De Espíndola, and E. M. D. O. Lopes, "Modeling of dynamic rotors with flexible bearings due to the use of viscoelastic materials," *Journal of the Brazilian Society of Mechanical Sciences and Engineering*, vol. 30, no. 1, pp. 22–29, 2008.
- [6] S. Ghinet and N. Atalla, "Modeling thick composite laminate and sandwich structures with linear viscoelastic damping," *Computers & Structures*, vol. 89, no. 15–16, pp. 1547–1561, 2011.
- [7] S. W. Park, "Analytical modeling of viscoelastic dampers for structural and vibration control," *International Journal of Solids and Structures*, vol. 38, no. 44–45, pp. 8065–8092, 2001.
- [8] J. B. Deng, Z. G. Zhu, and Q. H. Li, "Damping Characteristics of metal rubber damper on root of cantilever beam," *Journal of Aerospace Power*, vol. 13, no. 4, pp. 425–427, 1998.
- [9] H. X. Li, Z. J. Huang, and L. Zhang, "New technique for elimination fault of the tenon of fan blade with mid-span shroud," *Aeroengine*, vol. no.2, pp. 27–31, 2002.
- [10] R. T. Miao, "An analysis on break failure at dovetail of the 4th stage compressor blades of an engine," *Gas Turbine Experiment and Research*, vol. 16, no. 2, pp. 34–37, 2003.
- [11] T. Kocatürk, "Determination of the steady-state response of viscoelastically supported cantilever beam under sinusoidal base excitation," *Journal of Sound and Vibration*, vol. 281, no. 3–5, pp. 1145–1156, 2005.
- [12] Y. Wang and D. J. Inman, "Finite element analysis and experimental study on dynamic properties of a composite beam with viscoelastic damping," *Journal of Sound and Vibration*, vol. 332, no. 23, pp. 6177–6191, 2013.
- [13] M. Rafiee, F. Nitzsche, and M. Labrosse, "Dynamics, vibration and control of rotating composite beams and blades: A critical review," *Thin-Walled Structures*, vol. 119, pp. 795–819, 2017.
- [14] S. Kumar and R. Kumar, "Theoretical and experimental vibration analysis of rotating beams with combined ACLD and Stressed Layer Damping treatment," *Applied Acoustics*, vol. 74, no. 5, pp. 675–693, 2013.
- [15] D. Biswas and M. C. Ray, "Active constrained layer damping of geometrically nonlinear vibration of rotating composite beams using 1-3 piezoelectric composite," *International Journal of Mechanics and Materials in Design*, vol. 9, no. 1, pp. 83–104, 2013.
- [16] J. Austruy, F. Gandhi, and N. Lieven, "Rotor vibration reduction using an embedded spanwise absorber," *Journal of the American Helicopter Society*, vol. 57, no. 2, Article ID 022008, 2012.
- [17] S. M. Hosseini, H. Kalhori, A. Shooshtari, and S. N. Mahmoodi, "Analytical solution for nonlinear forced response of a viscoelastic piezoelectric cantilever beam resting on a nonlinear elastic foundation to an external harmonic excitation," *Composites Part B: Engineering*, vol. 67, pp. 464–471, 2014.

- [18] J. B. Min, K. P. Duffy, B. B. Choi, A. J. Provenza, and N. Kray, "Numerical modeling methodology and experimental study for piezoelectric vibration damping control of rotating composite fan blades," *Computers & Structures*, vol. 128, pp. 230–242, 2013.
- [19] M. Kumar, R. A. Shenoi, and S. J. Cox, "Experimental validation of modal strain energies based damage identification method for a composite sandwich beam," *Composites Science and Technology*, vol. 69, no. 10, pp. 1635–1643, 2009.
- [20] V. S. Rao, B. V. Sankar, and C. T. Sun, "Constrained Layer Damping of Initially Stressed Composite Beams Using Finite Elements," *Journal of Composite Materials*, vol. 26, no. 12, pp. 1752–1766, 1992.
- [21] R. Rikards, A. Chate, and E. Barkanov, "Finite element analysis of damping the vibrations of laminated composites," *Computers & Structures*, vol. 47, no. 6, pp. 1005–1015, 1993.
- [22] S. S. A. Ravi, T. K. Kundra, and B. C. Nakra, "Response re-analysis of damped beams using eigenparameter perturbation," *Journal of Sound and Vibration*, vol. 179, no. 3, pp. 399–412, 1995.
- [23] Y. M. Chen and H. R. Shi, "Vibration analysis of beams with partial constrained layer damping treatment," *Machinery Design and Manufacture*, vol. 5, pp. 103–105, 2009.
- [24] M. Wang, H. R. Chen, R. X. Bai, and Y. H. Cai, "Dynamic characteristics of composite reinforced laminates attached with frequency-dependent damping layers," *Engineering mechanics*, vol. 24, no. 10, pp. 64–70, 2007.
- [25] S. H. Zhang and H. L. Chen, "A study on the damping characteristics of laminated composites with integral viscoelastic layers," *Composite Structures*, vol. 74, no. 1, pp. 63–69, 2006.
- [26] F. Cortés and M. J. Elejabarrieta, "An approximate numerical method for the complex eigenproblem in systems characterised by a structural damping matrix," *Journal of Sound and Vibration*, vol. 296, no. 1-2, pp. 166–182, 2006.
- [27] D. H. Liu, *Application of viscoelastic damping vibration and noise reduction*, Aerospace Publishing House, Beijing, China, 1990.
- [28] A. D. Nashif, D. I. G Jones, and J. P. Henderson, *Vibration Damping*, John Wiley & Sons, Inc, New York, NY, USA, 1985.
- [29] Y. Cui, *Dynamic research of rigid-flexibly coupling system in stream turbine blades*, Harbin Engineering University, Harbin, China, 2008.
- [30] M. O. Kaya, "Free vibration analysis of a rotating Timoshenko beam by differential transform method," *Aircraft Engineering and Aerospace Technology*, vol. 78, no. 3, pp. 194–203, 2006.
- [31] D. J. Ewins, *Modal testing: theory and practice*, Research studies press, England, UK, 1984.

## Research Article

# Experimental Validation of Numerical Model for Bi-Tilt-Isolator

Ming-Hsiang Shih <sup>1</sup>, Wen-Pei Sung <sup>2</sup>, and Chia-Yu Ho<sup>1</sup>

<sup>1</sup>Department of Civil Engineering, National Chi Nan University, Nantou 545, Taiwan

<sup>2</sup>Department of Landscape Architecture, Integrated Research Center for Green Living Technologies, National Chin-Yi University of Technology, Taichung 41170, Taiwan

Correspondence should be addressed to Wen-Pei Sung; [wps@ncut.edu.tw](mailto:wps@ncut.edu.tw)

Received 8 September 2017; Accepted 7 February 2018; Published 14 March 2018

Academic Editor: Paulo B. Gonçalves

Copyright © 2018 Ming-Hsiang Shih et al. This is an open access article distributed under the Creative Commons Attribution License, which permits unrestricted use, distribution, and reproduction in any medium, provided the original work is properly cited.

Bi-Tilt Isolator (BTI) is composed of bi-tilt beveled substrate and slider. The advantages of BTI are that the maximum upload seismic force of structure can be easily controlled and displacement of isolation layer will be reduced. Sliding force, friction force, and impulse force are caused in the slanting process of BTI, nonlinear behavior. A nonlinear mathematical model is derived based on the sliding upwards, sliding downwards, and transition stages. Then, BTI element of nonlinear analysis program, GENDYN, is developed by the fourth-order Runge-Kutta method, the discretized ordinary differential equation for three movement stages of BTI. Then, test set-up of superstructure installed with BTI is tested and recorded the real displacement and acceleration responses under conditions of full lubrication, mild lubrication, and without lubrication between interface of bi-tilt beveled substrate and slider with three various initial displacements. The comparison of simulation results and test results shows the following: (1) root mean square error is below 1.35% for WD40 sprayed, 0.47% for WD40 whipped, and 0.54% for without lubrication, respectively; (2) the maximum root mean square error for simulating with cubic polynomial function of friction is much less than those of constant friction except conditions of full lubrication, which are not affected by kinetic friction force; (3) application of cubic polynomial function for simulating friction of BTI with three different lubricated conditions can perform very fine simulation results, compared with the test results. This proposed mathematical model and BTI element of GENDYN program, using cubic polynomial function of friction, perform fine simulation capability to assess nonlinear isolation effect of structure installed with BTI.

## 1. Introduction

Earthquakes and strong winds are unavoidable natural disasters on the planet. Recently, the intensity of natural disasters has been enhanced according to many factors; strong earthquakes, such as 9.0 magnitude (Richter scale) earthquakes, happened on 2004 in India and 2011 in Japan and triggered severe tsunami, resulting in heavy losses of life and property. In addition, some strong earthquakes occurred in the world. For example, 7.7 magnitude (Richter scale) earthquake in Pakistan on 2013 and 7.8 and 7.3 magnitude (Richter scale) earthquakes in Nepal on 2015 caused a lot of casualties. Taiwan is located in the Circum-Pacific Seismic Zone and also at the junction of the Eurasian plate and the Philippine Sea plate, witnessing sensible earthquakes every year. In particular, Chi-Chi earthquake (7.3 magnitude on the Richter scale) happened on 1999 to result in great damage to

buildings and bridges. Moreover, a 6.4 magnitude (Richter scale) earthquake happened in southern Taiwan and led to the 16-story building collapsing on the ground, causing heavy casualties in 2016, before Chinese New Year. The main reason for building collapse is the lack of earthquake resistance capability.

To maintain the safety of buildings to resist seismic force and external force, structural control theorems and equipment are widely applied in Architecture and Civil Engineering. Structural control techniques [1–3] have been divided into passive control (isolation, shock absorption, and energy dissipation) [4–11], active control [12–23], and semiactive control [24–27]. In this study, a newly developed Bi-Tilt Isolator is proposed as an isolation system for building. Traditionally, soft isolation layer is used as base isolation, for example, lead rubber bearing, LRB [28–33], and rubber bearing, RB [34, 35]. The purposes of LRB and RB are applied

to extent structural period and isolate seismic waves into the structures to reduce the horizontal seismic force. The defect of these kinds of isolation systems is a large displacement of isolation layer, affecting the practicality.

To improve shortcomings of base isolation system, Bi-Tilt Isolator, BTI, composed of bi-tilt beveled substrate and slider, as shown in Figure 1, is proposed in this study. Although the proposed BTI and Friction Pendulum System (FPS) look quite similar, isolation efficiency and practical performance between these two devices have significant differences.

FPS is composed of a concave plate with spherical surface and an articulated slider with the same radius of curvature as the substrate [36–38]. These two devices provide functions of autohoming and frictional energy dissipation mechanism to meet most of the requirements for structural isolators. They have an advantage over flexible vibration isolator, such as performance of High Damping Rubber Bearing (HDRB), but they do not cause an eccentric effect. But, the maximum force of BTI is determined by its bevel angle and friction coefficient, independent of the relative displacement of the isolation layer. This isolator has no isolation effect under small earthquakes, and only large earthquakes can limit the maximum upload earthquake force. Action force of FPS is related to the displacement of the isolation layer. When surface seismicity exceeds design seismicity, the seismic force uploaded to the superstructure may exceed the design value, and the deformation of the structure is hard to estimate. BTI does not have the characteristic frequency of linear spring, and there is no resonance phenomenon in isolation layer. The energy dissipation mechanism of BTI has a friction force and an impact force on a bevel transition, which enhances the energy dissipation effect. Nevertheless, this impact force on bevel transitions causes high frequency and transient acceleration response but does not apply to noise sensitive situations, such as high-tech plant.

Actually, friction force and slop restoring force of BTI happened between bi-tilt symmetrical beveled substrate and slider. When external force to building is less than combination of these two forces, there is no sliding phenomenon of BTI. Thus, isolation effect of BTI does not occur in small earthquakes or intermediate strong winds. Particularly, to overcome strong winds, BTI cannot begin to slide under the maximum consideration of wind force. Otherwise, uploaded load to superstructure, induced by seismic force, is limited by characteristic of BTI. Therefore, upload seismic force to superstructure can be easily controlled to maintain the safety of building. On the other hand, displacement of isolation layer has been restricted by the sliding range at the interface of bi-tilt beveled substrate and slider, which makes it impossible to produce a big displacement. However, friction force and impulse force of BTI happened in sliding process. In order to establish the numerical analysis method for structural engineers to apply this BTI to buildings, mathematical model is derived in this study based on the moving process of BTI. Then, analysis model of BTI element is developed for nonlinear shear building analysis program, GENDYN, based on the second-order dynamic equation, reduced to the first-order differential equation at state space. The fourth-order Runge-Kutta method [39–41] is applied to solve the nonlinear



FIGURE 1: The proposed Bi-Tilt Isolator.

dynamic equation. Finally, test results and simulation results of displacement and acceleration responses of BTI under conditions of full lubrication, mild lubrication, and without lubrication are compared to test and verify the analysis accuracy of this proposed mathematical model, analysis method, and nonlinear analysis program, GENDYN, in this study.

## 2. Mathematical Model for BTI Elements

Bi-Tilt Isolator is composed of two parts: bi-tilt beveled substrate and slider components, where double beveled substrate is connected with structural foundation, while the sliders are connected with the upper structure. In order to adjust the size of friction between the double beveled substrate and sliders, a specific material, such as Teflon, can be embedded in sliders to reduce friction. Sliders are subjected to the weight of superstructure. Therefore, there are considerable normal force and friction between double beveled substrate and sliders. When superstructure is subjected to horizontal forces, such as seismic force and wind force, impact force, or base distribution caused by earthquake, the horizontal force between double beveled substrate and sliders would be increased. When this force is less than the sum of friction and inclined forces between double beveled substrate and sliders, it does not generate the relative displacement. But, when this force is greater than the sum of friction and inclined forces, the relative displacement would occur. Therefore, uploading seismic force to superstructure, caused by seismic disturbance, can be restricted to improve the seismic proof capability of structure when the structure is provided with Bi-Tilt Isolator.

Basic assumptions of this Bi-Tilt Isolator: the foundation of structure can be assumed as a fixed end without displacement, relative to the ground surface displacement coordinate system between double beveled substrate and structural foundation. Mathematical model is derived based on the above-mentioned assumption or the mass of degrees of freedom relative to the slider mass of degrees of freedom is infinite; Figure 2 shows configuration of Bi-Tilt Isolator.

Figure 3 shows the relative motion between double beveled substrate and sliders; the action force between these two parts can be divided into three states.

*2.1. Sliding Upwards Stage.* Referring to free body diagram of Figure 3(a) on the left of the slider, deducting force component on normal direction of slope, tilt force of sliders,

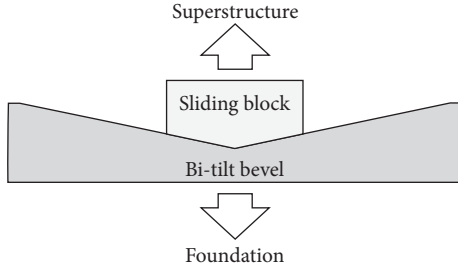


FIGURE 2: Configuration of a Bi-Tilt Isolator.

and directing to neutral position of slope can be expressed as follows:

$$R = W \sin \theta + \mu W \cos \theta, \quad (1)$$

where  $R$  is the tilt force, directing to neutral position of slope on slider;  $W$  is summation of self-weight of structure and slider, acted on the slider;  $\theta$  is slope angle;  $\mu$  is the coefficient of friction.

Resultant force of the tilt acceleration of slider on the tendency of oblique direction of (1) can be expressed as follows:

$$a_s = \frac{W \sin \theta + \mu W \cos \theta}{m_b}, \quad (2)$$

where  $a_s$  is the tilt acceleration of slider and  $m_b$  is slider mass of degrees of freedom (with isolation layer mass).

In analysis mode of shear building, the horizontal degree of freedom is only considered for each floor. Thus, the horizontal component of tendency of oblique acceleration is taken from (2) as follows:

$$a_h = \frac{W \sin \theta + \mu W \cos \theta}{m_b} \cos \theta. \quad (3)$$

Therefore, action force of bi-tilt substrate effect on the slider can be expressed as (4). The product of acceleration and the mass of slider can be obtained as follows:

$$F_e = \frac{W \sin 2\theta}{2} + \mu W \cos^2 \theta. \quad (4)$$

The slider is shown in the left hand side of neutral position of bi-tilt substrate in Figure 3(a), but the direction of action force of bi-tilt substrate is opposite to that in (4).

**2.2. Sliding Downwards Stage.** Referring to free body diagrams on the right side of the slider in Figure 3(b), deducting force component on normal direction of slope, tilt force of slider, and point to the slant neutral position can be expressed as follows:

$$R = W \sin \theta - \mu W \cos \theta. \quad (5)$$

According to the same way of the above-stage procedure, action force of bi-tilt bevel effect on the slider can be expressed as follows:

$$F_e = \frac{W \sin 2\theta}{2} - \mu W \cos^2 \theta. \quad (6)$$

If the slider is located on the left hand side of neutral position of bi-tilt bevel in Figure 3 and slide to the top left hand, the direction of action force of bi-tilt substrate is opposite to that in (6).

**2.3. Downwards/Upwards Transition Stage.** Slider moves from the left hand side to the right hand side of neutral position, and movement direction of slider changes discontinuously. Considering rigid body collision, slider bears the pulse effect in the collision, and the action force approaches infinity result in a discontinuity on the analysis. Figure 4 shows instant speed vector of slider before and after the collision through the neutral position. Before the collision, the slider passes through the neutral position of BTI, shown in Figure 4(a). Slider moves down to the right; the speed vector ( $\vec{v}_0$ ) can be divided into parallel ( $v_0^t$ ) and perpendicular ( $v_0^n$ ) on the right side bevel component. When the slider contacts the right side bevel, the perpendicular component changes but the parallel component does not change. From experimental observation, separation (or jump) phenomenon between the slider and bi-tilt bevel does not happen when slider transits from the neutral position to the other side. Therefore, the assumption of this study is that the perpendicular component of momentum in collisions is "inelastic collision." Otherwise, assuming that the bi-tilt bevel substrates are fixed points, thus, the speed components of sliders ( $v_0^n$ ) before the collision, perpendicular to the right side of slope, disappeared to be zero after the collision. Speed vectors of sliders ( $\vec{v}_1$ ) are the only the parallel component, as shown in Figure 4(b). Therefore, the speed vector of slider before the collision is shown as follows:

$$\vec{v}_0 = v_0^t \vec{t} - v_0^n \vec{n}, \quad (7)$$

where  $\vec{t}$  and  $\vec{n}$  represent the unit tangent vector and unit normal vector, respectively.

Then, speed vector after the collision is expressed as follows:

$$\vec{v}_1 = v_0^t \vec{t}. \quad (8)$$

Thus, the horizontal component ratio of movement speed of slider before and after the collision can be expressed as follows:

$$r_v = \frac{|v_1| \cos \theta}{|v_0| \cos \theta} = \frac{v_0^t}{|v_0|} = \cos 2\theta, \quad (9)$$

where  $\theta$  is the angle between the slope and the horizontal plane;  $2\theta$  is the angle between the right and left bevel.

Assuming the horizontal momentum loss rate is  $\eta$  of slider in transition stage when shear building is applied to analyze. The horizontal momentum loss rate is expressed as follows:

$$\eta = 1 - \cos 2\theta. \quad (10)$$

Thus, sliders bear impulse force  $I$  in transition stage, shown as follows:

$$I = -\eta m_b v_0^h, \quad (11)$$

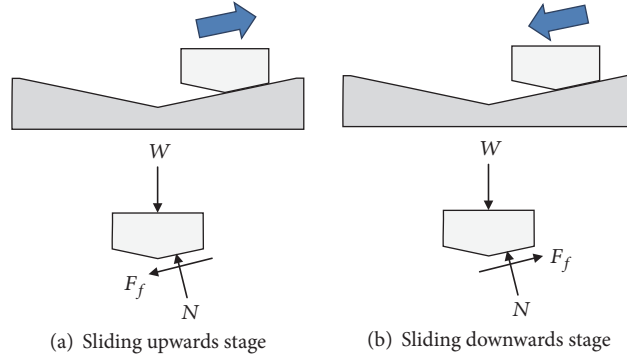


FIGURE 3: Action force between double beveled substrate and sliders in the process of movement.

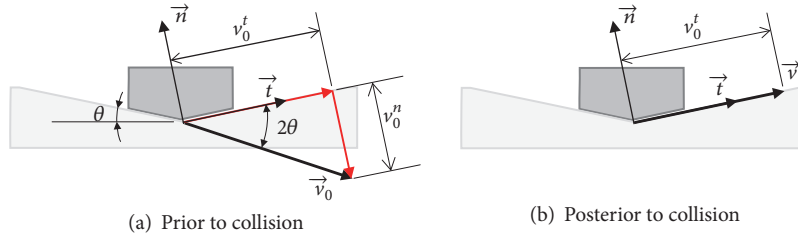


FIGURE 4: Instant speed vector of slider before and after the collision through the neutral position.

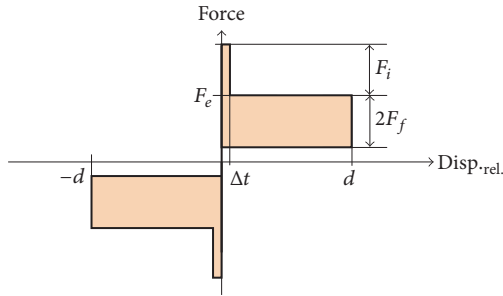


FIGURE 5: Force-relative displacement relation of the BTI element.

where  $v_0^h$  is the horizontal speed component of slider before the collision.

Therefore, assuming sliders bear the action forces of bi-tilt substrate in transition stage is shown as follows:

$$F_i = \frac{\eta m_b v_0^h}{\Delta t}, \quad (12)$$

where  $\Delta t$  is collision time. It is a very short time, assuming  $\Delta t = 0.001$  sec.

Assuming that sliders move distance  $d$  between the right and left hand side of the neutral position, typical action force (which to the left is positive) of bi-tilt substrate will have an effect on slider. Thus, force-relative displacement relation of the BTI element can be derived, as shown in Figure 5.

Kinetic friction force in (4) and (6) is defaulted as constant. But, some studies [42] reveal that friction force is the function of contacted normal force and sliding velocity. Experimental results also display that kinetic friction force

of BTI slider, use of Teflon slider, is highly related to sliding speed. Therefore, to appropriately describe friction with sliding velocity change, all analysis equations must be based on cubic polynomial. Therefore, the friction responses in (4) and (6) of part of friction force should be simulated based on the actual calibration function. Constant friction force and cubic nonlinear friction function are used to simulate the friction responses of numerical simulation in this study and to compare the correlation time history of displacement responses between experiment results and simulation results to verify the reasonableness and accuracy of this proposed mathematical model. At this point, constant friction refers to the minimum root mean square error of constant friction to obtain the best simulation results.

### 3. Analysis Program of the Proposed Model, GENDYN Analysis Procedure

The developed nonlinear shear building analysis program, GENDYN, is applied to process numerical simulation to verify the accurate degree of the proposed model for BTI. The second-order dynamic equation in GENDYN is reduced to the first-order differential equation at state space. Then, the fourth-order Runge-Kutta method is applied to solve the nonlinear dynamic equation.

**3.1. GENDYN Analysis Procedure.** The first-order ordinary differential equation of GENDYN program is discretized as follows.

$$\dot{x} = Ax + Bu, \quad (13)$$

where  $x$  is  $2n$  dimensional state vector;  $A$  is  $2n \times 2n$  system matrix of state space;  $B$  is  $2n \times n$  force distribution matrix of state space;  $n$  is degree of freedom.

State vector is composed of displacement vector and velocity of degree of freedom as follows:

$$x = \begin{Bmatrix} y \\ \dot{y} \end{Bmatrix}, \quad (14)$$

where  $y$  is  $n$  dimensional displacement vector;  $\dot{y}$  is  $n$  dimensional velocity vector.

System matrix  $A$  represents the role of linear components, such as mass, linear spring, and damping as follows:

$$A = \begin{bmatrix} 0 & I \\ -M^{-1}K & -MC \end{bmatrix}, \quad (15)$$

where  $M$  is  $n \times n$  the mass matrix of the second-order ordinary differential equation of motion;  $K$  is  $n \times n$  the stiffness matrix of the second-order ordinary differential equation of motion;  $C$  is  $n \times n$  the damping coefficients matrix of the second-order ordinary differential equation of motion;  $I$  is  $n \times n$  unit vector.

$B$  matrix is used for the conversion of the external force and each acceleration of degree of freedom; for a lumped mass system,  $B$  matrix can be defined as

$$B = \begin{Bmatrix} 0 \\ M^{-1} \end{Bmatrix}. \quad (16)$$

External force vector  $u$  is the summation of external force and nonlinear component force. Equation (13) is solved by numerical analysis method. Two items at the right hand side of equal sign can be combined into one to get (17) as follows:

$$\dot{x} = \begin{bmatrix} I & 0 \\ 0 & M^{-1} \end{bmatrix} \begin{Bmatrix} \dot{y} \\ f \end{Bmatrix}, \quad (17)$$

where  $f$  is the summation of linear component force, nonlinear component force, and external force.

That is,

$$f = u - Kx - C\dot{x}. \quad (18)$$

Thus, (18) can be explained as the summation of internal force and external force, acting on each mass of degree of freedom. It is analyzed by stepwise integration method, and the basic procedure at each time step is as follows:

Time step  $i$ :

Given:  $x_{i-1}, f_{i-1}(x_{i-1}), f_i(x_{i-1})$

Step integral by appropriate method

Update parameters of nonlinear components

The fourth-order Runge-Kutta is analyzed by stepwise integration method to process four times calculation of internal force of component at each step. Nonlinear component parameters for calculation of internal forces at these steps can be assumed as unchanged. Only in the end of each calculation step before it moves on to the next step can the nonlinear component parameters be renewed based on the latest status.

**3.2. The Fourth-Order Runge-Kutta Method.** In order to find solution of ordinary differential equations by stepwise time step, the fourth-order Runge-Kutta method is applied in this study. The Runge-Kutta methods are a family of implicit and explicit iterative methods, which include the well-known routine called the Euler Method, used in temporal discretization for the approximate solutions of ordinary differential equations [39]. Key concept of fourth-order Runge-Kutta algorithm is described as follows [40, 41].

The first-order ordinary differential equation is defined by

$$\frac{dy(t)}{dt} = f(y(t), t). \quad (19)$$

To progress from a point at  $t = t_0$ ,  $y^*(t_0)$ , by one time step,  $h$ , the steps are as follows:

- (1) Approximate derivative at  $t = t_0$ ,  $k_1 = f(y^*(t_0), t_0)$ .
- (2) Intermediate estimate of function at  $t = t_0 + h/2$ , using  $k_1$ ,

$$y_1\left(t_0 + \frac{h}{2}\right) = y^*(t_0) + \frac{k_1 h}{2}. \quad (20)$$

- (3) Estimate of slope at  $t = t_0 + h/2$

$$k_2 = f\left(y_1\left(t_0 + \frac{h}{2}\right), t_0 + \frac{h}{2}\right). \quad (21)$$

- (4) Another estimate of slope at  $t = t_0 + h/2$ , using  $k_2$ ,

$$y_2\left(t_0 + \frac{h}{2}\right) = y^*(t_0) + \frac{k_2 h}{2}. \quad (22)$$

- (5) Another estimate of slope at  $t = t_0 + h/2$

$$k_3 = f\left(y_2\left(t_0 + \frac{h}{2}\right), t_0 + \frac{h}{2}\right). \quad (23)$$

- (6) An estimate of function at  $t = t_0 + h/2$ , using  $k_3$ ,

$$y_3(t_0 + h) = y^*(t_0) + k_3 h. \quad (24)$$

- (7) Estimate of slope at  $t = t_0 + h$

$$k_4 = f(y_3(t_0 + h), t_0 + h). \quad (25)$$

- (8) Estimate of  $y(t_0 + h)$

$$y^*(t_0 + h) = y^*(t_0) + \frac{k_1 + 2k_2 + 2k_3 + k_4}{6} h. \quad (26)$$

**3.3. State Updating Procedure.** Bevel force, impact force, and friction force are three nonlinear force components of BTI. These forces should be renewed by analyzing the state vector of  $x_i$ . Analysis method is described as follows:

- (1) The summation of bevel force and friction force  $F_e$ : value of bevel force is related to displacement and velocity based on (4) and (6) as follows:

$$F_e = -\frac{W \sin 2\theta}{2} \text{sign}(y_{\text{rel},i}) - \mu W \cos^2 \theta \text{sign}(\dot{y}_{\text{rel},i}), \quad (27)$$

where  $y_{rel,i}$  is the relative displacement of the double elements;  $\dot{y}_{rel,i}$  is the relative velocity of the double elements.

- (2) Impact force  $F_i$ : collision time between bevel tilt substrate and slider is very short, happening at the moment when slider moves from the left hand side of neutral point of BTI to the right hand side and occurred in the opposite process. Therefore, assume collision time is  $\Delta t$ . Effect of impact force is used to simulate impulse of slider. In order to avoid lack of impulse,  $\Delta t$  must be set as an integer multiple of setting the time stride for analyzing settings of GENDYN. For example,

$$N_{ti} = \frac{\Delta t}{h}, \quad (28)$$

where  $h$  is setting of the time stride to analyze settings of GENDYN.

Therefore, we detect the following conditions:

$$y_{rel,i} \cdot y_{rel,i-1} < 0. \quad (29)$$

Then, impact force can be assumed as follows:

$$F_i = -\frac{\eta m_b \dot{y}_{rel,i}}{\Delta t} \text{sign}(\dot{y}_{rel}). \quad (30)$$

Time interval of impact force must remain total length of time  $\Delta t$ . Therefore, time of impact points must be stored for checking the analysis time point to calculate the force point and start time of impact force. When the time difference between these two points is less than  $\Delta t$ , impact force is constant as in (30). When the time difference between these two points is greater than  $\Delta t$ , impact force then becomes zero.

#### 4. Experimental Design and Data Acquisition

Bi-tilt beveled substrate and sliders form Bi-Tilt Isolator, BTI. Sliding force will be caused by the shift of slider. Actually, bi-tilt beveled substrate has a symmetrical slope surface; therefore, the slope resorting force is constant. When the superstructure on BTI is subjected to a certain level and above seismic force to overcome the slope resorting force, the sliding force will occur between bi-tilt beveled substrate and sliders. This force is equal to the product of the horizontal component of the sliding down weight of isolator and kinetic friction force. Therefore, the maximum upload force to structure, caused by external force, can be easily predicted and controlled. Otherwise, the displacement at the isolator layer should be reduced to avoid the defects of base isolation. That is, the external force at slider, installed on the base of superstructure, is greater than the sum of friction force and inclined force. Slip phenomenon will be stimulated on BTI to cause displacement and upload external force to structure. There are three stages of the relative motions between bi-tilt beveled substrate and slider: sliding upwards stage, sliding downwards stage, and downwards/upwards transition stage.

Action forces between the bi-tilt beveled substrate and slider are self-weight of superstructure and slider, friction force, and impact force at the collision. In order to capture the real reactions of BTI in the process of movement, experimental design is planned as follows: (1) experimental model: superstructure, self-weight is 20.78 kg, made of aluminum extrusion; isolation layer, made of aluminum extrusion; sliding interface, steel (polished) with Gasket, made of Teflon (Polytetrafluoroethylene); (2) displacement detecting: the developed noncontact measurement technology, Digital Image Correlation (DIC) method is proposed to measure the displacement variation; and (3) acceleration detecting: a smart recorder. Experimental set-up is shown in Figure 6. High speed digital camera is applied to measure all dynamic displacement responses with marks on this test set-up. A smart recorder consists of (1) Arduino Nano, (2) MPU 9250, and (3) SD module. MPU 9250 breakout board is equipped with nine degrees of freedom in inertial measurement unit, IMU and 16-bit ADC (Analog-to-Digital Converter) to detect the acceleration responses in the process of the dynamic test.

Experimental parameters are three tests for WD40 sprayed, WD40 whipped, and without lubrication with initial displacement of  $-50$  mm,  $100$  mm, and  $150$  mm, respectively. Each parameter combination processes two tests to record displacement and acceleration responses by dynamic DIC and MPU9250 accelerometers.

#### 5. Test and Analysis Results and Discussions

All experimental records are analyzed by dynamic analysis to acquire the corresponding optimal parameters based on the optimization procedure. Normal vector equation method is adapted to process parameter optimization. Four friction parameters are used as independent variable, assuming friction is cubic polynomial functions of speed. The minimum root mean square error of time history of displacement for three seconds (901 records) is targeted to process iterative analysis. Parameter analysis of the optimization friction function with the maximum initial displacement ( $150$  mm) for three different lubrication conditions is used to analyze the other displacement responses with various initial conditions and compare with the experimental data. If the optimization parameters by the initial displacement  $150$  mm are applied in the other initial displacements, they can also obtain high-precision displacement reactions. It demonstrates practical application value of this proposed model and program.

Then, assuming that friction is a constant to obtain the minimum root mean square error for simulation and experiment of displacement responses within three seconds, the optimization friction forces for the state of the maximum initial displacement are iterated with three various lubrication conditions. Next, this friction force substitutes into state of the other initial displacements within three seconds to calculate the time history of displacement reactions and compare with the time history of displacement responses of experimental and simulation results, acquired by the cubic polynomial function simulation of friction.

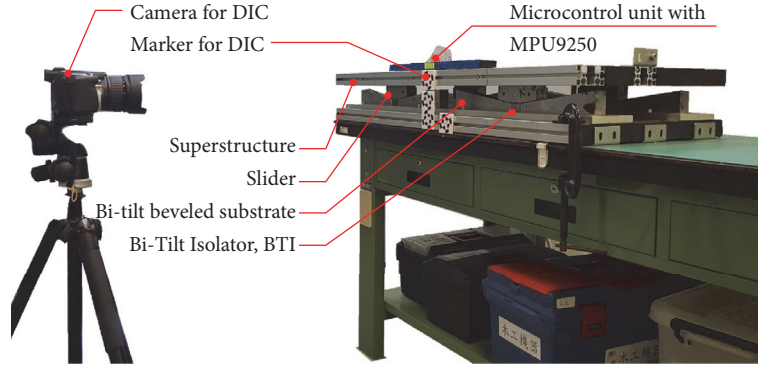


FIGURE 6: Set-up for experimental design and data acquisition.

TABLE 1: Root mean square error of different initial displacement and lubrication conditions with optimal parameters of friction force.

Initial displacement	WD40 sprayed, m	WD40 whipped, m	W/O lubrication, m
0.05 m* (0.048~0.059 m)	0.00028	0.00021	0.00029
	0.00041	0.00033	0.00079
	0.00156	0.00225	0.00453
	0.47%	0.44%	0.54%
0.10 mm* (0.097~0.107 m)	0.00055	0.00046	0.00034
	0.00056	0.00082	0.00094
	0.00182	0.00438	0.00649
	0.51%	0.47%	0.32%
0.15 mm* (0.152~0.155 m)	0.00206	0.00057	0.00061
	0.00206	0.00057	0.00061
	0.00229	0.00829	0.00874
	1.35%	0.37%	0.40%

\*There is slight difference for actual initial displacement in the process of test; the optimization solution with cubic polynomial of friction; the error of the optimum parameters for using the maximum initial displacement simulation; simulation errors with constant friction; the ratio of error of the optimum solutions and initial displacement.

**5.1. Test and Analysis Results.** Table 1 lists all analysis results of the root mean square error of different initial displacement and lubrication conditions with optimal parameters of friction force. Figures 7~9 are analysis results of function of individual best fit and friction force and function of overall best fit and friction force for three different conditions of lubrication with various initial situations. Figure 10 is the comparison of function of overall best fit and friction force with various lubricated conditions. Figures 11~13 reveal simulation time history of displacement for the friction function of measuring displacement and individual best fit and overall best fitting function under conditions of WD40 sprayed with initial displacement 58.68 mm, WD40 whipped with initial displacement 47.98 mm, and without lubrication with initial displacement of 54.05 mm, respectively. Figures 14~16 show simulation time history of displacement for the friction function of measuring displacement and individual best fit and overall best fitting function under conditions of WD40 sprayed with initial displacement of 106.76 mm, WD40 whipped with initial displacement 96.87 mm, and without lubrication with initial displacement of 106.98 mm,

respectively. Figures 17~19 display simulation time history of displacement for the friction function of measuring displacement and individual best fit and overall best fitting function under conditions of WD40 sprayed with initial displacement of 152.56 mm, WD40 whipped with initial displacement of 151.83 mm, and without lubrication with initial displacement of 154.76 mm, respectively. Figure 20 reveals the comparison of RMS displacement errors for simulation results with cubic polynomial friction function and constant friction force.

**5.2. Discussions.** The purpose of this study is to explore the experimental curves of friction within the speed range on optimization of parameters calculation. Even through friction parameters are significantly different, friction force does not have obvious differences. Analysis results for the function of friction force and velocity display that there is little difference between the function of individual best fit and friction and function of overall best fit and friction under condition of full lubrication and slightly large difference happening at high velocity under condition of mild lubrication with large initial displacement. Results for

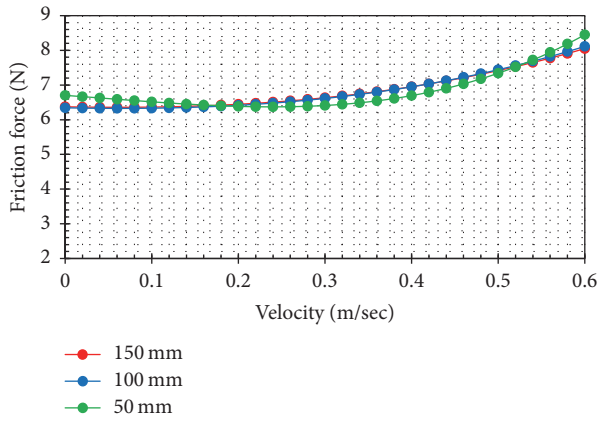


FIGURE 7: Function of individual best fit and friction force and function of overall best fit and friction and friction force (WD40 sprayed) with various initial displacements.

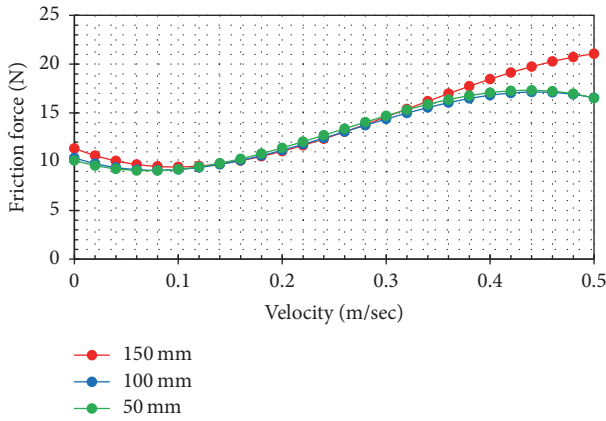


FIGURE 8: Function of individual best fit and friction force and function of overall best fit and friction and friction force (WD40 whipped) with various initial displacements.

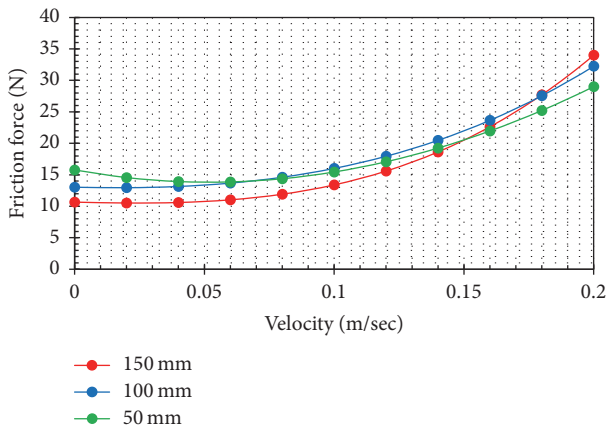


FIGURE 9: Function of individual best fit and friction force and function of overall best fit and friction and friction force (without lubrication) with various initial displacements.

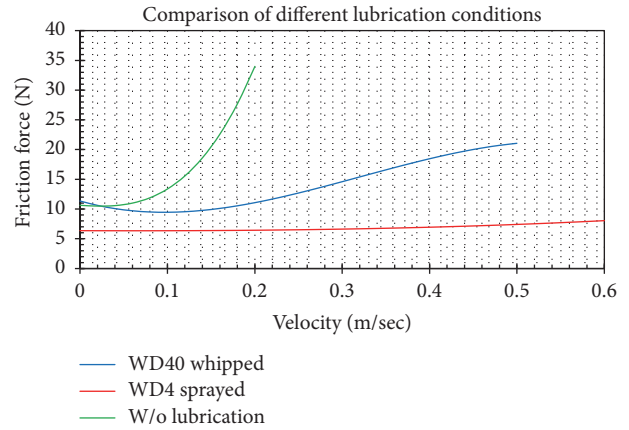


FIGURE 10: The comparison of function of overall best fit and friction force with various lubricated conditions.

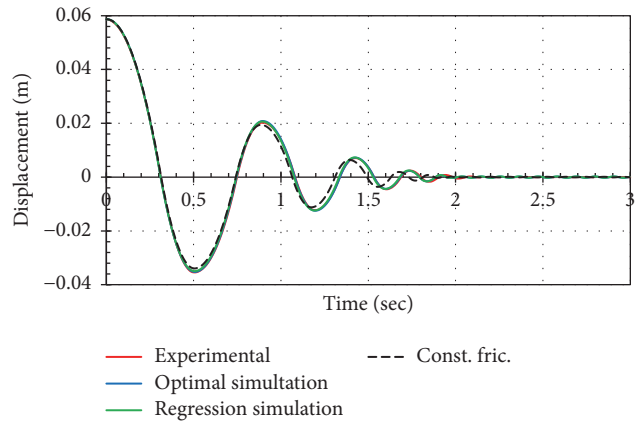


FIGURE 11: Simulation time history of displacement for the friction function of measuring displacement and individual best fit and overall best fitting function (WD40 sprayed with initial displacement of 58.68 mm).

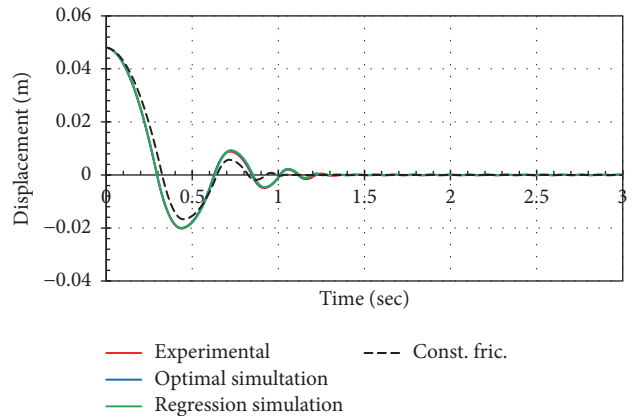


FIGURE 12: Simulation time history of displacement for the friction function of measuring displacement and individual best fit and overall best fitting function (WD40 whipped with initial displacement of 47.98 mm).

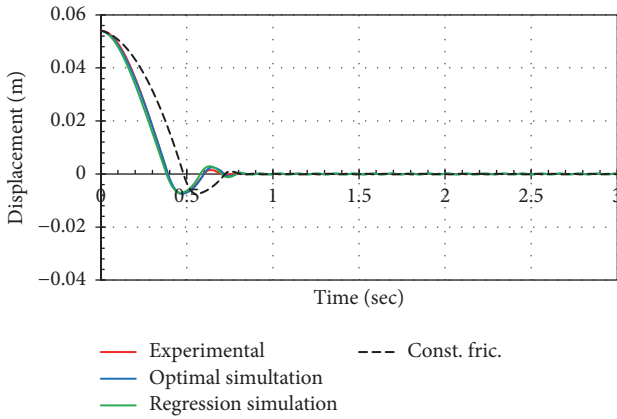


FIGURE 13: Simulation time history of displacement for the friction function of measuring displacement and individual best fit and overall best fitting function (without lubrication with initial displacement of 54.05 mm).

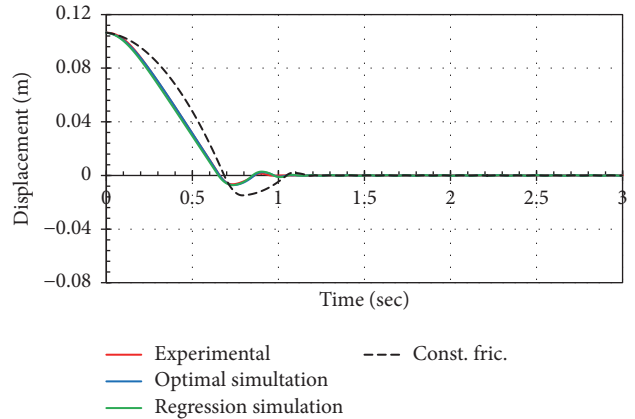


FIGURE 16: Simulation time history of displacement for the friction function of measuring displacement and individual best fit and overall best fitting function (without lubrication with initial displacement of 106.98 mm).

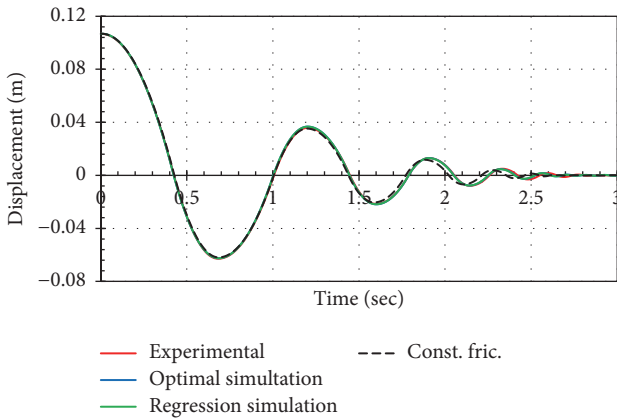


FIGURE 14: Simulation time history of displacement for the friction function of measuring displacement and individual best fit and overall best fitting function (WD40 sprayed with initial displacement of 106.76 mm).

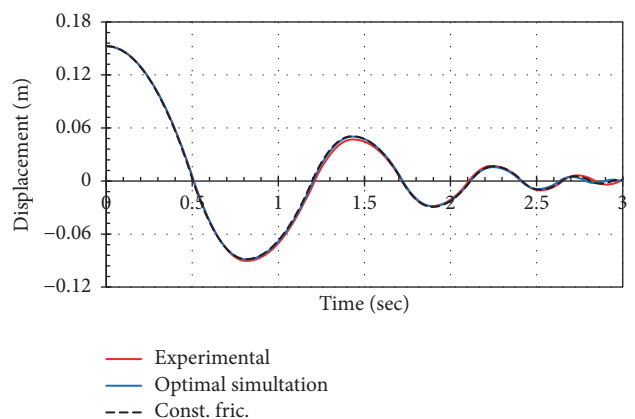


FIGURE 17: Simulation time history of displacement for the friction function of measuring displacement and individual best fit and overall best fitting function (WD40 sprayed with initial displacement of 152.56 mm).

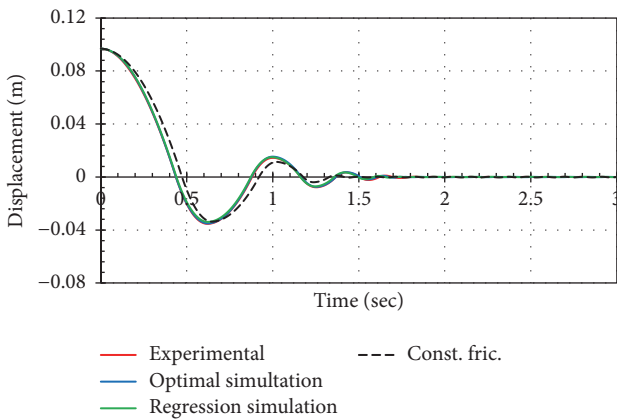


FIGURE 15: Simulation time history of displacement for the friction function of measuring displacement and individual best fit and overall best fitting function (WD40 whipped with initial displacement of 96.87 mm).

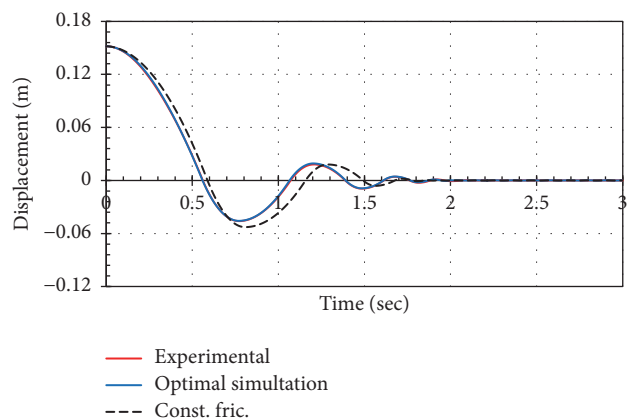


FIGURE 18: Simulation time history of displacement for the friction function of measuring displacement and individual best fit and overall best fitting function (WD40 whipped with initial displacement of 151.83 mm).

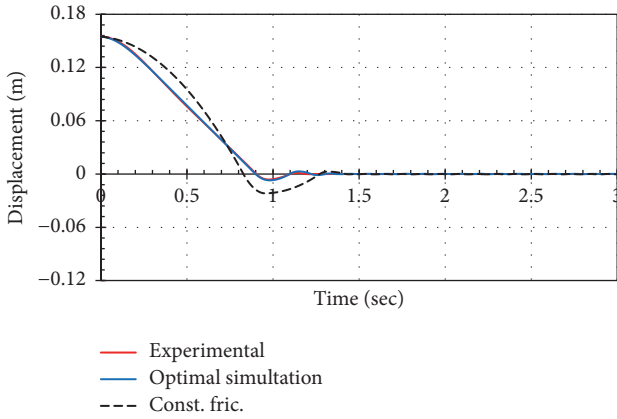


FIGURE 19: Simulation time history of displacement for the friction function of measuring displacement and individual best fit and overall best fitting function (without lubrication with initial displacement of 154.76 mm).

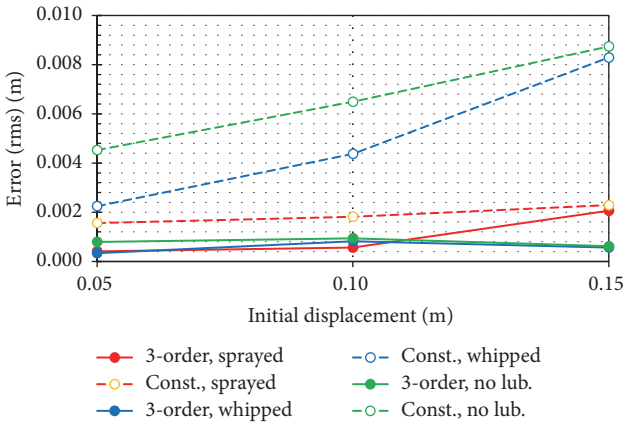


FIGURE 20: The comparison of RMS displacement errors for simulation results with cubic polynomial friction function and constant friction force.

condition of without lubrication show divergence between the analysis results of the function of individual best fit and friction and function of overall best fit and friction with large initial displacement and those of the other two. Then, the comparison results of different lubrication conditions reveal that the function curve of friction force and velocity is very gentle for condition of full lubrication, slightly steep for condition of mild lubrication, and steep for condition of without lubrication. These results show that movement behavior of BTI for function of friction force and velocity can be simulated by this proposed model.

Root mean square error between the experimental data and individual optimization parameters simulation results of displacement reactions are below 1.35% (WD40 sprayed), 0.47% (WD40 whipped), and 0.54% (without lubrication) of initial displacement, respectively. However, the results of optimization parameters for the two tests still have significant differences in exactly the same combination of experimental parameters. Therefore, it can identify that speed responses

of the isolated layers are not high. Although four friction parameters are too many, results of this study confirm that BTI element of GENDYN program does have the capability to simulate the nonlinear responses of structure with combined effect of frictional sliding and collision.

The maximum root mean square error between simulation results and experimental data are 0.00229 m (WD40 sprayed), 0.00829 m (WD40 whipped), and 0.00874 m (without lubrication), using constant friction for Bi-Tilt Isolator with three various conditions. The maximum root mean square errors are 0.00206 m (WD40 sprayed), 0.00082 m (WD40 whipped), and 0.00094 m (without lubrication), respectively, using cubic polynomial function of friction for Bi-Tilt Isolator with three various conditions.

The optimization parameters, set out by the time history of displacement responses with the maximum initial displacement for each condition, are substituted for the rest of the initial displacement conditions to simulate displacement reactions. The comparison of simulation displacement responses and experimental data indicates a high correlation degree. BTI element of GENDYN program provides very good numerical simulation capability for Bi-Tilt Isolator. It can be used to assess structural seismic responses and effect of vibration isolation of structure, installed with BTI.

Simulation results of time history of displacement, by BTI element of GENDYN program, using cubic polynomial function of friction for Bi-Tilt Isolator with three various conditions, are very close to the displacement responses of test. But, when friction parameter sets as constant, analysis precision is relative to the variation of friction and velocity, affected by kinetic friction force.

## 6. Conclusions

Bi-Tilt Isolator (BTI) is a new base isolator for building. Upload force, induced by external force, for superstructure with BTI, can be controlled easily to maintain the safety of structures. Otherwise, displacement of superstructure will be reduced according to the limit displacement of isolation layer. The friction force and impact force between double beveled substrate and slider will be caused in the process of relative movement and nonlinear behavior. In this study, a mathematical model is derived based on the three real movement stages of BTI, sliding upwards stage, sliding downwards stage, and downwards/upwards transition stage. Due to the complicated numerical calculation, nonlinear analysis program, GENDYN, applying the fourth-order Runge-Kutta method, is developed to solve the nonlinear dynamic responses of BTI. Analysis procedure of GENDYN program, discretized ordinary differential equation, is derived and applied for nonlinear components of bevel force, impact force, and friction force of sliding upwards stage, sliding downwards stage, and downwards/upwards transition stage. Then, all dynamic test results of three different lubricated conditions with the maximum initial displacements are analyzed to acquire optimal parameters and assume friction function as cubic polynomial function of speed. These optimal parameters are used to simulate the displacement responses for test model with various initial conditions and also comparison with the

test results. In order to test and verify the analysis accuracy of the derived mathematical model and nonlinear analysis program, GENDYN, the relationship of friction force and velocity for conditions of mild lubrication, full lubrication, and without lubrication, with different initial displacement, is simulated by the function of individual best fit and friction force and function of overall best fit function and friction force. Then, the comparison of time history of measuring displacement, individual best fit, and overall best fit function under conditions of three various lubricated conditions is discussed. The conclusions from a series of test and analysis results are summarized as follows:

- (1) The optimal parameters, acquired by the maximum initial displacement in the process of optimization, can be used to the other initial conditions. The comparison of simulation time history of displacements and test data provides high correlation degree.
- (2) Analysis results show that root mean square error between the experimental data and simulation results of displacement responses are below 1.35% for WD40 sprayed, 0.47% for WD40 whipped, and 0.54% for without lubrication with three different initial displacements, respectively.
- (3) The maximum root mean square error between simulation results and test results for simulating with cubic polynomial function of friction is much less than those of constant friction. Otherwise, there is little difference of the maximum root mean square error between simulation results and test results under condition of full lubrication, not affected by the kinetic friction force.
- (4) Analysis accuracy of this proposed model and program is influenced by the variation of friction force and velocity, caused by the kinetic friction force when the friction force set as constant.
- (5) Application of cubic polynomial function for simulating friction of BTI with three different lubricated conditions can perform very fine simulation results, compared with the test results.

All test and analysis results reveal that this proposed mathematical model and BTI element of GENDYN program, using cubic polynomial function of friction, perform fine simulation capability to assess nonlinear isolation effect of structure installed with BTI. This proposed GENDYN program can be widely applied for structure engineers to design structure, installed with BTI.

### Conflicts of Interest

The authors declare that there are no conflicts of interest regarding the publication of this paper.

### Acknowledgments

The authors would like to acknowledge the support of Taiwan Ministry of Science and Technology through Grants nos. MOST-105-2221-E-260-003 and MOST-105-2221-E-167-001.

### References

- [1] J. T. P. Yao, "Concept of Structural Control," *ASCE Journal of the Structural Division*, vol. 98, no. 7, pp. 1567–1574, 1972.
- [2] J. T. P. Yao, "Practical aspects of structural control," in *Proceedings of the Proc ICOSSAR 89, 5th International Conference on Structural Safety and Reliability*, pp. 479–483, 1989.
- [3] M. A. Basharkah and J. T. P. Yao, "Reliability aspects of structural control," Purdue University, School of Civil Engineering, Structural Engineering (Technical Report) CE-STR, 1982.
- [4] M. D. Symans and M. C. Constantinou, "Passive fluid viscous damping systems for seismic energy dissipation," *ISET Journal of Earthquake Technology*, vol. 35, no. 4, pp. 185–206, 1998.
- [5] K. Mohammadian, K. Goulias, E. Cicek, J. Wang, and C. Maraveas, *Civil Engineering and Urban Planning III*, CRC Press, 2014.
- [6] Taylor Devices Inc and D. P. Taylor, The Application of Energy Dissipating Damping Devices to an Engineered Structure or Mechanism, <http://www.shockandvibration.com>.
- [7] R. J. McNamara, *Seismic Damage Control with Passive Energy Devices: A Case Study*, McNamara/Salvia, Inc. Consulting Structural Engineers, <http://taylordevices.com/literature.html>.
- [8] T. T. Soong and M. C. Constantinou, *Passive and Active Structural Vibration Control in*, Civil Engineering, Department of Civil Engineering, State University of New York at Buffalo, 1994.
- [9] Devices Taylor and M. W. Mosher, Reduction of Shock Response Spectra Using Various Types of Shock Isolation Mounts, <http://taylordevices.com/literature.html>.
- [10] D. P. Taylor and M. C. Constantinou, Fluid Dampers for Application of Seismic Energy Dissipation and Seismic Isolation, <http://taylordevices.com/literature.html>.
- [11] W.-P. Sung, M.-H. Shih, D. Bacinskas, and G. Kaklauskas, "Experimental verification and analysis on seismic proof performance of Velocity and Displacement Dependent Hydraulic Damper (VDHD)," *Information*, vol. 15, no. 2, pp. 741–750, 2012.
- [12] J. T. P. Yao and H. G. Natke, "Effect of active control to structural reliability," in *Proceedings of the 6th ASCE Specialty Conference on Probabilistic Mechanics, and Structural and Geotechnical Reliability*, pp. 373–376, July 1992.
- [13] M. Behrooz, X. Wang, and F. Gordaninejad, "Performance of a new magnetorheological elastomer isolation system," *Smart Materials and Structures*, vol. 23, no. 4, Article ID 045014, 2014.
- [14] H.-J. Jung, D.-D. Jang, H.-J. Lee, I.-W. Lee, and S.-W. Cho, "Feasibility test of adaptive passive control system using mr fluid damper with electromagnetic Induction Part," *Journal of Engineering Mechanics*, vol. 136, no. 2, Article ID 002002QEM, pp. 254–259, 2010.
- [15] S. J. Dyke, B. F. Spencer Jr., M. K. Sain, and J. D. Carlson, "An experimental study of MR dampers for seismic protection," *Smart Materials and Structures*, vol. 7, no. 5, pp. 693–703, 1998.
- [16] K. Liu, L.-X. Chen, and G.-P. Cai, "Active control of a nonlinear and hysteretic building structure with time delay," *Structural Engineering and Mechanics*, vol. 40, no. 3, pp. 431–451, 2011.
- [17] W. D. Iwan and L. J. Wang, "New Developments in Active Interaction Control," in *Proceedings of the 2 International Workshop on Structural Control*, 1996.
- [18] L. J. Wang, "Active interaction control for civil structures," Tech. Rep. 1997, California Institute of Technology, 1997.
- [19] Y. Zhang and W. D. Iwan, "Active interaction control of tall buildings subjected to near-field ground motions," *Journal of Structural Engineering*, vol. 128, no. 1, pp. 69–79, 2002.

- [20] Y. Zhang and W. D. Iwan, "Active interaction control of civil structures—part 1: SDOF systems," *Earthquake Engineering & Structural Dynamics*, vol. 31, no. 1, pp. 161–178, 2002.
- [21] Y. Zhang and W. D. Iwan, "Active interaction control of civil structures. Part 2: MDOF systems," *Earthquake Engineering & Structural Dynamics*, vol. 31, no. 1, pp. 179–194, 2002.
- [22] S. Thenozhi and W. Yu, "Active vibration control of building structures using fuzzy proportional-derivative/proportional-integral-derivative control," *Journal of Vibration and Control*, vol. 21, no. 12, pp. 2340–2359, 2015.
- [23] N. Fallah and M. Ebrahimnejad, "Active control of building structures using piezoelectric actuators," *Applied Soft Computing*, vol. 13, no. 1, pp. 449–461, 2013.
- [24] F. Palacios-Quiñonero, J. Rubió-Massegú, J. M. Rossell, and H. R. Karimi, "Semiactive-passive structural vibration control strategy for adjacent structures under seismic excitation," *Journal of The Franklin Institute*, vol. 349, no. 10, pp. 3003–3026, 2012.
- [25] S. Pourzeynali and P. Jooei, "Semi-active control of building structures using variable stiffness device and fuzzy logic," *International Journal of Engineering, Transactions A: Basics*, vol. 26, no. 10, pp. 1169–1182, 2013.
- [26] K. Hiramoto, T. Matsuoka, and K. Sunakoda, "Simultaneous optimal design of the structural model for the semi-active control design and the model-based semi-active control," *Structural Control and Health Monitoring*, vol. 21, no. 4, pp. 522–541, 2014.
- [27] M. E. Uz and P. P. Sharafi, "Investigation of the Optimal Semi-Active Control Strategies of Adjacent Buildings Connected with Magnetorheological Damper," vol. 6, pp. 523–547, 2016.
- [28] V. A. Matsagar and R. S. Jangid, "Influence of isolator characteristics on the response of base-isolated structures," *Engineering Structures*, vol. 26, no. 12, pp. 1735–1749, 2004.
- [29] R. S. Jangid, "Optimum lead-rubber isolation bearings for near-fault motions," *Engineering Structures*, vol. 29, no. 10, pp. 2503–2513, 2007.
- [30] R. B. Salic, M. A. Garevski, and Z. V. Milutinovic, "Response of Lead-Rubber Bearing Isolated Structure , The 14th World Conference on Earthquake Engineering," in *Proceedings of the Response of Lead-Rubber Bearing Isolated Structure , The 14th World Conference on Earthquake Engineering*, Beijing, China, 2008.
- [31] B. Cunningham, "Using Lead Rubber," in *Bearings in Base Isolation Systems*, 2015, <https://www.comsol.com/blogs/using-lead-rubber-bearings-in-base-isolation-systems/>.
- [32] R. Hanson, *Earthquakes and the benefits of lead rubber bearing base isolation*, 2016, <http://www.stuff.co.nz/87075507/Roger-Hanson-Earthquakes-and-the-benefits-of-lead-rubber-bearing-base-isolation>.
- [33] P. Mishra and G. D. Awchat, "Lead Rubber Bearings as Base Isolating Devices for the Construction of Earthquake Resistant Structures-A Review," *SSRG International Journal of Civil Engineering (SSRG-IJCE)*, vol. 4, no. 7, pp. 18–20, 2017.
- [34] X. M. Tian and M. Lu, "Design of Base-Isolated Structure with Rubber-Bearing , The 14th World Conference on Earthquake Engineering," in *Proceedings of the Design of Base-Isolated Structure with Rubber-Bearing , The 14th World Conference on Earthquake Engineering*, Beijing, China, 2008.
- [35] S. Chirez, S. Fujita, and K. Minagawa, "Effect of nonlinearity of rubber bearing on a seismic isolated structure considering their layout," in *Proceedings of the ASME 2014 Pressure Vessels and Piping Conference, PVP 2014*, USA, July 2014.
- [36] C. S. Tsai, P.-C. Lu, W.-S. Chen, T.-C. Chiang, C.-T. Yang, and Y.-C. Lin, "Finite element formulation and shaking table tests of direction-optimized-friction-pendulum system," *Engineering Structures*, vol. 30, no. 9, pp. 2321–2329, 2008.
- [37] P. Castaldo, B. Palazzo, and P. Della Vecchia, "Seismic reliability of base-isolated structures with friction pendulum bearings," *Engineering Structures*, vol. 95, pp. 80–93, 2015.
- [38] L.-Y. Lu, M.-H. Shih, C.-Y. Wu, and C.-S. Chang-Chien, "Near-fault seismic isolation using sliding bearings with variable curvatures," in *Proceedings of the 13th World Conference on Earthquake Engineering (Oral)*, Vancouver, Canada, 2004.
- [39] [https://en.wikipedia.org/wiki/Runge%E2%80%93Kutta\\_methods](https://en.wikipedia.org/wiki/Runge%E2%80%93Kutta_methods).
- [40] P. L. Devries and J. E. Hasbun, "A first course in computational physics," p. 215, Jones and Bartlett Publishers, 2nd edition, 2011.
- [41] M. Hazewinkel, *Runge-Kutta method*, *Encyclopedia of Mathematics*, Springer Science+Business Media B.V./Kluwer Academic Publishers, 2001.
- [42] J. H. Choo, R. P. Glovnea, A. K. Forrest, and H. A. Spikes, "A low friction bearing based on liquid slip at the wall," *Journal of Tribology*, vol. 129, no. 3, pp. 611–620, 2007.

## Research Article

# Experimental Study on Mechanical and Acoustic Emission Characteristics of Rock Samples under Different Stress Paths

Tao Qin <sup>1,2</sup>, Hongru Sun,<sup>1</sup> Heng Liu,<sup>1</sup> Junwen Zhang <sup>1,3</sup>, Tao Li,<sup>1</sup>  
Gang Liu,<sup>1</sup> and Zhenwen Liu<sup>1</sup>

<sup>1</sup>Heilongjiang Ground Pressure & Gas Control in Deep Mining Key Lab, Heilongjiang University of Science & Technology, Harbin 150022, China

<sup>2</sup>School of Resources & Civil Engineering, Northeastern University, Shenyang 110819, China

<sup>3</sup>College of Resource and Safety Engineering, China University of Mining and Technology, Beijing, China

Correspondence should be addressed to Junwen Zhang; zhangjunwen1977@163.com

Received 20 September 2017; Revised 23 December 2017; Accepted 16 January 2018; Published 13 February 2018

Academic Editor: Paulo B. Gonçalves

Copyright © 2018 Tao Qin et al. This is an open access article distributed under the Creative Commons Attribution License, which permits unrestricted use, distribution, and reproduction in any medium, provided the original work is properly cited.

A series of tests on characteristics of acoustic emission have been performed on sandstone under uniaxial, conventional, and triaxial conditions and the unloading confining pressure path. The failure mode of rock specimen has been scanned by CT and a three-dimensional reconstruction was made. The differences on characteristics of AE, mechanics, and the failure mode of sandstone during the failure process under three paths are studied. The results show that the deformation of rock specimen is bigger, and axial strain and circumferential strain have a deformation platform at peak point of stress under the unloading confining pressure path. Characteristics of AE ringing are significantly affected by the confining pressure and stress path. AE ringing counts peak value, and accumulative ringing on the breaking moment as well as cumulative release energy is higher, which indicates that the rock failure is more violent under the unloading confining pressure path. The failure mode of rock specimen was dominated by shear failure under the conventional triaxial stress path. The tension failure is the main form at a lower initial value of unloading confining pressure, and the shear failure is more prominent at a higher initial value of unloading confining pressure.

## 1. Introduction

During the excavation in underground projects of deep rock, rock masses have been subjected to the stage of loading-unloading repeatedly before the excavation and the condition of unloading after the excavation. That is, rock masses have experienced the mining process from stress of the primary rock, increasing load, and unloading to failure. The stress path is different from unloading and loading, and mechanical properties and the fracture mechanism have both similarities and differences. Safety of the excavation in underground projects is attracting more attention. The study of damage formation in jointed or bulk rock under stress has been a subject of widespread interest, and the results have led to a number of comprehensive texts. Acoustic emission (AE) techniques are broadly applied to rock in order to obtain information on the crack initiation and propagation in rock engineering [1–3].

There are a large number of research results about acoustic emission in the process of rock loading, including uniaxial loading, conventional triaxial loading, unloading confining pressure, and cyclic unloading. The study on acoustic emission characteristics of coal rock has been finished, and the relationship between acoustic emission characteristic parameters and the rock loading failure process has been obtained by the acoustic emission test under uniaxial compression [3–5]. The variant trends are identical between ringing counting and accumulative energy with acoustic emission experiments of the rock damage process under different confining pressures [6, 7]. Acoustic emission events are fewer before yield and gradually become more active during the period of postyield, and then the AE cumulative count and the cumulative number of energy have the singular points obviously in the case of the stress peak [8, 9]. The characteristics of AE are analyzed under the unloading confining pressure, and then the failure characteristics and the mechanism of rock burst



FIGURE 1: The rock servo-controlled rheology testing machine.

are discussed with the granite unloading confining pressure test on acoustic emission under different loading paths [7, 10–13].

There are a lot of research results about the failure process of rock acoustic emission under the loading path, but comparative analyses are not enough on the mechanical properties, acoustic emission characteristics, and failure modes under the paths of uniaxial loading, regular triaxial loading, and unloading confining pressure. Thus, the analysis research has been completed about the mechanical properties and acoustic emission characteristics of rock under different loading paths in this paper. Then, the macroscopic failure morphology is analyzed through the CT scanning and the 3D image reconstruction. A basis for understanding the fracture mechanism of rock materials will be provided by the research results.

## 2. Experimental Processes

In accordance with the test requirements of International Institute of Rock Mechanics, the sandstone samples were processed into standard specimens with a diameter of 50 mm and a height of 100 mm. Test specimens with a wave velocity of about 2000 m/s are screened using the test system of Sonic Viewer-SX rock sample to reduce the discreteness of the specimen.

The loading device adopted the automatic servo rheometer of TOP INDUSTRIE Rock 600-50 (Figure 1), which was composed of servo devices of axial pressure, confining pressure, and seepage pressure. The axial strain was monitored by 2 linear displacement sensors (LVDT). The circumferential strain was monitored by the electronic strain gauge which was placed at the height of the center. Acoustic emission information was collected by Acoustic Emission System of SH-II. Acoustic emission sensors were arranged on outside and below the three-axle chamber. The sampling frequency of acoustic emission was 2.5 MHz, and the gain and the threshold value were 40 dB and 30 dB, respectively.

The sandstone samples were performed by three loading paths, namely, uniaxial compression, the conventional triaxial compression, and unloading confining pressure.

Path 1 is uniaxial compression loading. The samples were loaded to destroy completely by the displacement-controlled method. The axial loading rate was 0.1 mm/min. Three rock

TABLE 1: Experiment results of rock specimens under different stress paths.

Serial number	Density g/cm <sup>3</sup>	$\sigma_1 - \sigma_3$ /MPa	$\sigma_3$ /MPa (initial)	$\sigma_3$ /MPa (destroy)
D <sub>0-2</sub>	2.10	62.6	0	0
S <sub>5-2</sub>	2.10	121.6	5	5
S <sub>10-1</sub>	2.10	145.6	10	10
S <sub>15-3</sub>	2.09	178.5	15	15
S <sub>20-3</sub>	2.12	202.4	20	20
X <sub>5-1</sub>	2.10	96.8	5	4.2
X <sub>10-2</sub>	2.10	119.1	10	5.9
X <sub>15-3</sub>	2.10	144.6	15	12.4
X <sub>20-2</sub>	2.10	160.6	20	13.4

samples were repeated, which were numbered D0-1, D0-2, and D0-3, respectively.

Path 2 is conventional triaxial compression. First, the samples were loaded in the hydrostatic pressure condition ( $\sigma_1 = \sigma_2 = \sigma_3$ ) at the loading rate of 0.05 MPa/s. Then, the specimens were loaded to destroy completely at the axial loading rate of 0.1 mm/min. The confining pressures were 5 MPa, 10 MPa, 15 MPa, and 20 MPa, respectively, and three samples in each condition were repeated, which were numbered S<sub>5-1</sub>, S<sub>5-2</sub>, S<sub>5-3</sub>, S<sub>10-1</sub>, S<sub>10-2</sub>, S<sub>10-3</sub>, S<sub>15-1</sub>, S<sub>15-2</sub>, S<sub>15-3</sub>, S<sub>20-1</sub>, S<sub>20-2</sub>, and S<sub>20-3</sub>, respectively.

Path 3 is unloading confining pressure. First, the samples were loaded in the hydrostatic pressure condition ( $\sigma_1 = \sigma_2 = \sigma_3$ ) at the loading rate of 0.05 MPa/s. Then, the specimens were loaded under about 80% of the ultimate stress at the axial loading rate of 0.1 mm/min. Last, the confining pressure of specimens was unloaded at the axial loading rate of 0.05 MPa/s, in the condition of keeping the main stress constant. The specimens were loaded to destroy completely at the axial loading rate of 0.1 mm/min when destroyed. The initial values of the unloading confining pressure were 5 MPa, 10 MPa, 15 MPa, and 20 MPa, respectively, and three samples in each condition were repeated, which were numbered X<sub>5-1</sub>, X<sub>5-2</sub>, X<sub>5-3</sub>, X<sub>10-1</sub>, X<sub>10-2</sub>, X<sub>10-3</sub>, X<sub>15-1</sub>, X<sub>15-2</sub>, X<sub>15-3</sub>, X<sub>20-1</sub>, X<sub>20-2</sub>, and X<sub>20-3</sub>, respectively.

## 3. The Characteristics of Sandstone of Strength and the Deformation under Different Stress Paths

The rock specimens under different stress paths were analyzed, whose strength was close to the average strength under the different conditions. The rock specimens selected were D<sub>0-2</sub>, S<sub>5-2</sub>, S<sub>5-2</sub>, S<sub>10-1</sub>, S<sub>15-3</sub>, S<sub>20-3</sub>, X<sub>5-1</sub>, X<sub>10-2</sub>, X<sub>15-3</sub>, and X<sub>20-2</sub>. The test results are shown in Table 1.

*3.1. Mechanical Properties of Sandstone under the Paths of Uniaxial and Conventional Triaxial Compression.* The stress-strain curves were shown in Figure 2 under the paths of uniaxial and conventional triaxial compression.

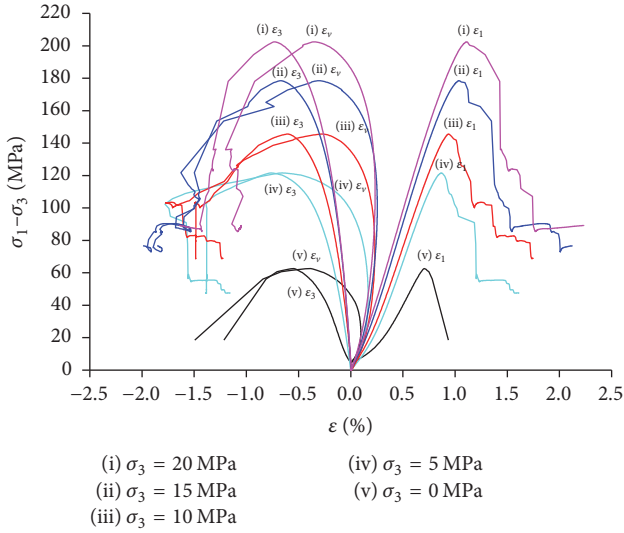


FIGURE 2: Complete stress-strain curves of rock samples under uniaxial and triaxial compression.

(1) Under the different confining pressures, the stress-strain curve of the compression test shows four stages of the rock deformation: the initial compaction phase, elastic stage, plastic stage, and postpeak stage. Sandstone samples had the confining pressure effect obviously. Under the condition of triaxial compression, the initial compaction phase was not obvious, compared with the uniaxial compression test. The main reasons are that the original crack was compacted; the compaction stage was not obvious; the internal original crack of the rock sample was compacted under the condition of hydrostatic pressure. Besides, the compressive strength and the elastic limit of the rock sample became larger with the increase of confining pressure.

(2) Under the condition of triaxial compression, the rock sample still had a certain bearing capacity when it apparently exhibited a macrocrack. When the confining pressures were 5 MPa, 10 MPa, 15 MPa, and 20 MPa, residual strength of rock samples were 55 MPa, 96 MPa, 110 MPa, and 120 MPa, respectively. Because the high confining pressure limited the damage of rock, the plastic deformation and the peak strain of rock increased, and the failure mode of rock gradually transformed into a progressive failure.

**3.2. Mechanical Properties of Sandstone under the Unloading Confining Pressure Path.** Under different initial confining pressures, the curves of the stress-strain test are shown in Figure 3. Under the unloading confining pressure path, the prepeak deformation characteristics were approximately the same, and the peak deformation was different from those of the conventional three-axis tests. Under the confining pressure path, when the stress reached the peak strength, the decrease of the confining pressure would make the lateral slip of rock fractures increase, and the plastic deformation of circumference would increase. There was an obvious deformation yielding platform for the circumferential strain and volume strain.

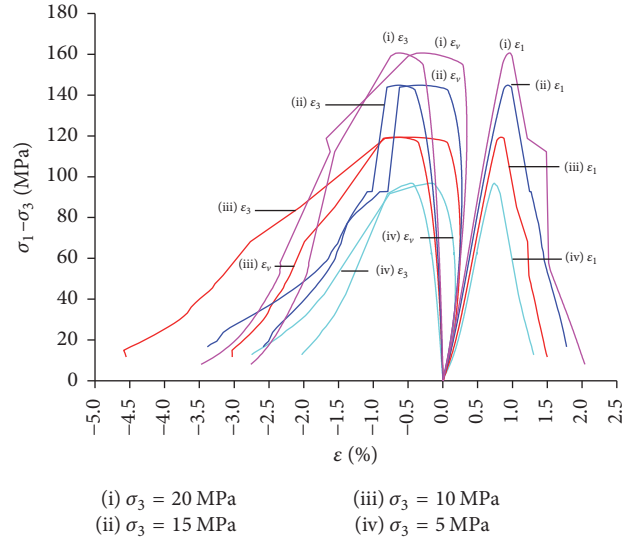


FIGURE 3: Stress-strain curves of rock samples under unloading confining pressure.

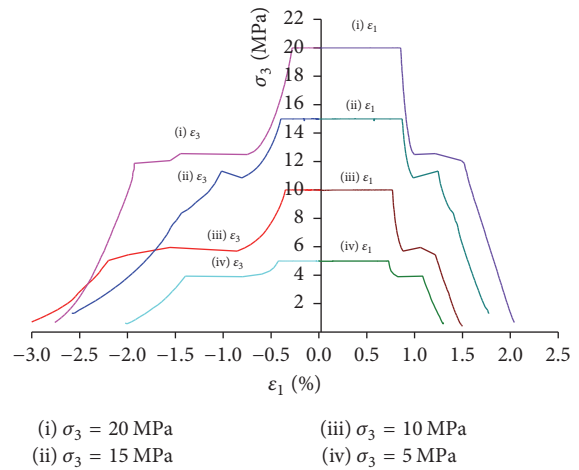


FIGURE 4: Stress-strain curves of axial and circumferential under different initial confining pressures.

Under the unloading confining pressure path, the clear sound for rupture occurred when rocks were broken. The bearing capacity of rocks lost suddenly after rocks were broken, and the residual strength of rocks became smaller. When the value of  $\sigma_1$  remained unchanged and  $\sigma_3$  kept decreasing, the rock was very prone to a sudden failure, leading to the rock burst, such as the wall rock of the underground excavation.

Under different confining pressures, the curves of axial strain and circumferential strain are shown in Figure 4. Under the unloading confining pressure, axial strain was larger, and the axial strain became greater with the confining pressure increasing. The circumferential strain was limited by the confining pressure, and the circumferential strain became smaller with the confining pressure increasing. At the initial stage of the unloading confining pressure, the growth rate of the circumferential strain was much higher than that of the

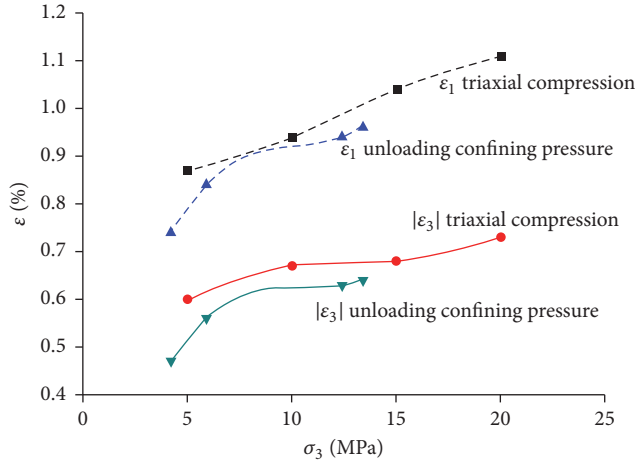


FIGURE 5: Axial strain and circumferential strains of stress peak value under different stress paths.

axial strain. Both the axial strains and circumferential strains were approximately linear related to the confining pressure. The rock samples were in the elastic deformation stage. The rock samples came into the plastic deformation stage with the confining pressure unloaded step by step, and the rates of the axial and circumferential strains increased obviously. In this stage, the circumferential strains increased more sharply, and the circumferential deformation took the dominant position of the rock deformation.

Under different stress paths, the axial and circumferential strains corresponding to the peak stress are shown in Figure 5 (the circumferential strain in the graph is absolute). As seen from the trend line in the chart, the axial and circumferential strains are much less than the conventional triaxial compression path, and its deformation is characterized as the transition from being ductile to being brittle.

Rock mechanical properties under different stress paths correspond to the different states in underground excavation engineering. The changes of mining load will lead to different axial and lateral deformations, and the influences of unloading confining pressure path are more remarkable about the rock deformation, which shows that the rock in the unloading pressure state is more likely to destroy under smaller deformation conditions, and the deformation characteristics of the rock under the unloading pressure condition should be paid more attention with the depth of rock underground engineering increasing.

#### 4. Analysis of Rock Acoustic Emission Characteristics and Failure Modes under Different Stress Paths

AE information can reflect the fracture damage of the rock, which is closely related to the evolution of the primary fissures as well as the initiation, propagation, and coalescence of new fractures in the process of rock loaded. In this paper, the ringing count and ringing accumulation numbers of acoustic emission were measured to analyze acoustic emission

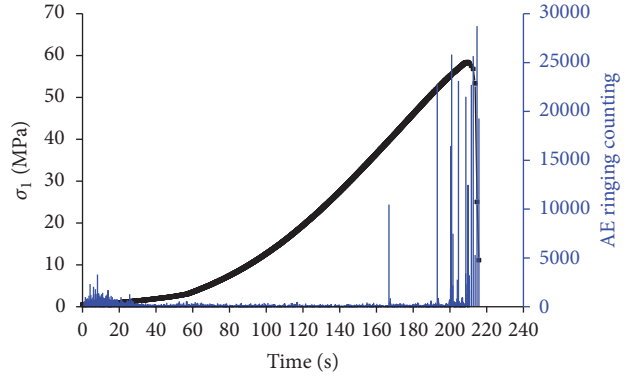


FIGURE 6: Test results of AE ringing counts of rock specimens under uniaxial compression.

characteristics of the rock failure process under different loading paths. The morphology of the rock failure was scanned by the CT system with a microfocus microscope, and the three-dimensional shape of the rock failure was reconstructed by the three-dimensional and visual modeling software.

*4.1. Analysis of Acoustic Emission and the Destruction Process of Rocks.* In the time-domain graph of the acoustic emission wave, the output of a pulse is called AE ringing with transducer in each shock. By contrasting counting characteristics of acoustic emission in different processes of a rock failure, the following conclusions are obtained.

(1) Under the uniaxial compression test, the time-stress-ringing curve of the rock failure process is shown in Figure 6. During the compaction stage, a certain amount of acoustic emission events occurred, and most of them were with small scales. The acoustic emission ring count was low. At the elastic deformation stage, the acoustic emission ringing counts decreased gradually. Following the plastic deformation stage, ringing counts gradually increased with the initiation and propagation of the main fracture. During the last stage of the plastic deformation, the ringing count peaks were centrally active, which could be regarded as forthcoming peak stress of the rock samples. At the peak point of stress, the rock samples underwent a suddenly brittle failure and lost their carrying capacity after the failure, and the acoustic emission events suddenly became silent.

(2) Under the triaxial compression test, the time-stress-ringing curves of the rock failure process are shown in Figure 7. In the early stage of loading, acoustic emission rarely occurred, because a large number of primary pores in the rock had been tightly closed during the application of hydrostatic pressure, and the integrity and stiffness of the rock had increased. During the elastic deformation stage, the acoustic emission ringing counts were relatively inactive, and the values of ringing counts were small; in addition, the duration time of this stage became longer with the confining pressure increasing. Following the plastic deformation stage, rock particles and fractures slip were limited by the confining pressure, which improved the shear strength of the rock. The active degree of AE count has decreased obviously compared

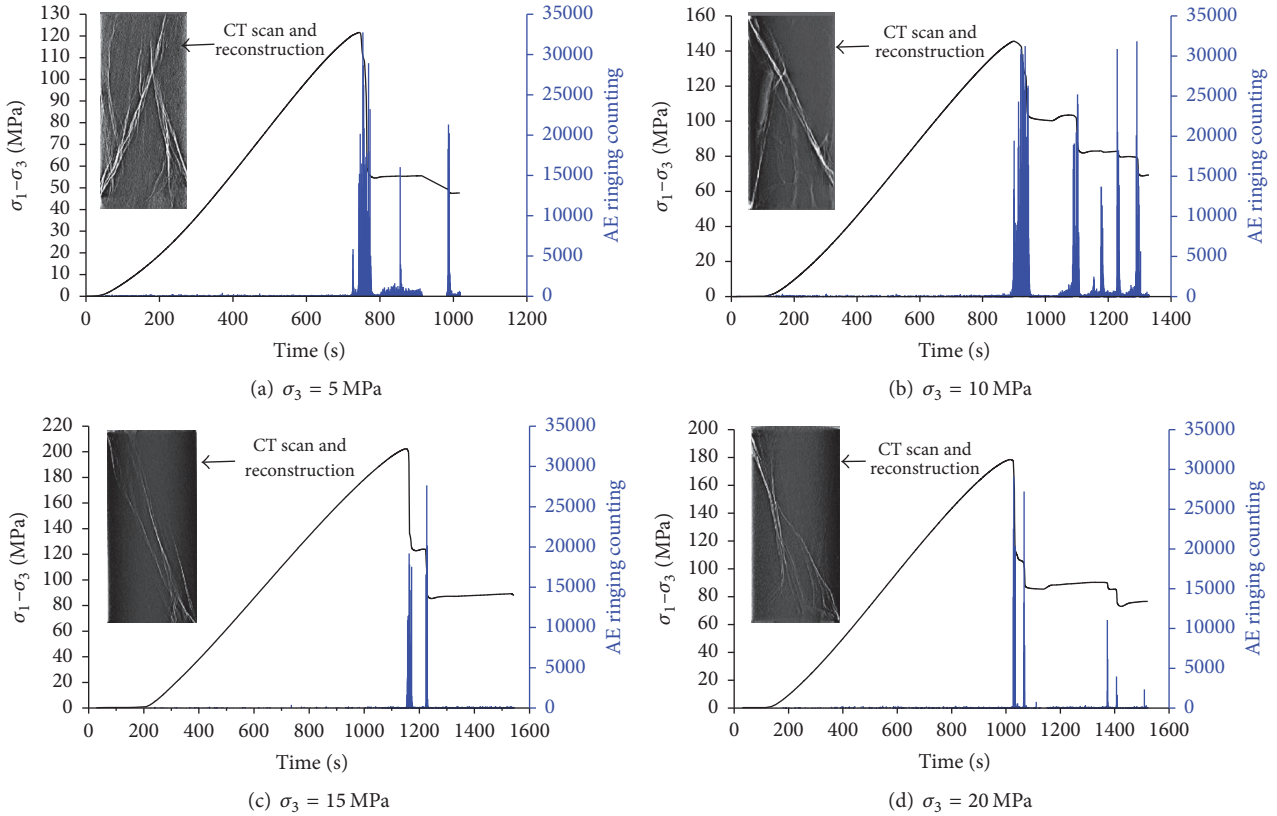


FIGURE 7: Test results of AE ringing counts of rock specimens under different confining pressures.

with the uniaxial compression path, and the active stage of peak value was not obvious. At the loading stage of postpeak, the rock samples still had a certain residual strength because of the confining pressure, and microcracks of rocks continued to emerge and expand after the main fault occurring. At this stage, acoustic emission was more active, and the crack initiation and propagation occurred obviously accompanied by a sudden increase of AE counts. That is, the peak counts of acoustic emission have a good relationship with the stress drop.

Compared with the postpeak stage of different confining pressures, acoustic emission became less active with the increase of the confining pressure, which was due to the crack initiation and propagation limited by the high confining pressure. It can be seen from the CT scanning and 3D reconstruction images that the sandstone under the triaxial compression path was a mainly shear failure, and the fracture of specimens was accompanied by more macroscopic cracks at a low confining pressure. However, the macrocrack decreased obviously under the high confining pressure, which explains the phenomenon that the ringing number of acoustic emission was weakened at the high confining pressure.

(3) Under the unloading confining pressures test, the time-stress-ringing curves of the rock failure process are shown in Figure 8. Before the failure of rock samples, the AE signal was not obvious under the confining pressure, and the ring count of acoustic emission was relatively low, which

was closer to the prepeak stage of the triaxial compression loading. With the confining pressure unloaded, the rock samples lost the confining pressure, and the rocks were damaged suddenly when the pressure reached rock bearing limit, which was accompanied by a great deal of elastic energy suddenly releasing and the ringing number of AE sharply increasing. After a sudden brittle fracture, the rock samples lost their carrying capacity and had almost no residual strength. The ring count of acoustic emission became suddenly silent, and the postdestruction stage was closer to the postpeak stage of uniaxial loading.

The confining pressures were 4.2 MPa, 5.9 MPa, 12.4 MPa, and 13.4 MPa, and the failure modes included tensile failure, tensile failure, tensile shear failure, and shear failure, respectively, at the peak damage when the initial values of unloading confining pressures were 5 MPa, 10 MPa, 15 MPa, and 20 MPa. That is to say, the tensile failure was dominant at the low initial value of the unloading confining pressure, and the shear failure was predominant at the high initial value of the unloading confining pressure.

From the analysis of the failure mechanism of rocks, under the condition of  $\sigma_1$  remaining unchanged and  $\sigma_1 - \sigma_3$  increasing, microcracks were arranged in the direction of the maximum principal stress due to axial stress at the initial stage of the unloading confining pressure. With confining pressure unloaded further and  $\sigma_1 - \sigma_3$  increasing gradually, the microcracks were compressed along the direction of maximum principal stress and the tension cracks were expanded

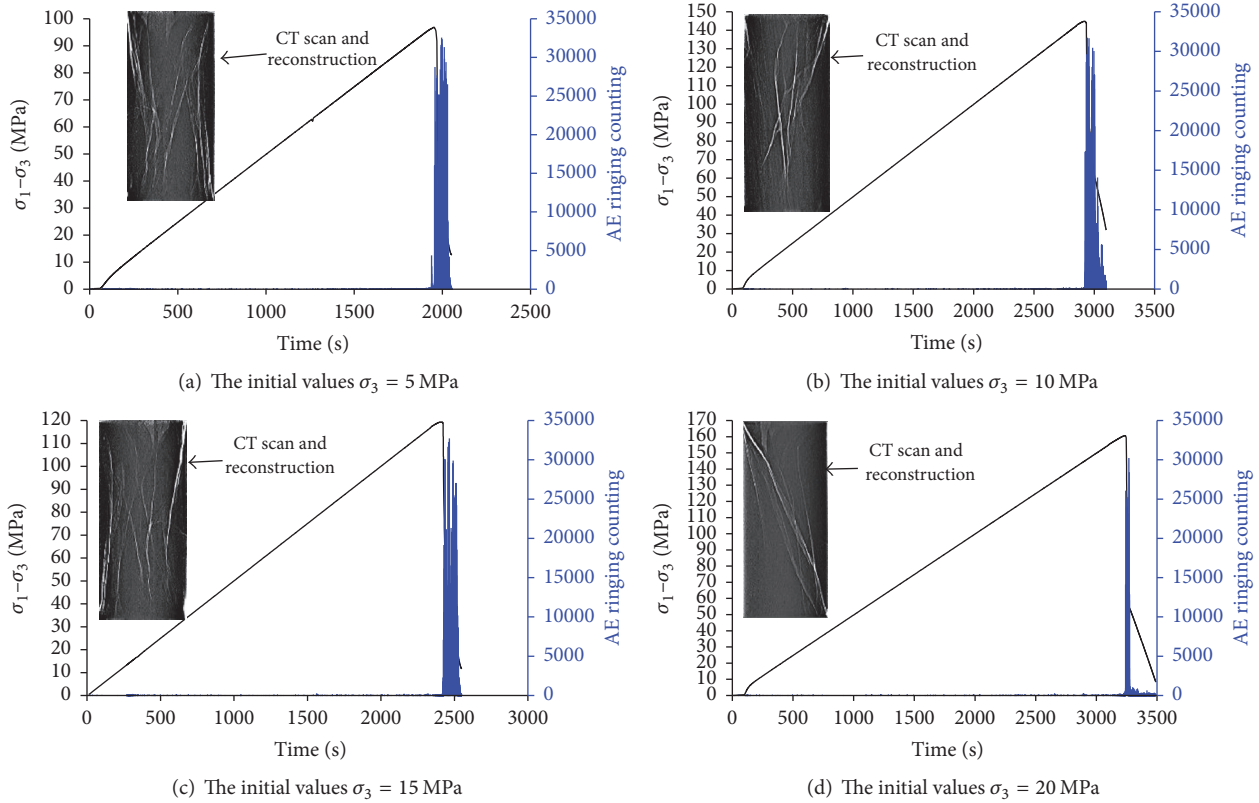


FIGURE 8: Test results of AE ringing counts of rock specimens under the unloading confining pressure.

continuously. This conforms to the Griffith failure criterion. When the confining pressure was unloaded to a certain extent, the tensile stress of the end crack was concentrated, which is due to the rebound deformation caused by pressure unloaded. And, tensile cracks may be connected, and then the failure mode of tensile splitting was formed at a low confining pressure. During the test of this study, the rate of confining pressure unloaded was 0.05 MPa/s, a lower rate. Therefore, the confining pressure remained at a relatively high degree during the formation of the main fracture, which limited the rate of the lateral deformation. As a result, the rock samples were still subjected to a shear failure at the high initial confining pressure.

**4.2. Analysis of Acoustic Emission Ringing Cumulative Number.** The cumulative number of AE rings reflects the variation of cumulative damage during the rock failure. Due to limited length of this article, only the tests of the uniaxial, conventional triaxial compression ( $\sigma_3 = 20$  MPa) and the unloading confining pressure (initial values of the confining pressure  $\sigma_3$  is 20 MPa) were listed in this paper. The curves of time-stress-cumulative number of rings are shown in Figure 9 during the process of the rock failure. The main conclusions are obtained by the comparison with the number of rings accumulated under different loading paths.

(1) Under the uniaxial compression path, the curve of cumulative number of rings could be divided into 3 stages: the initial growth stage, the stable growth stage, and the rapid

growth stage. There was no obvious quiet period in the whole loading process.

(2) Under the conventional triaxial compression path, the curve of cumulative number of rings could be divided into 3 stages: the quiet stage, the sudden increase stage, and the postpeak unstable stage. Due to the effects of the confining pressure, there was an obvious quiet period in the curve of cumulative number of rings, and the longer the confining pressure lasted for, the longer the stationary phase lasted. During the postpeak stage, each apparent stress drop was accompanied by a sudden increase in the cumulative number of AE rings.

(3) Under the unloading confining pressure path, the curve of cumulative number of rings had obvious stages of a calm and sudden increase. There was a sudden failure in the peak, and no instable stage in the postpeak.

**4.3. Analysis of AE Characteristics and Failure Modes under Different Stress Paths.** (1) Under the paths of conventional triaxial compression and unloading compression, AE counts had no obvious active stage compared with the uniaxial test in the latter stage of the plastic deformation.

The rock specimens were destroyed suddenly under the paths of uniaxial and unloading compression, and AE was not obvious in the postpeak stage. What is more, during the postpeak stage of the conventional triaxial compression path, the residual strength of rock samples remained under the action of the confining pressure, and there were strong

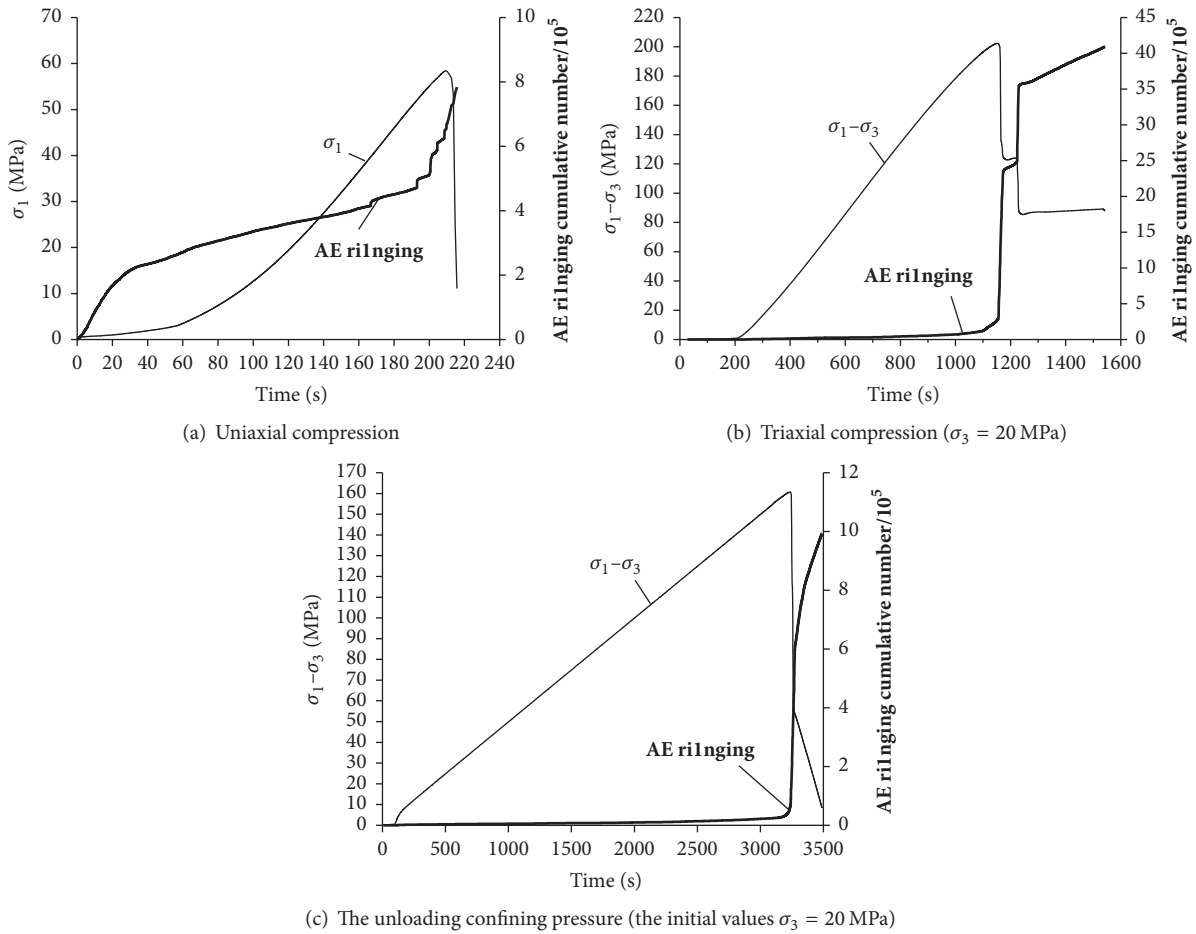


FIGURE 9: Test results of AE accumulative ringing of rock specimens under different stress paths.

acoustic emission signals due to the friction of the crack growth and the fracture surfaces.

Under conventional triaxial compression paths and unloading confining pressure paths, the peak curves of acoustic emission count are shown in Figure 10. Under the unloading confining pressure path, the ring count peak of rock samples was obviously larger than those of conventional triaxial compression paths. The main causes were sudden and strong brittle fractures of rock specimens under the unloading confining pressure paths. When the rock samples failed, the release of elastic energy was more concentrated and a larger scale of fractures was produced.

In order to analyze the influences of the confining pressure during a rock failure, a cumulative number of moments ringing were analyzed under different stress conditions. Trend lines of AE accumulative ringing of rock specimens on the breaking moment are shown in Figure 11. Under the unloading confining pressure path, the cumulative number of AE ringing was larger than those of conventional triaxial compression paths. The main causes are that a larger scale of fractures of rock specimens was produced and the moment accumulated damage was also greater during the rock breaking because of the elastic energy sudden release.

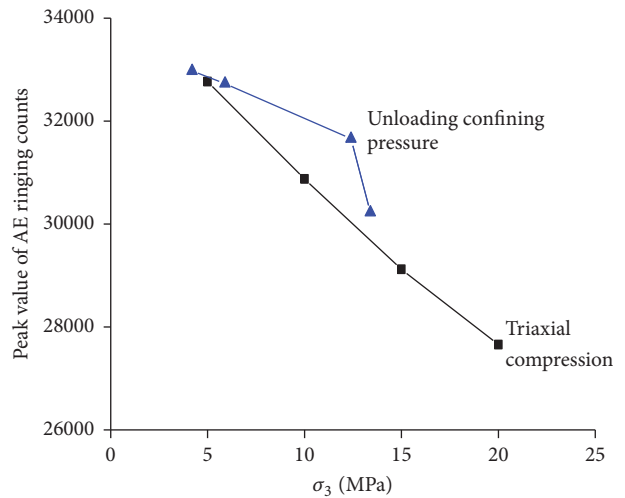


FIGURE 10: Peak value of AE ringing counts under different stress paths.

From the macroscopic failure morphology of rock samples, a shear failure of sandstone was dominated under the

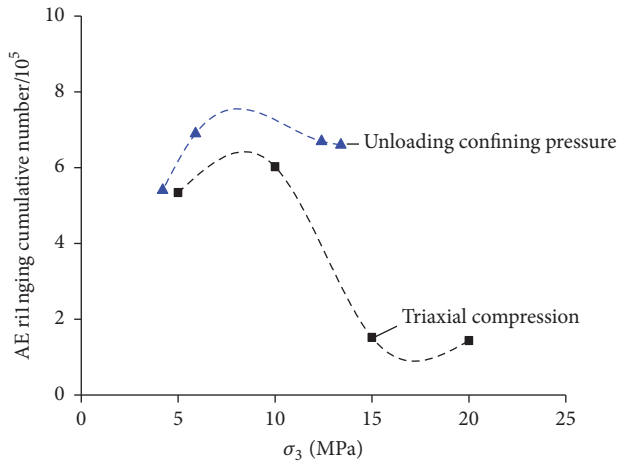


FIGURE 11: The trend line of AE accumulative ringing of rock specimens on the breaking moment.

conventional triaxial compression path, and there were both a tensile failure and a shear failure under the unloading confining pressure path. Under the unloading confining pressure path, the number and size of macrocracks increased obviously comparing with the conventional triaxial compression path after the rock failure.

## 5. Conclusion

In this paper, a series of tests on characteristics of acoustic emission have been performed on sandstone under different stress paths, and the failure modes of rock specimens have been scanned by the CT after the rock destroy. The differences in characteristics of AE, mechanics and failure modes of sandstone during the failure process under three paths were studied. The main conclusions are as follows.

(1) Under different stress paths, the deformations of sandstone samples have significant differences. Under the unloading confining pressure path, the circumferential and volumetric deformations have more obvious influences on the rock. Under the confining pressure path, the decrease of the confining pressure makes the lateral slip of rock fractures increase, and there are obviously deformation yielding platforms for the circumferential strain and volume strain at the peak point.

(2) Under the unloading confining pressure path, the axial strain and the hoop strain are smaller than those of the conventional triaxial compression path, and under the unloading state of the underground excavation, the rock is more likely to be destroyed by smaller deformation conditions. With the depth of rock underground engineering increasing, the deformation characteristics of the rock should be paid more attention under the unloading condition.

(3) Under the uniaxial loading path, acoustic emission is produced significantly in the compaction stage. Under the conventional triaxial compression path, AE signal is not obvious due to the primary pores of the rock closed by hydrostatic pressure, and the sudden increasing phenomenon of AE ringing is weakening with initiation and propagation

of the crack limited by the high confining pressure. Under the unloading confining pressure path, rock specimens are destroyed suddenly and strongly due to elastic energy releasing intensely, and the peak and accumulated number of AE ringing are greater than those of the conventional triaxial compression path.

(4) Under conventional triaxial compression path, the shear failure of sandstone is dominated, and there are both a tensile failure and a shear failure under the unloading confining pressure path. Under the conventional triaxial compression path, the initiation and propagation of microcracks are inhibited by the confining pressure, and the number of macroscopic cracks produced under a low confining pressure is much higher than those of a high confining pressure. Under the unloading confining pressure path, the rebound deformation caused by the unloading confining pressure makes the tensile stress concentrated and expanded at the end of the tension crack. Then the tensile fracture may be interconnected directly under a low confining pressure, and the tensile splitting failure mode will be formed. In the case of the high initial confining pressure, the concentrated level of tensile stress will be weakened. The rate of the lateral deformation was limited by the high confining pressure, and a shear failure still occurs in rock samples.

## Conflicts of Interest

The authors declare that they have no conflicts of interest.

## Acknowledgments

The research presented in this paper has been supported jointly by the National Key Research and Development Program (Grant no. 2016YFC0600901), Natural Science Foundation of Heilongjiang Province (Grant no. E2015031), and the National Natural Science Foundation (NNSF) of China (Grant nos. 51604100, 51574114, 51574115, and 51474099).

## References

- [1] T. Ishida, T. Kanagawa, and Y. Kanaori, "Source distribution of acoustic emissions during an in-situ direct shear test: implications for an analog model of seismogenic faulting in an inhomogeneous rock mass," *Engineering Geology*, vol. 110, no. 3-4, pp. 66-76, 2010.
- [2] V. Mlakar, F. P. Hassani, and M. Momayez, "Crack development and acoustic emission in potash rock," *International Journal of Rock Mechanics and Mining Sciences & Geomechanics Abstracts*, vol. 30, no. 3, pp. 305-319, 1993.
- [3] E. Aker, D. Kühn, V. Vavryčuk, M. Soldal, and V. Oye, "Experimental investigation of acoustic emissions and their moment tensors in rock during failure," *International Journal of Rock Mechanics & Mining Sciences*, vol. 70, pp. 286-295, 2014.
- [4] J. Xu, S. Li, X. Tang et al., "Rock fatigue damage evolution based on acoustic emission," *Journal of University of Science and Technology Beijing*, vol. 31, no. 1, pp. 19-24, 2009.
- [5] B. B. Gao and H. G. Li, "Research on coal samples damage model based on acoustic emission parameters," *Journal of Disaster Prevention and Mitigation Engineering*, vol. 34, no. 1, pp. 101-106, 2014.

- [6] H. Ji and X. Lu, "Characteristics of acoustic emission and rock fracture precursors of granite under conventional triaxial," *Chinese Journal of Rock Mechanics and Engineering*, vol. 34, no. 4, pp. 694–702, 2015.
- [7] V. L. Shkuratnik, Y. L. Filimonov, and S. V. Kuchurin, "Regularities of acoustic emission in coal samples under triaxial compression," *Journal of Mining Science*, vol. 41, no. 1, pp. 44–52, 2005.
- [8] C.-D. Su, X.-X. Zhai, B.-F. Li, and H.-Q. Li, "Experimental study of the characteristics of acoustic emission for sandstone specimens under uniaxial and triaxial compression tests," *Journal of Mining and Safety Engineering*, vol. 28, no. 2, pp. 225–230, 2011.
- [9] M. Cai, H. Morioka, P. K. Kaiser et al., "Back-analysis of rock mass strength parameters using AE monitoring data," *International Journal of Rock Mechanics and Mining Sciences*, vol. 44, no. 4, pp. 538–549, 2007.
- [10] W.-Z. Chen, S.-P. Lü, X.-H. Guo, and C.-J. Qiao, "Unloading confining pressure for brittle rock and mechanism of rock burst," *Chinese Journal of Geotechnical Engineering*, vol. 32, no. 6, pp. 963–969, 2010.
- [11] A. Lavrov, "Kaiser effect observation in brittle rock cyclically loaded with different loading rates," *Mechanics of Materials*, vol. 33, no. 11, pp. 669–677, 2001.
- [12] J. S. Kim, K. S. Lee, W. J. Cho, H. Choi, and G. Cho, "A comparative evaluation of stress–strain and acoustic emission methods for quantitative damage assessments of brittle rock," *Rock Mechanics and Rock Engineering*, vol. 48, no. 2, pp. 495–508, 2015.
- [13] J. He, L. M. Dou, W. Cai, Z. L. Li, and Y. L. Ding, "In situ test study of characteristics of coal mining dynamic load," *Shock and Vibration*, vol. 2015, Article ID 121053, 8 pages, 2015.

## Research Article

# Multistability in Horizontal Platform System with and without Time Delays

**Karthikeyan Rajagopal** , **Prakash Duraisamy,**  
**Riessom Weldegiorgis, and Anitha Karthikeyan**

*Centre for Nonlinear Dynamics, Defense University, Bishoftu, Ethiopia*

Correspondence should be addressed to Karthikeyan Rajagopal; rkarthikeyan@gmail.com

Received 2 September 2017; Revised 25 December 2017; Accepted 11 January 2018; Published 11 February 2018

Academic Editor: José Manoel Balthazar

Copyright © 2018 Karthikeyan Rajagopal et al. This is an open access article distributed under the Creative Commons Attribution License, which permits unrestricted use, distribution, and reproduction in any medium, provided the original work is properly cited.

Chaotic behavior and bifurcation analysis of horizontal platform systems (HPS) have been investigated widely by many researchers. However, the multistable features of such systems have not been investigated, and hence we identified the multistable parameter and investigated the coexisting attractors of the HPS. To understand the effects of time delays on the nonautonomous and autonomous HPS, we introduced a constant time delay in the state feedback variable. Investigation of the bifurcation of the time delayed HPS with time delay and parameters reveals that the system behavior differs between the autonomous and nonautonomous HPS. To investigate the multistability existence in time delayed HPS, we plot the bifurcation of the autonomous HPS and show the multistability and coexisting attractors.

## 1. Introduction

Mathematical models of most of the physical systems show complex nonlinear behaviors. The superposition principle is very useful in linear analysis, which is not valid in the case of nonlinear analysis. The uncertainty with system models often demands the nonlinear dynamical models to be analyzed without linearization. Since mass, damper, and spring are the basic components of a vibratory system, nonlinearity may be introduced into the governing differential equation through any of these components. Chaos modeling has applications in many areas in science and engineering [1]. Some of the common applications of chaotic systems in science and engineering are chemical reactors, Brusselators, dynamos, tokamak systems, biology models, neurology, ecology models, and memristive devices. Chaotic phenomenon was observed in several mechanical systems [2]. Chaos may be described as bounded random like motion exhibited by deterministic nonlinear systems characterized by their sensitivity to initial conditions. Not all nonlinear systems exhibit chaos nor does chaos occur for all combinations of system parameters and initial conditions for a given system [3].

The horizontal platform system (HPS) holds a freely rotating platform about its horizontal axis especially in offshore applications. An accelerometer is placed over the platform in order to sense the displacement; accordingly, the platform is balanced by producing inverse torque to maintain the stability of HPS. Horizontal platform system (HPS) exhibits chaotic behavior on some specified conditions [4]. Chaotic motion and bifurcation analysis of a HPS under specified conditions with its dynamical response as a function of the torque is discussed in [5]. An adaptive sliding mode controller (ASMC) is designed and implemented to control the chaotic behavior in HPS with parameter uncertainties. HPS with model and parameter uncertainties with external disturbances is investigated, the chaotic behavior of the system is controlled using HPS synchronization with time varying control [6], and the dynamic analysis of a fractional order horizontal platform system (FOHPS) and its fractional order finite time chaos control design are investigated in [7].

Motivated by the above mentioned discussions, we are interested in analyzing the HPS with autonomous and nonautonomous modeling. Most of the earlier literature has discussed and analyzed the regular bifurcation pattern of the HPS, but none has presented the multistable behavior of the

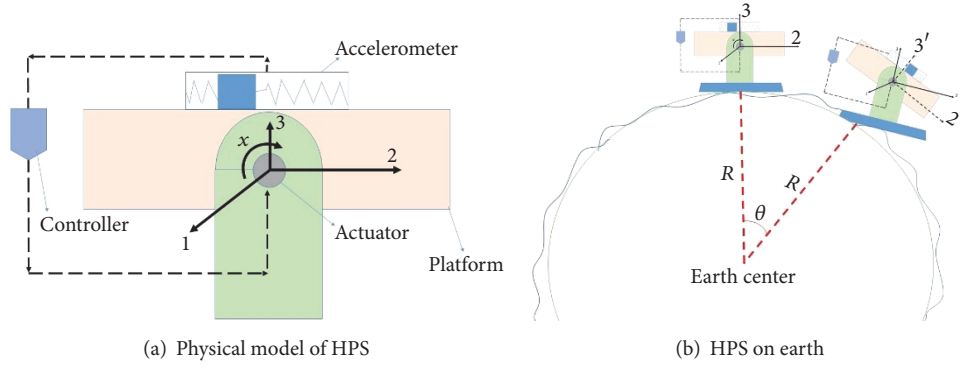


FIGURE 1

HPS which we have presented here. We also discuss the effect of constant time delays on the nonlinear behavior of the HPS and show the effect of time delays on autonomous and nonautonomous HPS.

## 2. Mathematical Modeling of HPS

We have used the HPS model described in [4–7] as given by Figures 1(a) and 1(b). While the platform varies from horizontal position, the accelerometer measures and sends it to the controller and the controller will produce inverse torque in order to stabilize the platform; the actuator will execute the inverse torque.

The basic assumption is that the horizontal platform rests on spherical joint which enables movement in coupled manner when it is displaced in one rotational axis.  $x(t)$  represents the rotation of the platform in relation to the earth. Consider  $A_1$ ,  $A_2$ , and  $A_3$  are the inertia moments of the platform for axes 1, 2, and 3, respectively.  $D$  denotes the damping coefficient,  $R$  represents radius of the earth,  $r$  is the proportional constant of the accelerometer,  $g$  denotes gravity, and  $F \cos \omega t$  is the harmonic torque.

The governing law is Newton's 2nd law of motion for rotational motion:

$$\sum M = I\ddot{x}. \quad (1)$$

The net moment acting on a rigid body is equivalent to the product of the moment of inertia and angular acceleration about an axis.

$$\sum M = A_1\ddot{x}. \quad (*A)$$

When the horizontal platform is displaced with a relative angular displacement " $x$ ," the moments produced on the consequence are the resisting moment due to damping (fluidic friction, Coulomb friction), the moment due to accelerometer, and the coupling effect.

The damping torque is

$$T_d = D\dot{x}. \quad (*B)$$

Force acting due to accelerometer is

$$\cos(90 - x) = \frac{f}{mg} \quad (2)$$

$$f = mg \cos(90 - x).$$

The offset distance between center of mass of accelerometer and the center of mass of platform is " $a$ ." The accelerometer torque moment is

$$M = f \cdot a \quad (3)$$

$$M = mga \cos(90 - x).$$

Consider  $ma = r$ ,

$$M = rg \sin x. \quad (*C)$$

Moment equation with angular velocities in terms of Euler angles and Euler rates is

$$L = I_x \dot{p} + I_{xz} \dot{r} + qr(I_z - I_y) - I_{xz} pq, \quad (4)$$

where  $q = \dot{\theta} \cos \phi + \dot{\psi} \cos \theta \sin \theta$ ,

$$r = \dot{\psi} \cos \theta \cos \phi - \dot{\theta} \sin \phi$$

$$\theta = \text{Pitch angle} \quad (5)$$

$$\phi = \text{Roll angle}$$

$$\psi = \text{Yaw angle.}$$

Since  $I_{xz} = 0$  and  $I_x \dot{p} = A_1 \ddot{x}$ ,

$$L = A_1 \ddot{x} + qr(I_z - I_y)$$

$$L = A_1 \ddot{x} + (\dot{\theta} \cos \phi + \dot{\psi} \cos \theta \sin \theta) \quad (6)$$

$$\cdot (\dot{\psi} \cos \theta \cos \phi - \dot{\theta} \sin \phi) \cdot (A_2 - A_3).$$

We know that  $\dot{\psi} = 0$

$$L = A_1 \ddot{x} - \dot{\theta}^2 \cos \phi \sin \phi \cdot (A_2 - A_3)$$

$$= A_1 \ddot{x} - \frac{\dot{\theta}^2 R}{R} \cos \phi \sin \phi \cdot (A_2 - A_3). \quad (7)$$

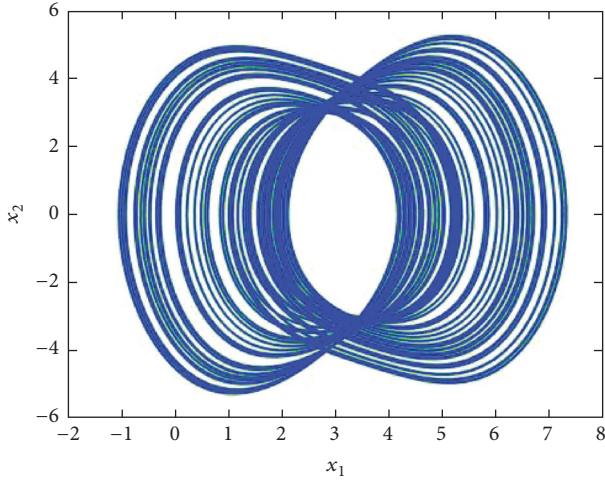


FIGURE 2: Phase portrait of the HPS.

Since  $\theta^2 R = 3g$ ,  $\phi = x$ ,

$$L = A_1 \ddot{x} - \frac{3g}{R} \cos x \sin x \cdot (A_2 - A_3). \quad (*D)$$

Equation of motion can be formulated using (\*A), (\*B), (\*C), and (\*D):

$$\begin{aligned} A_1 \ddot{x}(t) + D\dot{x}(t) + rg \sin x(t) \\ - \frac{3g}{R} (A_2 - A_3) \cos x(t) \cdot \sin x(t) = F \cos \omega t. \end{aligned} \quad (*)$$

Let us define the new states as  $x_1(t) = x(t)$ ,  $x_2(t) = \dot{x}(t)$  and new parameters as  $a = D/A_1$ ,  $b = rg/A_1$ ,  $l = (3g/A_1 R)(A_2 - A_3)$ ,  $h = F/A_1$ , and (\*) can be rewritten as

$$\begin{aligned} \dot{x}_1(t) &= x_2(t) \\ \dot{x}_2(t) &= -ax_2(t) - b \sin x_1(t) + l \cos x_1(t) \sin x_1(t) \\ &\quad + h \cos \omega t. \end{aligned} \quad (8)$$

The autonomous form of the HPS defined in (8) can be given by

$$\begin{aligned} \dot{x}_1(t) &= x_2(t) \\ \dot{x}_2(t) &= -ax_2(t) - b \sin x_1(t) + l \cos x_1(t) \sin x_1(t) \\ &\quad + h \cos x_3(t) \\ \dot{x}_3(t) &= \omega. \end{aligned} \quad (9)$$

For  $A_1 = 0.3$ ,  $A_2 = 0.5$ ,  $A_3 = 0.2$ ,  $D = 0.4$ ,  $r = 0.11559633$ ,  $g = 9.8$ ,  $R = 6378000$ ,  $F = 3.4$ ,  $\omega = 1.8$ , the new parameters are solved as  $a = 1.333$ ,  $b = 3.776$ ,  $l = 4.6 \times 10^{-6}$ ,  $h = 11.333$ . For initial condition  $[-3.4, 2.1, 0]$ , the HPS shows chaotic behavior. The phase portrait is shown in Figure 2.

**2.1. Dynamic Analysis of HPS.** In this section we analyze the dynamic properties of HPS (9) like equilibria points, Lyapunov exponents, and bifurcation diagrams. The system does not have a fixed equilibrium point as the system model is nonautonomous.

Lyapunov exponents of a nonlinear system define the convergence and divergence of the states. Lyapunov exponents (LEs) are necessary and more convenient for detecting chaos in dynamical systems, and the existence of a positive Lyapunov exponent confirms the chaotic behavior of the system [8–12]. Time series based LEs calculation methods like Wolf algorithm [9], Jacobian method [10], and neural network algorithm [11] are popularly known ways of calculating Lyapunov exponents for integer and fractional order systems. To calculate the LEs of the HPS we use the Wolf method [9] and the total simulation time taken to calculate LEs is 20000s. The LEs of the HPS are calculated as  $L_1 = 0.2198$ ,  $L_2 = 0$ ,  $L_3 = -1.5531$ , and one positive LE ( $L_1$ ) confirms that HPS exhibits chaotic oscillations.

To analyze the impact of the parameters on the HPS, we derive and investigate the bifurcation plots. By fixing all the other parameters, we vary parameter  $h$  between  $[9.8, 12.2]$ , and Figures 3(a) and 3(b) show the bifurcation plots for states  $x_1$  and  $x_2$ , respectively. The initial condition for the first iteration is fixed as  $[-3.4, 2.1, 0]$  and is changed in every iteration as the end value of the state trajectory. The bifurcation plots show regions of period-5 limit cycle ( $9.9 \leq h \leq 10.05$ ), period-4 limit cycle for ( $11.83 \leq h \leq 11.9$ ), period-2 limit cycle for ( $11.91 \leq h \leq 12.1$ ), and period-1 limit cycle for ( $12.1 \leq h \leq 12.2$ ). As can be seen from Figure 3, the HPS takes period halving exit from chaos and period doubling limit cycle route to chaos. Furthermore an in-depth observation of Figure 3(a) gives a clue of hysteresis and bistability existence by showing discontinuous bifurcation.

**2.2. Multistability in HPS.** Multistability in mechanical systems is important in analyzing the system performance and its nonlinear behavior. A model of a vibroimpact oscillator, known as impact pair, composed of a point mass free to move inside a periodically driven box is investigated for its multistable property [13]. The statistical mechanics of shape transitions in small elastic elliptical plates and shells driven by noise and their multistable feature is analyzed in [14]. Multistability and controllability of multistability in the presence of noise and transition to chaos in noise and quasi-periodically driven systems are of significance [15–17]. Multistable features of HPS are investigated in this section and the bifurcation diagram is obtained by plotting local maxima of the coordinate  $x_2$  in terms of the parameter that is increased (or decreased) in tiny steps in the range of  $9.8 \leq h \leq 12.2$ . This strategy, known as forward and backward continuation, represents a simple way to localize the window in which the system develops multistability. The existence of multistability can be confirmed by comparing the forward (Figure 4(a) red) and backward (Figure 4(a) black) bifurcation diagrams. Figure 4(b) shows the coexisting attractors for various values of  $h$  and initial conditions  $[3.4, -2.1, 0]$  (red plot),  $[3.4, -2.1, -1.8]$  (blue plot).

### 3. Time Delayed HPS (TDHPS)

Time delayed differential equations play an important role in most of the engineering applications [18]. Time delay effects on mechanical systems have gained interest in recent years.

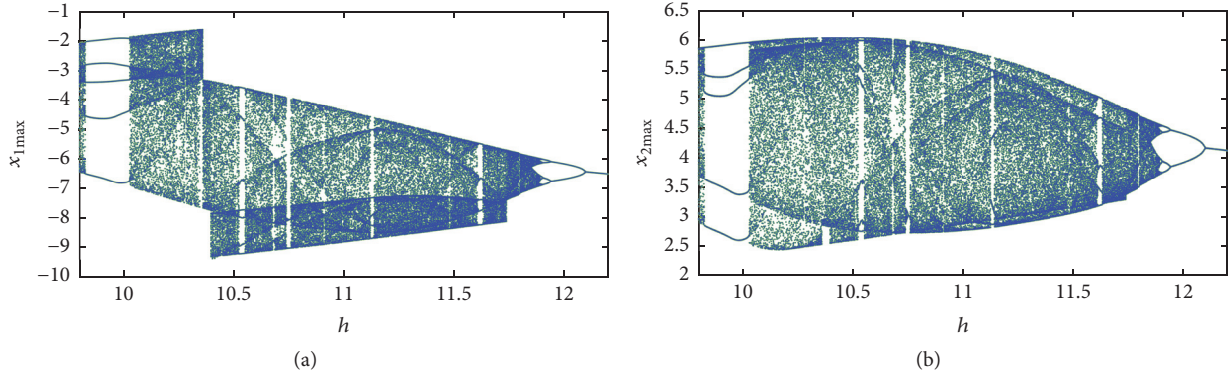


FIGURE 3: Bifurcation of the HPS (9) with the parameter  $h$ ((a)  $x_1$  and (b)  $x_2$ ).

The increased efficiency requirements in the control inputs and controller feedback have demanded the analysis of the effect of time delays on the system. The time delays in both controllers and actuators have become a serious problem and, for instance, all digital controllers, analogue antialiasing, and reconstruction filters exhibit a certain time delay during operation, and the hydraulic actuators and human machine interaction usually show even more significant time delays [19]. Considering these facts, we are interested in analyzing the time delay effects on the HPS dynamics.

**3.1. Time Delayed Nonautonomous HPS.** We first introduce feedback state delay for the state variable  $x_1$  and modify the nonautonomous HPS (8) as

$$\begin{aligned} \dot{x}_1(t) &= x_2(t) \\ \dot{x}_2(t) &= -a_\tau x_2(t) - b_\tau \sin x_1(t - \tau) \\ &\quad + l_\tau \cos x_1(t - \tau) \sin x_1(t - \tau) \\ &\quad + h_\tau \cos \omega_\tau t. \end{aligned} \quad (10)$$

and for the constant time delay  $\tau = 0.1$ , parameter values  $a_\tau = 1.333$ ,  $b_\tau = 3.776$ ,  $l_\tau = 4.6 \times 10^{-6}$ ,  $h_\tau = 11.333$ ,  $\omega_\tau = 2$ , and initial conditions  $[-3.4, 2.1, 0]$ , the time delayed nonautonomous HPS (TDNHPS) shows chaotic behavior as shown in Figure 5.

As discussed in the HPS, the TDNHPS also does not have a fixed point as the system is nonautonomous. To calculate the Lyapunov exponents of the TDNHPS, there are several algorithms proposed in the literature [20–22]. In this paper we adopted the technique employing the synchronization of identical systems coupled by linear negative feedback mechanism [21] for finding the exact Lyapunov exponents that are calculated as  $L_1 = 0.2311$ ,  $L_2 = -1.5245$ .

To analyze the impact of the time delays on the proposed TDNHPS, we derive the bifurcation of the system with the time delay  $\tau$  varied between  $[0.0001, 1]$  and the system parameters fixed at their respective values for chaotic behavior, and the initial condition for first iteration is  $[-3.4, 2.1, 0]$  and is changed to the end values of the state trajectory in every iteration. Figure 6 shows the bifurcation plot of TDNHPS with time delay, and as can be seen from the figure the system

shows multiple chaotic regions for  $0.0001 \leq \tau \leq 0.01$ ,  $0.15 \leq \tau \leq 0.35$ ,  $0.4 \leq \tau \leq 0.72$ , and  $0.77 \leq \tau \leq 0.9$ . The TDNHPS takes period doubling limit cycle route to chaos and inverse period doubling exit from chaos.

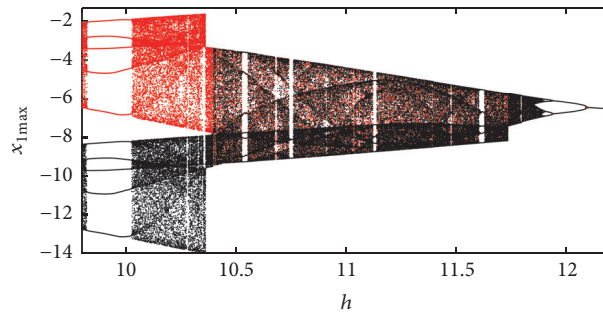
Figure 7 shows the bifurcation of the TDNHPS with the angular frequency of the excitation. As seen from the figure the TDNHPS shows discontinuous bifurcation with chaotic oscillations for  $1.77 \leq \omega_\tau \leq 2.05$ ,  $2.35 \leq \omega_\tau \leq 2.57$ , and  $2.6 \leq \omega_\tau \leq 2.7$  and takes period doubling route to chaos and period halving exit from chaos.

**3.2. Time Delayed Autonomous HPS (TDAHPS).** The time delayed autonomous system for the HPS (9) is derived by introducing the constant time delay in the feedback of state variable  $x_1$  given as

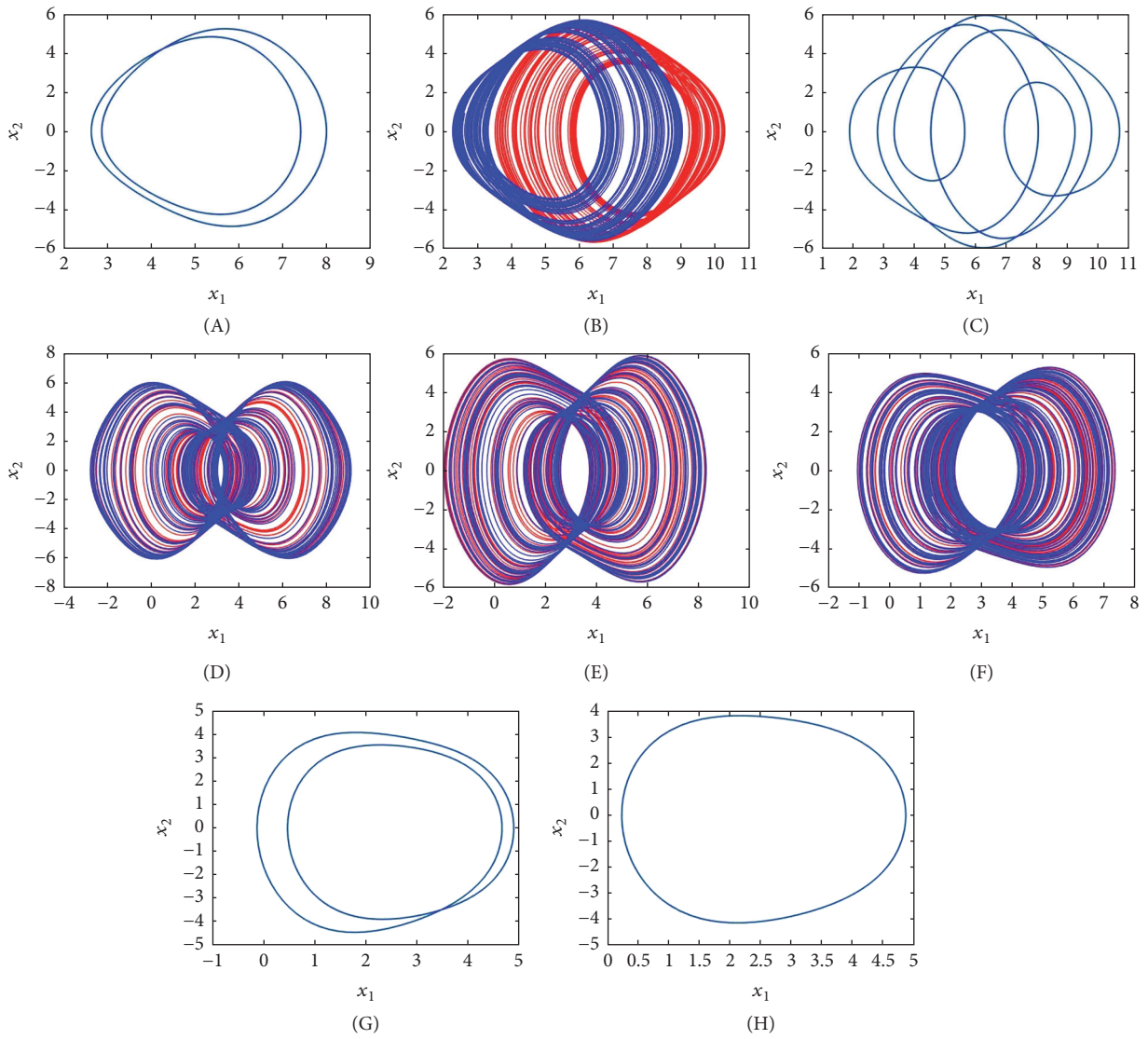
$$\begin{aligned} \dot{x}_1(t) &= x_2(t) \\ \dot{x}_2(t) &= -ax_2(t - \tau) - b \sin x_1(t - \tau) \\ &\quad + l \cos x_1(t - \tau) \sin x_1(t - \tau) \\ &\quad + h \cos x_3(t) \\ \dot{x}_3(t) &= \omega. \end{aligned} \quad (11)$$

Like TDNHPS, the TDAHPS also shows chaotic behavior for the same conditions and parameter values, and the chaotic attractor is shown in Figure 8.

There are no defined fixed points for the system and the Lyapunov exponents of the system are calculated as  $L_1 = 0.2392$ ,  $L_2 = 0$ ,  $L_3 = -1.5137$ . The bifurcation of the TDAHPS with time delay is given in Figure 9. Unlike TDNHPS (Figure 6), the TDAHPS shows nearly continuous bifurcation for  $0.05 \leq \tau \leq 0.8$  and takes routing entry to and exit from chaos with period doubling and period halving limit cycle, respectively. Also there is significant difference between the bifurcation patterns of TDNHPS and TDAHPS confirming that the approximation of the time with a third state is not an effective method to convert nonautonomous to autonomous systems when time delay effects are considered. Similarly the effect of the parameter ( $\omega_\tau$ ) also varies between autonomous and nonautonomous HPS as can be seen from Figures 10 and 7, respectively.



(a) Multistability in HPS with the red plots showing the forward continuation (increase parameter  $h$  from 9.8 to 12.2) and black plots showing backward continuation (decrease parameter  $h$  from 12.2 to 9.8) with reinitializing of the initial conditions



(b) Coexisting attractors for various values of  $h$  and initial conditions  $[3.4, -2.1, 0]$  (red plot),  $[3.4, -2.1, -1.8]$  (blue plot); (A)  $h = 9$ ; (B)  $h = 9.5$ ; (C)  $h = 10$ ; (D)  $h = 10.5$ ; (E)  $h = 11$ ; (F)  $h = 11.5$ ; (G)  $h = 12$ ; (H)  $h = 12.2$

FIGURE 4

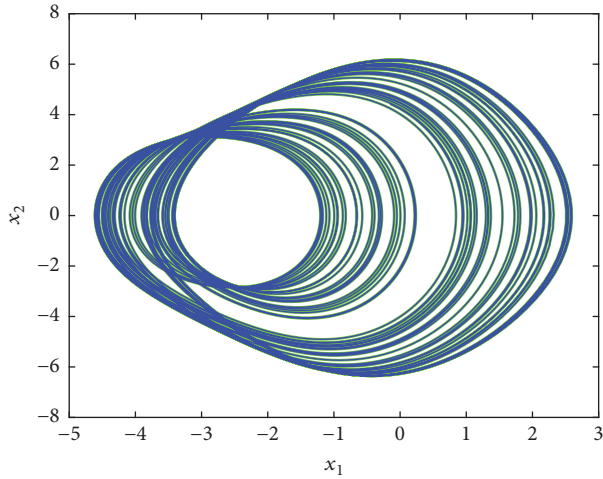


FIGURE 5: Chaotic attractor of the time delayed nonautonomous HPS.

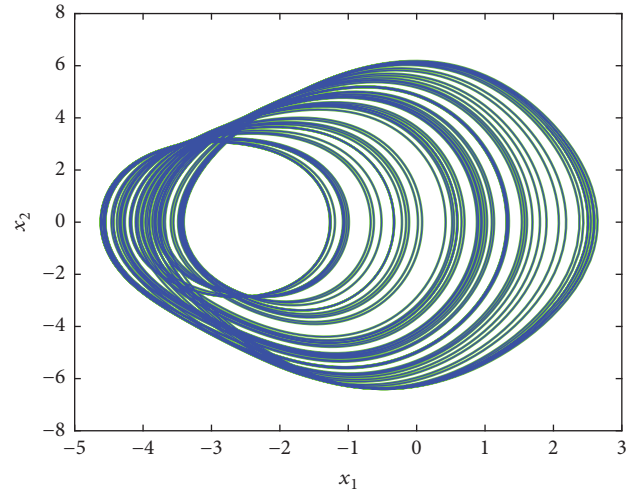


FIGURE 8: Phase portrait of the time delayed autonomous HPS.

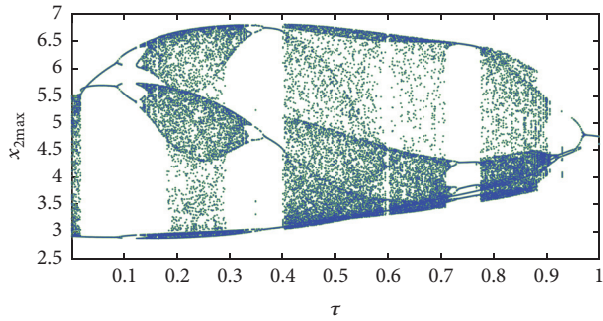


FIGURE 6: Bifurcation of the TDNHPS with time delay  $\tau$ .

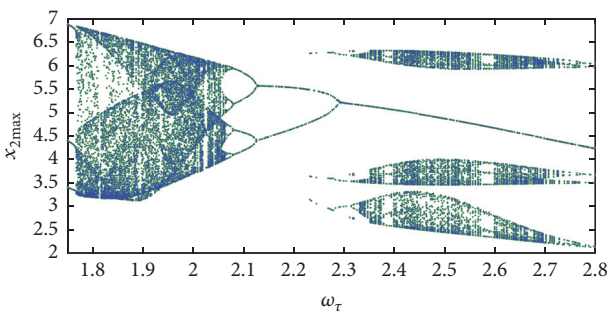


FIGURE 7: Bifurcation of the TDNHPS with parameter  $\omega_\tau$ .

**3.3. Multistability in Time Delayed Autonomous HPS.** To analyze the multistability existence in time delayed autonomous HPS, we derive and analyze the bifurcation of TDAHPS with parameter  $h_\tau$ . The initial condition for the first iteration is taken as  $[-3.4, 2.1, 0]$  and is reinitialized to the last value of the state variables at the end of every iteration, plotting local maxima of the coordinate  $x_2$  in terms of the parameter  $h_\tau$  that is increased from 9.8 to 13 (forward continuation) and decreased from 13 to 9.8 (backward continuation) in tiny steps. The constant time delay of the TDAHPS is fixed at 0.1. Figure 11 shows the multistability in TDAHPS, and as seen from the figure there are coexisting attractors for

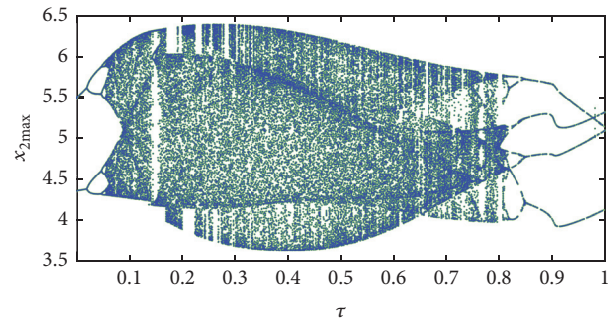


FIGURE 9: Bifurcation of the TDAHPS with time delay  $\tau$ .

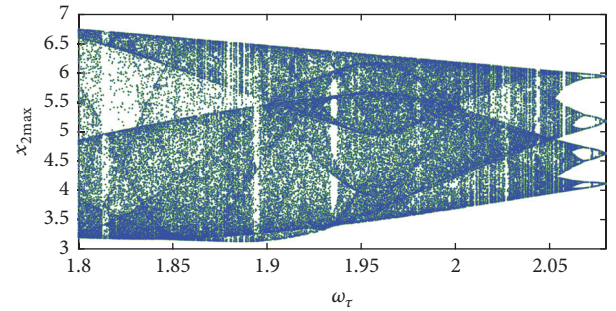


FIGURE 10: Bifurcation of the TDAHPS with parameter  $\omega_\tau$ .

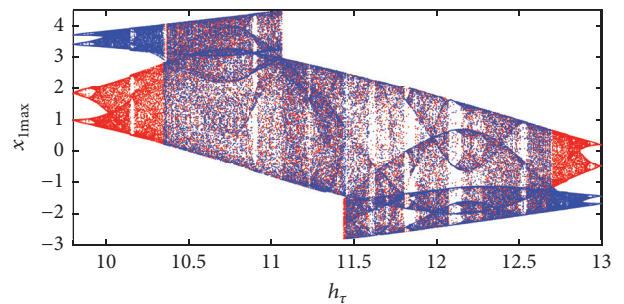


FIGURE 11: Multistability in TDAHPS with the red plots showing the forward continuation (increase in parameter  $h_\tau$  from 9.8 to 13) and blue plots showing backward continuation (decrease in parameter  $h_\tau$  from 13 to 9.8) with reinitializing of the initial conditions.

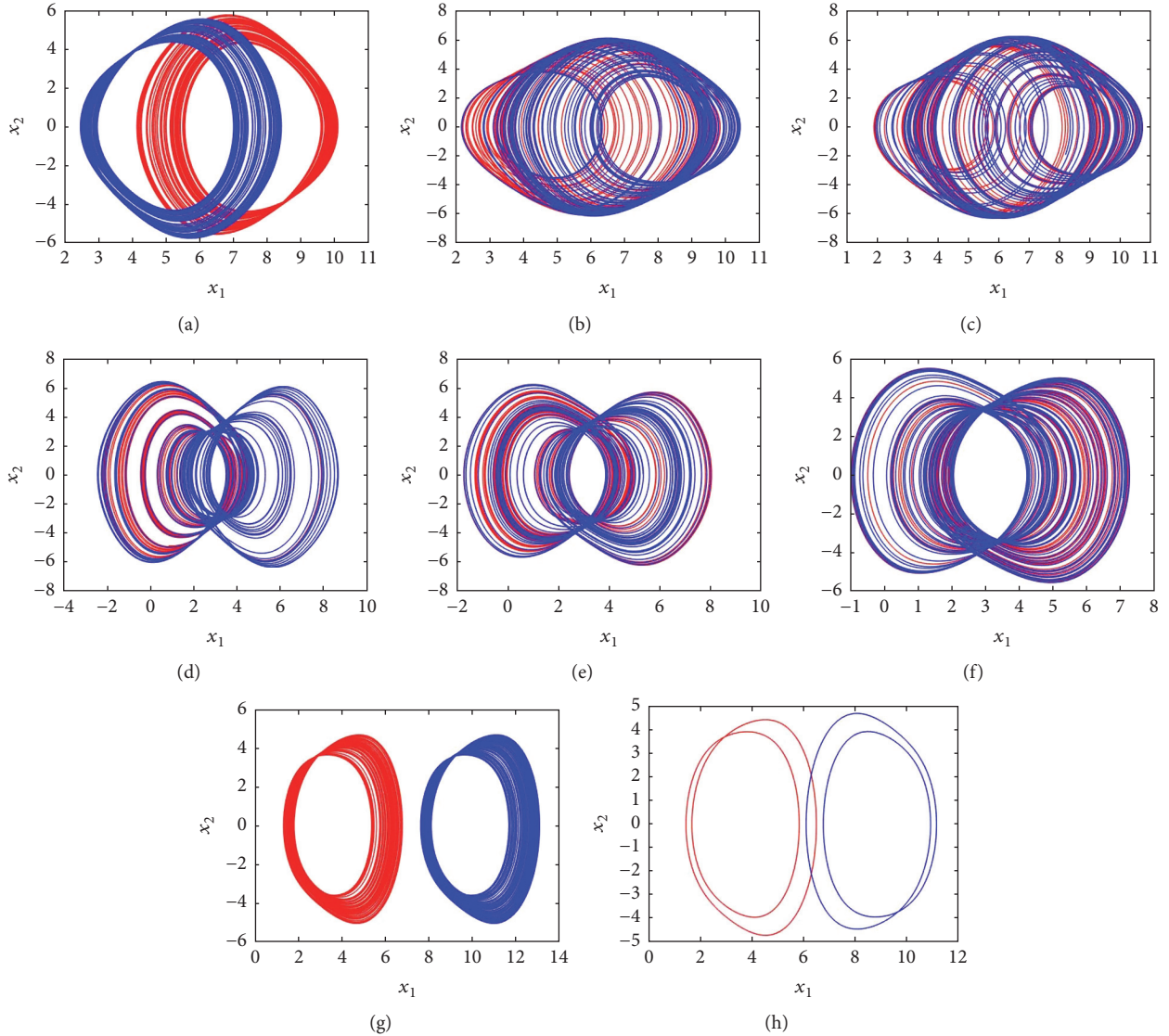


FIGURE 12: Coexisting attractors of the TDAHPS for various values of parameter  $h_\tau$ . (a)  $h_\tau = 10$ ; (b)  $h_\tau = 10.5$ ; (c)  $h_\tau = 11$ ; (d)  $h_\tau = 11.5$ ; (e)  $h_\tau = 12$ ; (f)  $h_\tau = 12.5$ ; (g)  $h_\tau = 12.8$ ; (h)  $h_\tau = 13$ .

$9.918 \leq h_\tau \leq 10.36$ ,  $11.45 \leq h_\tau \leq 11.46$ , and  $12.69 \leq h_\tau \leq 12.93$ . These coexisting attractors are evidence of multistability and are seen by comparing the forward (red) and backward (blue) continuation plots. Figure 12 shows the 2D phase portraits of the TDAHPS.

#### 4. Conclusion

Bifurcation analysis and chaotic behaviors exhibited by a horizontal platform system are studied for nonautonomous nondelayed system. The bifurcation of the HPS with parameter  $h$  shows that the system shows multistability with coexisting attractors. Time delay effects on the autonomous and nonautonomous HPS are derived by introducing a constant delay with the state feedback variable  $x_1$ . Bifurcation of the autonomous and nonautonomous TDHPS with time delay shows that the system behavior differs with the introduction

of the third state variable. Similarly the bifurcation of the parameters of the autonomous and nonautonomous TDHPS also shows difference. This clearly shows that a constant time delay can change the system behavior between the autonomous and nonautonomous systems. Multistability and coexisting attractors are seen in the TDHPS as well as the HPS.

#### Conflicts of Interest

The authors declare that there are no conflicts of interest regarding the publication of this paper.

#### References

- [1] S. Vaidyanathan and C. Volos, Eds., *Advances and applications in chaotic systems*, vol. 636 of *Studies in Computational Intelligence*, Springer, [Cham], 2016.

- [2] K. Rajagopal, A. Karthikeyan, and P. Duraisamy, "Bifurcation Analysis and Chaos Control of a Fractional Order Portal Frame with Nonideal Loading Using Adaptive Sliding Mode Control," *Shock and Vibration*, vol. 2017, Article ID 2321060, 2017.
- [3] P. Sekar and S. Narayanan, "Chaos in mechanical systems - A review," *SADHANA - Academy Proceedings in Engineering Sciences*, vol. 20, no. 2-4, pp. 529-582, 1995.
- [4] N.-S. Pai and H.-T. Yau, "Suppression of chaotic behavior in horizontal platform systems based on an adaptive sliding mode control scheme," *Communications in Nonlinear Science and Numerical Simulation*, vol. 16, no. 1, pp. 133-143, 2011.
- [5] C. C. Wang, N. S. Pai, H. T. Yau et al., "Bifurcation Analysis of Horizontal Platform System," *World Academy of Science, Engineering and Technology International Journal of Mathematical, Computational, Physical, Electrical and Computer Engineering*, vol. 4, no. 5, 2010.
- [6] M. P. Aghababa and H. P. Aghababa, "Synchronization of mechanical horizontal platform systems in finite time," *Applied Mathematical Modelling*, vol. 36, no. 10, pp. 4579-4591, 2012.
- [7] M. P. Aghababa, "Chaotic behavior in fractional-order horizontal platform systems and its suppression using a fractional finite-time control strategy," *Journal of Mechanical Science and Technology*, vol. 28, no. 5, pp. 1875-1880, 2014.
- [8] C. Li, Z. Gong, D. Qian, and Y. Chen, "On the bound of the Lyapunov exponents for the fractional differential systems," *Chaos: An Interdisciplinary Journal of Nonlinear Science*, vol. 20, no. 1, Article ID 016001CHA, 2010.
- [9] A. Wolf, J. B. Swift, H. L. Swinney, and J. A. Vastano, "Determining Lyapunov exponents from a time series," *Physica D: Nonlinear Phenomena*, vol. 16, no. 3, pp. 285-317, 1985.
- [10] S. Ellner, A. R. Gallant, D. McCaffrey, and D. Nychka, "Convergence rates and data requirements for Jacobian-based estimates of Lyapunov exponents from data," *Physics Letters A*, vol. 153, no. 6-7, pp. 357-363, 1991.
- [11] A. Maus and J. C. Sprott, "Evaluating Lyapunov exponent spectra with neural networks," *Chaos, Solitons & Fractals*, vol. 51, pp. 13-21, 2013.
- [12] M. S. Tavazoei and M. Haeri, "Unreliability of frequency-domain approximation in recognising chaos in fractional-order systems," *IET Signal Processing*, vol. 1, no. 4, pp. 171-181, 2007.
- [13] E. S. Medeiros, S. L. T. de Souza, and I. L. Caldas, "Multistability in Systems with Impacts, International conference on Chaos and Nonlinear Dynamics," in *Proceedings of the Multistability in Systems with Impacts, International conference on Chaos and Nonlinear Dynamics*, 2010.
- [14] L. Mahadevan and L. Ee Hou Yong, "Statistical Mechanics of Multistability in Microscopic Shells".
- [15] U. Feudel and C. Grebogi, "Multistability and the control of complexity," *Chaos: An Interdisciplinary Journal of Nonlinear Science*, vol. 7, no. 4, pp. 597-604, 1997.
- [16] S. Kraut, U. Feudel, and C. Grebogi, "Preference of attractors in noisy multistable systems," *Physical Review E*, vol. 59, pp. 5253-5260, 1999.
- [17] S. Kraut and U. Feudel, "Multistability, noise, and attractor hopping: The crucial role of chaotic saddles," *Physical Review E: Statistical, Nonlinear, and Soft Matter Physics*, vol. 66, no. 1, Article ID 015207, pp. 015207/1-015207/4, 2002.
- [18] J.-P. Richard, "Time-delay systems: An overview of some recent advances and open problems," *Automatica*, vol. 39, no. 10, pp. 1667-1694, 2003.
- [19] H. Y. Hu and Z. H. Wang, *Dynamics of controlled mechanical systems with delayed feedback*, Springer Berlin Heidelberg, 2002.
- [20] A. Stefanski and A. Dabrowski, "Tomasz Kapitaniak, Evaluation of the largest Lyapunov exponent in dynamical systems with time delay, Chaos," *Solitons Fractals*, vol. 23, no. 5, pp. 1651-1659, March 2005.
- [21] A. Stefanski, T. Kapitaniak, A. Dabrowski, A. Stefański, and A. Dąbrowski, "The Largest Lyapunov Exponent of Dynamical Systems with Time Delay," in *Proceedings of the IUTAM Symposium on Chaotic Dynamics and Control of Systems and Processes in Mechanics*, G. Rega and F. Vestroni, Eds., vol. 122, p. 122, Springer, Dordrecht, the Netherlands, 2005.
- [22] A. Dabrowski, "Estimation of the largest Lyapunov exponent-like (LLEL) stability measure parameter from the perturbation vector and its derivative dot product (part 2) experiment simulation," *Nonlinear Dynamics*, vol. 78, no. 3, pp. 1601-1608, 2014.